



저작자표시-비영리-변경금지 2.0 대한민국

이용자는 아래의 조건을 따르는 경우에 한하여 자유롭게

- 이 저작물을 복제, 배포, 전송, 전시, 공연 및 방송할 수 있습니다.

다음과 같은 조건을 따라야 합니다:



저작자표시. 귀하는 원저작자를 표시하여야 합니다.



비영리. 귀하는 이 저작물을 영리 목적으로 이용할 수 없습니다.



변경금지. 귀하는 이 저작물을 개작, 변형 또는 가공할 수 없습니다.

- 귀하는, 이 저작물의 재이용이나 배포의 경우, 이 저작물에 적용된 이용허락조건을 명확하게 나타내어야 합니다.
- 저작권자로부터 별도의 허가를 받으면 이러한 조건들은 적용되지 않습니다.

저작권법에 따른 이용자의 권리는 위의 내용에 의하여 영향을 받지 않습니다.

이것은 [이용허락규약\(Legal Code\)](#)을 이해하기 쉽게 요약한 것입니다.

[Disclaimer](#)

Ph.D. DISSERTATION

A STUDY ON SCAN BLINDNESS AND
FINITE SUBSTRATE EFFECT IN
PRINTED DIPOLE ARRAY

프린티드 다이폴 배열 내 스캔블라인드니스와
유한한 크기를 갖는 기판 효과에 대한 연구

FEBRUARY 2021

GRADUATE SCHOOL OF ELECTRICAL
ENGINEERING AND COMPUTER SCIENCE
SEOUL NATIONAL UNIVERSITY

HANNI KOO

공학박사 학위논문

A STUDY ON SCAN BLINDNESS AND
FINITE SUBSTRATE EFFECT IN
PRINTED DIPOLE ARRAY

프린티드 다이폴 배열 내 스캔블라인드니스와
유한한 크기를 갖는 기판 효과에 대한 연구

2021 년 2 월

서울대학교 대학원

전기 • 컴퓨터공학부

구 한 이

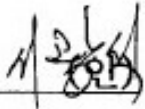
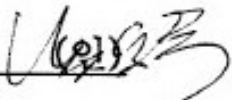
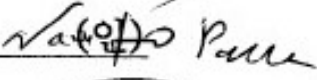
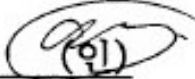
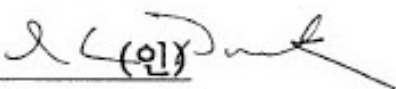
A STUDY ON SCAN BLINDNESS AND
FINITE SUBSTRATE EFFECT IN
PRINTED DIPOLE ARRAY

지도 교수 남 상 옥

이 논문을 공학박사 학위논문으로 제출함
2021 년 2 월

서울대학교 대학원
전기·컴퓨터공학부
구 한 이

구한이의 공학박사 학위논문을 인준함
2021 년 2 월

위원장	서광석	
부위원장	남상옥	
위원	박남규	
위원	오정석	
위원	박익모	

Abstract

In this thesis, a study on the mechanism of a printed dipole array mainly used in the millimeter wave band is conducted, which has an important role on the performance of it.

Two types of printed dipoles are mainly dealt with, and the first of them describes the scan blindness effect and causes that may occur in T-printed dipoles. Second, the operation principle of bow-tie element printed on a substrate with high dielectric is explained through Physical Optics and diffraction theory.

First, the scan blindness in a T-printed dipole in 1D and 2D array is analyzed, and an elimination strategy is proposed. The scan characteristics are obtained using an active element pattern (AEP) with an infinite rectangular lattice arrangement. Based on the propagation of a guided wave along the antenna row and the electric-field distribution observed during simulations, an equivalent circuit model for a unit cell of the T-printed dipole is obtained. A quasi-transverse electromagnetic (TEM) guided wave is predicted using the dispersion relation curve obtained from the equivalent circuit, and it is proved that the calculated curve is in good agreement with the eigen mode simulations and measured trajectory of the scan blind angle, for different frequencies. In addition, the Q value and scan blindness of the 1D array and the 2D array is considered, and it is verified that the mutual coupling of a 1D array decreases more than

that of a 2D array due to the radiation loss. Next, slits and stubs are introduced as parasitic structures, to eliminate the scan blindness and improve the antenna scan range. To confirm the effects of these parasitic elements, a linear array simulation is performed, which confirms the suppression of a quasi-TEM guided wave. Finally, the printed dipole array was fabricated, and an AEP was measured for the 11×1 (1D array) and 11×3 sub arrays (2D array). Their measurements validate the scan blindness prediction and confirm the proposed mechanism of scan blindness and its improvements.

In the second type, the principle of a printed bow-tie antenna on a high dielectric substrate is presented. For the sake of simplicity, it is assumed that the infinitesimal horizontal-electric dipole (HED) with unit current is located on the dielectric slab. And the theory of Physical Optics (PO) is applied. Through this study, it is theoretically concluded that the components of the antenna far-field are composed of geometric optics in which the direct ray radiated directly from the HED and the reflected wave by the dielectric are combined, and the diffracted ray generated by the space wave, surface wave, and leaky wave. In order to verify the validity of the theory, the electromagnetic wave analysis programs CST MWS and FEKO are used to compare and verify the theoretically obtained closed form. According to the results of the study, in the case of a high dielectric substrate with dielectric constant of 10 or more, the main component that constitutes the radiation pattern is TE₀ surface-wave (SW) diffracted ray generated from the edge of the dielectric slab. In

addition, the directivity of the antenna can obtain a high gain of 10 dBi or more, which is advantageous for single antenna design.

Finally, based on the previously derived theory, a ku-band printed Bow-tie array antenna with low mutual coupling is proposed. The diffracted ray induced at the edge of the truncated dielectric slab not only generates high gain, but also can reduce mutual coupling due to the cancellation effect of direct ray and reflected ray. In addition, an ohmic sheet is added on the dielectric slab of the single element to attenuate the surface waves traveling to the side and it leads to minimize the mutual coupling. In particular, there is an advantage of obtaining high gain and low mutual coupling without adding additional structures. The single element is designed and fabricated as a 1D sub-array in the H-plane direction. It is confirmed that the gain is higher than 6.5 dBi, and the mutual coupling is less than -20 dB in the band after 12.8 GHz.

In conclusion, this thesis propose that the electromagnetic mechanism of the two printed type antenna. For the T-printed dipole, it is revealed that the cause of the scan blindness is TEM guided mode. And It is theoretically revealed that the main cause of the printed bow tie antenna with high permittivity is the diffracted ray of TE_0 SW generated from the antenna.

Keywords: T-printed dipole, Scan blindness, Bow-tie antenna on high dielectric slab, Physical Optics, Diffracted Ray, Mutual coupling

Student Number: 2015-31012

Table of Contents

Abstract.....	i
Table of Contents.....	v
List of Figures	ix
List of Tables.....	v
Chapter 1. Introduction.....	1
1.1. Trend of T-Printed Dipoles	1
1.2. Scan blindness and its elimination methods.....	3
1.3. High Dielectric Antennas and Physical Optics (PO) .	7
1.4. References.....	9
Chapter 2. Analysis of Scan Blindness in a T-Printed Dipole Array	12
2.1. Motivation	12
2.2. Study on Single Element Design	13
2.3. Active Element Pattern in Infinite Array	16
2.4. E-field Distribution in Infinite Array	18
2.5. Dispersion Diagram.....	20

2.6. Guided quasi-TEM mode.....	22
2.7. Equivalent Circuit.....	24
2.8. Parasitic Elements for Eliminating Scan Blindness .	25
2.8.1. Comparison of Active Reflection Coefficients...	27
2.8.2. Guiding Wave Suppression.....	27
2.8.3. Comparison of Dispersion Relations.....	30
2.9. 1D Array Analysis	31
2.10. Finite Array and Measurements	37
2.10.1. Physical Explanation for Finite Array.....	37
2.10.2. Scanning Performance.....	38
2.10.3. Simulations and Measurements	41
2.11. Conclusion	46
2.12. References.....	48
 Chapter 3. Analysis of an HED on a Truncated Dielectric Slab	
.....	50
3.1. Motivation	50
3.2. Basic Formulation for PO.....	52
3.3. Polarization Current in Multilayered Structures.....	52

3.3.1. TE _z Mode Solution in Spectral Domain.....	56
3.3.2. TM _z Mode Solution in Spectral Domain	60
3.3.3. Complete Polarization Current Solution	65
3.4. Dispersion Equation Solutions	67
3.4.1. Surface Wave Solutions.....	67
3.4.2. Complex Guided Wave Solutions	71
3.5. The Saddle–Point Method of Integration.....	74
3.6. Geometrical Optics.....	81
3.7. Diffracted Rays.....	84
3.7.1. Surface wave diffracted wave.....	84
3.7.2. Leaky wave diffracted wave	85
3.7.1. Space wave diffracted wave.....	86
3.8. Numerical Results	87
3.8.1. Analysis of both sides truncated substrate	85
3.8.2. Analysis of a substrate standing perpendicular to the ground plane	94
3.8.3. Limitation of the Physical Optics	94
3.9. Implementation of Bow–tie printed Dipole Array .	100
3.9.1. Motivation	100
3.9.2. Single Antenna Design.....	101

3.9.3. Return Loss Characteristics.....	101
3.9.4. Mutual Coupling.....	101
3.9.5. Measurements.....	111
3.9.5.1 Single Element.....	111
3.9.5.2 H-plane 1-D Array.....	113
3.10. Conclusions.....	116
3.11. References.....	118
 Chapter 4. Conclusions.....	 119
 Appendix.....	 121
A.1. Derivation of Dispersion Relations.....	121
A.2. Detailed Derivation of (3.43).....	128

List of Figures

Fig. 1.1. Evolution of a Printed Dipole Antenna. (a) Conventional dipole with a coaxial balun. (b) Printed dipole with integrated balun. (c) Recent printed dipole.....	2
Fig. 1.2 Scan Blindness and its elimination methods	5
Fig. 1.3 Printed Dipole Type Antenna with High Dielectric.(a) WideBand Modified Printed Bow Tie Antenna. (b) Surface Wave Enhanced Yagi–Uda Antenna. (c) Horizontal Electric Dipole on odd High Dielectric Substrate..	7
Fig. 1.4 Measured ambient RF power at outdoors [23–25]. (a) London. (b) Colorado, USA. (c) Seoul, South Korea.....	8
Fig. 2.1 Geometry of an element: (a) Basic T–printed dipole. (b) Tprinted dipole with slits and stubs.....	12
Fig. 2.2 Active element pattern in an infinite array. (Comparison of E–plane and H–plane): (a) Basic T–printed dipole. (b) Tprinted dipole with slits and stubs	14
Fig. 2.3 E–field distribution between two dipoles in infinite array when Floquet excitation is performed so that the incident angle is (a) blind angle (36°) and (b) boresight angle (0°)	16
Fig. 2.4. Simulated dispersion diagrams of eigen mode, trajectory of scan blindness, and calculated dispersion relations obtained from Appendix (A.12).	19

Fig. 2.5. Electric field distribution of coupling between linear infinite dipole arrays placed 10 unit cells apart at 35 GHz for basic Tprinted dipole array	20
Fig. 2.6. (a) Equivalent topology of a T–printed dipole unit cell. (b) Transformed equivalent circuit	20
Fig. 2.7. Comparison of four types of two–dimensional active reflection coefficients: (a) basic T–printed dipole, (b) with stubs, (c) with slits, and (d) with slits and stubs	23
Fig. 2.8. Electric field distribution of coupling between linear infinite dipole arrays placed 10 unit cells apart at 35 GHz for basic Tprinted dipole array)	23
Fig. 2.9. Electric field distribution of coupling between linear infinite dipole arrays placed 10 unit cells apart at 35 GHz for basic Tprinted dipole array.....	25
Fig. 2.10. Simulation and measurement results of (a) Input reflection coefficient. (b) Maximum realized gain and total radiation efficiency.....	26
Fig. 2.11. Simulated dispersion diagram of eigen mode for different length of the slit ($slit_h$) and stub ($stub_h$)	26
Fig. 2.12. 1D Active element pattern	28
Fig. 2.13. Dispersion relations comparison between eigen mode simulation and scan blindness.	31
Fig. 2.14. Q factor comparison between 1 D and 2 D.	31

Fig. 2.15. Electric field simulation of coupling between linear dipole arrays placed 9 unit cells apart for open boundary. (a) Open boundary (b) PMC boundary	32
Fig. 2.16. S-parameter between linear dipole arrays placed 9 unit cells apart	32
Fig. 2.17. Geometry of 11×3 basic T-printed dipole array for a finite active element pattern	33
Fig. 2.18. Structure of an active element pattern of the 11×3 array (a) Basic printed dipole. (b) Proposed	33
Fig. 2.19. Structure of fully excited 8×1 arrays in E-plane with 41° scan angle. (a) Basic printed dipole. (b) Proposed.	33
Fig. 2.20. Simulated scanning performance in the E-plane for the 11×3 arrays with an excited 8-element linear array. (a) Basic printed dipole (b) Proposed.....	36
Fig. 2.21. Four types of center row substrate arrays fabricated: (a) Active element pattern (AEP) of the 11×3 arrays for the basic T-printed dipole. (b) AEP of the 11×3 arrays for the proposed T-printed dipole. (c) Fully excited 8×1 arrays for the basic T-printed dipole. (d) Fully excited 8×1 arrays for the proposed T-printed dipole. (e) Array of printed dipoles with slits and stubs mounted on the antenna bracket	61
Fig. 2.22. . E-plane co-polarization active element pattern of the 11×3 arrays. (a) Basic printed dipole. (b) Proposed	56
Fig. 2.23. Fully excited 8×1 arrays in E-plane co-polarization at 41° scan angle. (a) Basic printed dipole. (b) Proposed.....	59

Fig. 2.24. Printed Dipole AEP in the E–plane for 1D array. (a) 11×1 sub array for printed dipole. (b) 11×1 sub array for printed dipole with slit and stub	43
Fig. 2.25. Comparison of scan blindness occurrences when the printed dipole array antenna is steering from broadside to 50° in the Eplane. Eigen mode (simulated) vs. dispersion relations (calculated) vs. scan blindness (measured)	44
Fig. 3.1 Geometry of an HED over a truncated dielectric slab on the ground plane	52
Fig. 3.2. Equivalence theorem. (a)current on dielectric slab. (b)Equivalent current source.....	55
Fig. 3.3 Spectral equivalent circuit for the TE _z mode.....	57
Fig. 3.4. Spectral equivalent circuit for the TM _z mode	62
Fig. 3.5. Surface–wave pole solutions. (a)TE mode. (b)TM mode.	70
Fig. 3.6. Graphical solution for complex pole solutions. Solid lines are for real part solution; broken lines are imaginary part solution. (a)TE mode. (b)TM mode.....	74
Fig. 3.7. Topology of the proper Rieman sheet of the complex ky plane.....	76
Fig. 3.8. Topology of the top Rieman sheet of the complex s plane.	77
Fig. 3.9. Radiation Pattern for infinite dielectric slab. (a) 3D simulation results (b) comparison.....	83
Fig. 3.10. Truncated dielectric slab modeling	88

Fig. 3.11. Radiation pattern at H-plane for truncated dielectric slab (ϕ component, $\epsilon_r = 4$).....	88
Fig. 3.12. Radiation pattern at Diagonal plane for truncated dielectric slab. (a) ϕ component (b) θ component.....	90
Fig. 3.13. Surface-wave diffraction contribution.	91
Fig. 3.14. Space-wave diffraction contribution.	91
Fig. 3.15. Geometric Optics contribution.....	92
Fig. 3.16. Fig. 3.16. Diffracted ray and GO contributions for $\epsilon_r = 12.2$	93
Fig. 3.17 (a) Truncated dielectric slab over the ground plane. (b) Image theory model 1 (c) Image theory model 2..	95
Fig. 3.18. Far-field pattern for $\epsilon_r = 12.2$, $Ly = 0.2 \lambda_0$	96
Fig. 3.19. Fabricated 15x1 H-plane Array.....	99
Fig. 3.19 Design model (a) Front view (b) Side view	97
Fig. 3.20. Directivity for $\epsilon_r = 12$, $Ly = 0.2 \lambda_0$. : (a) Radiation pattern and E-field distribution, and (b) comparison PO calculations with CST simulations.	99
Fig. 3.21. (a) An HED on the finite dielectric substrate over the ground, and its (b) directivity pattern depend on cutting angle..	102
Fig. 3.22. (3D directivity pattern for Fig.3.21: (a) $\theta_{cut}=0^\circ$, and (b) $\theta_{cut}=60^\circ$	102

Fig. 3.23. An HED on the substrate with trapezoidal type over the ground: (a) Perspective view, (b) Front view, (c) Side view, and (d) Top view.	105
Fig. 3.24. E and H-plane single element pattern.....	106
Fig. 3.25. Single element model: (a) model 1, (b) model 2, and (c) model 3..	107
Fig. 3.26. Return loss characteristics for Fig. 3.25.	108
Fig. 3.27. Two element array: (a) geometrical model, and (b) mutual coupling on dielectric constant changes.	110
Fig. 3.28. Fabricated single element.....	111
Fig. 3.29. Far-field pattern in H-plane: (a) Measurements VS CST Simulations, and (b) Measurements VS PO Calculations.....	112
Fig. 3.30. Fabricated 15x1 H-plane Array.....	113
Fig. 3.31. S-parameter results. (a) Return loss (b) Mutual coupling between the center element and the adjacent element.....	114
Fig. 3.32. E and H-plane co-polarization active element pattern of 15x1... ..	115
Fig. A.1.1 Extraction of TL parameters. (a) Simulation setup for TL parameters. (b) Characteristic Impedance Z_{TL} and phase constant β_{TL}	125
Fig. A.1.2. Extraction of gap capacitance parameters. (a) Simulation setup for gap capacitance parameters. (b) Gap capacitance for series (C_{gs}) and gap capacitance for parallel (C_{gp}).....	126

Fig. A.1.3. Extraction of transformer parameters. (a) Simulation setup for transformer parameters. (b) Self-inductance (L) and mutual inductance (L_m).....27

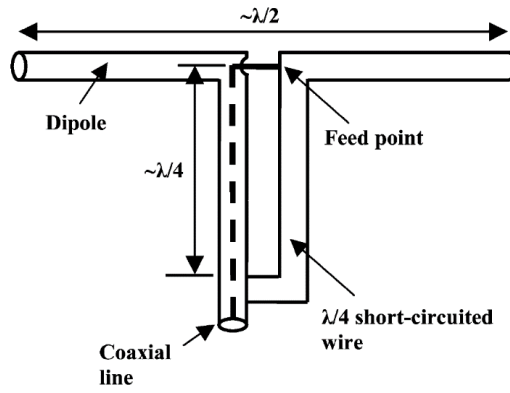
List of Tables

TABLE 2.1. Design parameters of T-printed dipole element	13
TABLE 3.1. Special equivalent circuit for electric current	56
TABLE 3.2. Dispersion equation	65
TABLE 3.3. Dispersion equation for complex wave	71
TABLE 3.4. Diffraction Coefficient.....	81

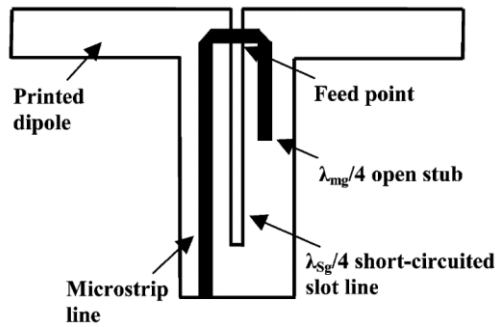
Chapter 1. Introduction

1.1. Trend of T-Printed Dipoles

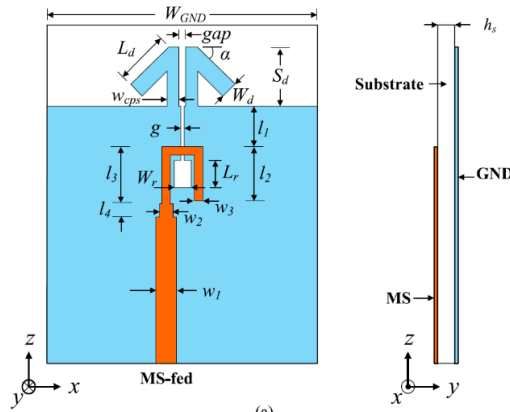
A T-printed dipole with integrated balun has been proposed for wireless communication at microwave frequencies, because it has many advantages such as light weight, low cost, ease of fabrication, and suitability for integration with microwave integrated circuit modules. Fig 1.1 (a) shows conventional dipole with a coaxial balun. The outer conductor of the coaxial line and the $\lambda_0/4$ short-circuited wire make infinite impedance at the feed point, and eliminating current flow on the outer surface of the outer conductor of the coaxial line [1]. For a printed dipole shown in Fig 1.1 (b), the coaxial balun can be replaced with a microstrip line, an open stub and a short-circuited slot line [2]. Fig 1.1 (c), presented a broadband printed-dipole antenna. To achieve the impedance matching over a broad frequency range, the balun acts as a microstrip to-slot-line transformer, which consists of a folded microstrip line connected to the feedline and a rectangular slot etched on the ground plane. Impedance matching is realized by adjusting the folded line and rectangular slot. In addition, a microstrip stub is inserted between the two printed angled-dipole antennas for mutual coupling reduction [3].



(a)



(b)



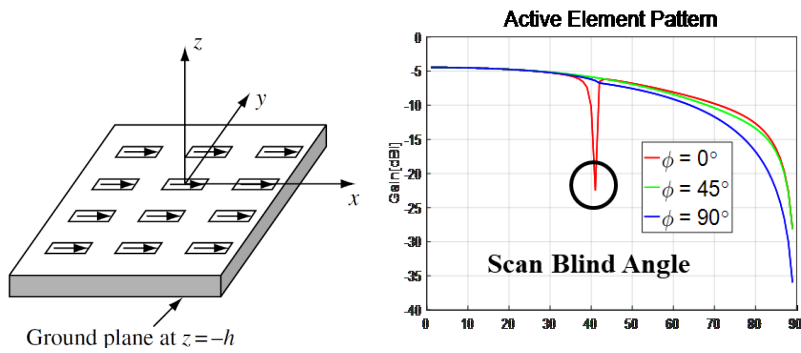
(c)

Fig. 1.1. Evolution of a Printed Dipole Antenna: (a) Conventional dipole with a coaxial balun, (b) Printed dipole with integrated balun, and (c) Recent printed dipole.

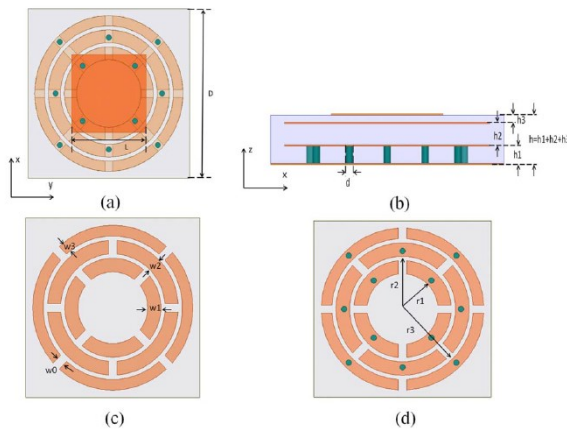
1.2. Scan blindness and its elimination methods

Scan blindness is a critical issue in phased array antennas. If an infinite phased array structure is capable of supporting a guided wave, then under certain Floquet excitations, the amplitude of the guided mode field increases infinitely, resulting in infinitely large input impedance. Thus, the array ceases to radiate. This phenomenon is known as scan blindness and the corresponding angle at which this occurs is called the blind angle [4]. Comprehensive studies have been conducted on the scan blindness in planar printed antennas such as dipoles or rectangular microstrip patches, based on the coupling from Floquet modes to surface-wave modes [5]–[8]. However, scan blindness is caused by not only surface waves but also various other factors. In 1991, infinite arrays of printed dipoles on finite-height dielectric sheet were analyzed using Green's function moment method approach and mode matching and its scan blindnesses were observed in the E-plane. In 1994, E-plane scan results were presented for infinite arrays of microstrip-fed dipoles printed on protruding dielectric substrates. In 1996, a model of parallel-plate modes was proposed to predict the existence and location of the E-plane scan blindness in a tapered-slot single-polarized array, which is associated with a guided wave on a corrugated surface [9]. In 2008, the scan blindness in single polarized tapered-slot elements in triangular grids was explained to have occurred because of the

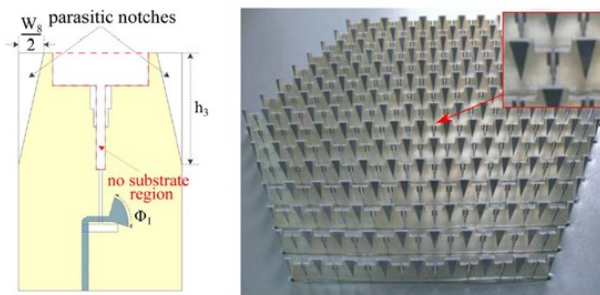
presence of leaky waves in the structure [10]. Various methods have been proposed to reduce the scan blindness in phased arrays, depending on the antenna element geometry [11]–[17]. The electromagnetic bandgap (EBG) structure is an effective method to eliminate scan blindness by suppressing the surface waves generated in printed phased arrays, and many related methods have been proposed [11]–[15]. Studies have been conducted to eliminate the scan blindness in Vivaldi arrays [16], [17]. In 2014, triangular parasitic notches were proposed to reduce the magnitude of leaky modes for E–plane scanning, and shift the cavity resonances of stripline–fed tapered–slot antennas to higher frequencies [16]. In 2018, a sliced notch antenna (SNA) array was proposed, which offered better suppression of the classical Vivaldi E–plane scan blindness [17].



(a)

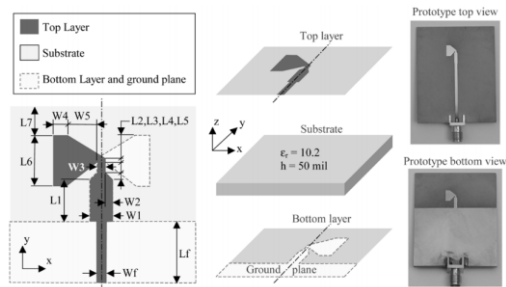


(b)

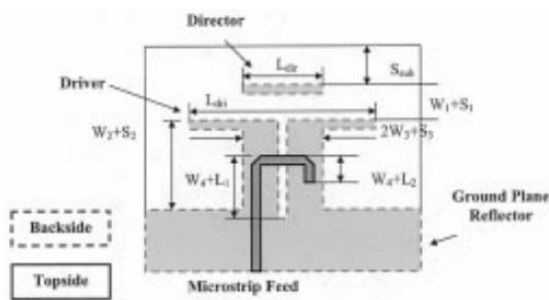


(c)

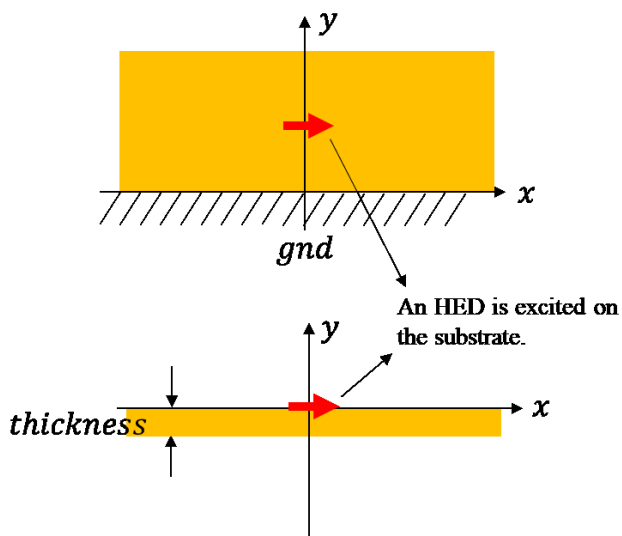
Fig. 1.2 Scan Blindness and its elimination methods:
 (a) Scan blindness and calculated results [1], (b) Bandgap- antenna [1], and (c) tapered-slot array including parasitic notches [1].



(a)



(b)



(c)

Fig. 1.3 Printed Dipole Type Antenna with High Dielectric: (a) Wide-Band Modified Printed Bow Tie Antenna [1], (b) Surface Wave Enhanced Yagi-Uda Antenna [1], and (c) Horizontal Electric Dipole on High Dielectric Substrate.

1.3. High Dielectric Antennas and Physical Optics (PO)

Printed dipole on high dielectric provides high gain and simple structure, so it is good candidate for wideband phased array systems. Fig 1.3(a) shows a wideband modified printed bow-tie antenna, covering the entire C and X bands and part of the Ku-band. The antenna is a good candidate for wideband phased array systems. Fig 1.3(b) shows the broadband printed antenna [18]. A TE₀ surface-wave is used as the primary source of free space radiation. In both Figs 1.3 (a) and (b), a high dielectric constant substrate with an ϵ_r of 10.2 is used to obtain broadband and high gain [19].

However, the specific mechanism for the mechanism of a printed antenna on high dielectric has not yet explained precisely. So, it is suggested to use the physical-optics (PO) approximation to analyze the mechanisms of the high dielectric printed antennas [20], [21]. Especially, PO provides physical insight into the diffraction phenomenon, and supplies an effective tool for predicting the effects of finite substrates in patch antenna as shown in Fig.1.4 [20]. In this thesis, the principle of operation is discussed by modeling an horizontal electric dipole (HED) on high dielectric substrate as shown

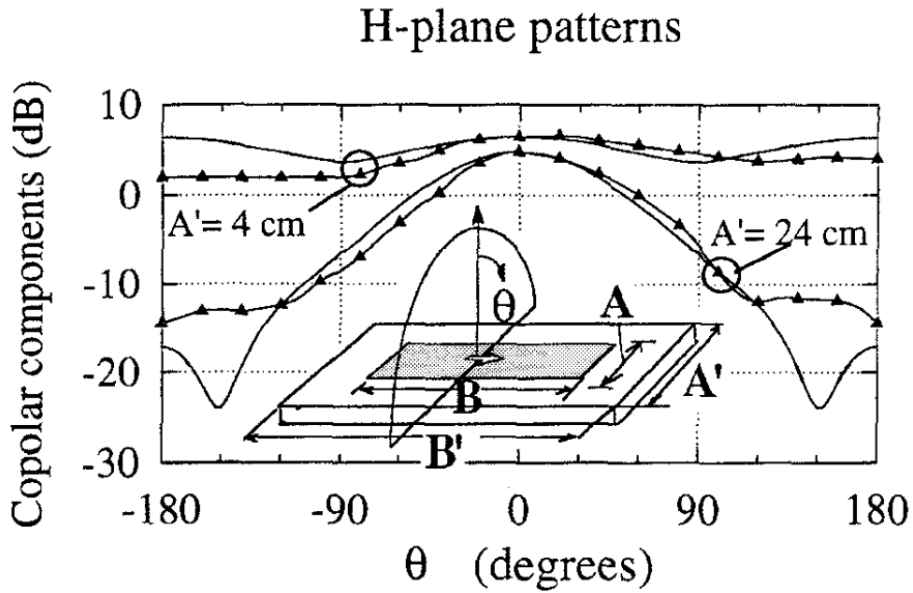


Fig. 1.4. Directivity pattern (copolar components, H-plane) for a rectangular patch over a finite rectangular-grounded slab ($f = 1.05$ GHz, $f = 3.25$ h = 1.524 mm); calculated (continuous line), measured Dielectric Substrate [20].

in Fig. 1.3(c) is very similar to the structure of dielectric with ground, it is reasonable to analyze the far-field component with PO. Furthermore, by using these various rays as multipath cancellation, mutual coupling of the array antennas can be reduced.

1.4. References

- [1] C. A. Balanis, *Antenna Theory: Analysis and Design*. New York: Wiley, 2005, pp. 53.
- [2] R. Li, T. Wu, B. Pan, K. Lim, J. Lascar, and M. Tentzeris, “Equivalent circuit analysis of a broadband printed dipole with adjusted integrated balun and an array for base station applications,” *IEEE Trans. Antennas Propag.*, vol. 57, no. 7, pp. 2180–2184, Jul. 2009.
- [3] S. X. Ta, H. Choo, and I. Park, “Broadband printed–dipole antenna and its arrays for 5G applications,” *IEEE Antennas Wireless Propag. Lett.*, vol.16, pp. 2183–2186, 2017.
- [4] A. K. Bhattacharyya, *Phased Array Antennas: Floquet Analysis, Synthesis, BFNs and Active Array Systems*. Hoboken, NJ, USA: Wiley, 2006.
- [5] D. M. Pozar and D. H. Schaubert, “Scan blindness in infinite phased arrays of printed dipoles,” *IEEE Trans. Antennas Propag.*, vol.32,no. 6, pp. 602–610, Jun. 1984.
- [6] D. M. Pozar and D. H. Schaubert, “Analysis of an infinite array of rectangular microstrip patches with idealized probe feeds,” *IEEE Trans. Antennas Propag.*, vol. 32, no.10, pp.1101–1107, Oct.1984.
- [7] D. M. Pozar, “Analysis of finite phased arrays of printed dipoles,” *IEEE Trans. Antennas Propag.*, vol. 33, no. 10, pp. 1045–1053, Oct. 1985.

[8] D. M. Pozar, "Finite phased arrays of rectangular microstrip patches," *IEEE Trans. Antennas Propag.*, vol. 34, no. 5, pp. 658–665, May 1986.

[9] D. H. Schaubert, "A class of E-plane scan blindnesses in single-polarized arrays of tapered-slot antennas with a ground plane," *IEEE Trans. Antennas Propag.*, vol. 44, no. 7, pp. 954–959, Jul. 1996.

[10] A. Ellgardt, "A scan blindness model for single-polarized tapered-slot arrays in triangular grids," *IEEE Trans. Antennas Propag.*, vol. 56, no. 9, pp. 2937–2942, Sep. 2008.

[11] Y. Fu and N. Yuan, "Elimination of scan blindness of microstrip phased array using electromagnetic bandgap structures," *IEEE Antennas Wireless Propag. Lett.*, vol. 3, pp. 63–65, 2004.

[12] L. Zhang, J. A. Castaneda, and N. G. Alexopoulos, "Scan blindness free phased array design using PBG materials," *IEEE Trans. Antennas Propag.*, vol. 52, pp. 2000–2007, Aug. 2004.

[13] G. Donzelli, F. Capolino, S. Boscolo, and M. Midrio, "Elimination of scan blindness in phased array antenna using a grounded-dielectric EBG material," *IEEE Antennas Wireless Propag. Lett.*, vol. 6, pp. 106–109, 2007.

[14] S. S. Holland, "Modeling of Photonic Bandgap Effects on Scan Blindnesses in Printed Dipole Array," in *Proc. Int. Symp. Antennas Propag. (APSURSI)*, July. 2017, pp. 1589–1590.

[15] E. Adas, F. D Flaviis, and N. G. Alexopoulos, "Realization of Scan Blindness Free Finite Microstrip Phased Arrays Based on

Mode-Free Radiating Electromagnetic Bandgap Materials,” IEEE Trans. Antennas Propag., vol. 66, pp. 3375–3382, July. 2018.

[16] Z. Xu, C. Zhang, T. Kaufmann, X. Yan, Y. Yuan, and C. Fumeaux “Analysis of Scan Blindness in a Linearly Polarized Tapered-Slot Phased Array in Triangular Lattice— Performance Improvement with Parasitic Notches”. IEEE Trans. Antennas Propag., Vol. 62, No.8, pp. 4057–4066, Aug. 2014.

[17] J. T. Logan, R. W. Kindt, and M. N. Vouvakis, “A 1.2–12 GHz Sliced Notch Antenna Array,” IEEE Trans. Antennas Propag., vol. 66, pp. 3375–3382, April. 2018.

[18] A. Eldek, Atef Z. Elsherbeni, and Charles E. Smith. “Wide-Band Modified Printed Bow-Tie Antenna with Single and Dual Polarization for C- and X-Band Applications” IEEE Trans. on Antennas and Propagat. VOL. 53, NO. 9, Sep. 2005.

[19] K. Leong, Y. Qian and T. Itoh, “Surface-Wave Enhanced Broadband Planar Antenna for Wireless Applications,” accepted for publication in IEEE Microwave and Wireless Components Letters, Feb. 2001.

[20] S. Maci, L. Borselli, and L. Rossi, “Diffraction at the edge of a truncated grounded dielectric slab,” IEEE Trans. Antennas Propagat., vol. 44, pp. 863–873, June 1996.

[21] S. Maci, L. Borselli, and A. Cucurachi, “Diffraction from a truncated grounded dielectric slab: A comparative full wave/physical optics analysis,” IEEE Trans. Antennas Propagat., vol. 48, pp. 48–57, Jan. 2000.

Chapter 2. Analysis of Scan Blindness in a T-Printed Dipole Array

2.1. Motivation

In this Chapter, the mechanism of scan blindness in T-printed dipole array is described, and an effective scan blindness elimination strategy is proposed. The T-printed dipole structure can support a wave that propagates along the E-plane, which resembles the quasi-TEM mode of a rectangular mushroom structure proposed in [1]. Further, this quasi-TEM analysis has been used to quickly and accurately calculate the dispersion curves [2].

Scan blindness is observed using an active element pattern (AEP) and active reflection coefficient [3], [4]. From the electric field (E-field) distribution at the scan blind angle in the E-plane, an equivalent circuit model for a unit cell is proposed and the equation for the dispersion relations is derived using the transmission line (TL) theory [2], [5], which has been used successfully to calculate the dispersion relations for two-dimensional (2D) periodic structures [6], [7]. The dispersion diagram is also used to verify the existence of the guided mode in the T-printed dipole, which is a proper method to find resonant frequencies in periodic structures.

We propose the T-printed dipole model to eliminate the guided

wave effect, and compare it to the conventional model. In 2015, a radio frequency choke (RFC) using modified stubs was developed to improve the isolation characteristics of multiple input multiple output (MIMO) antennas [6]. In 2017, Ta et al. proposed inserting a microstrip stub between two printed angled-dipole antennas to improve the scanning angle range, bandwidth, radiation efficiency, and mutual coupling [8], [9]. However, the specific mechanism by which the stub could reduce the mutual coupling and widen the scan range is not explained. In this paper, the role of slits and stubs is discussed in terms of the scan blindness and suppression of the guided wave. These parasitic elements are applied to the T-printed dipole to eliminate scan blindness effectively.

2.2. Study on Single Element Design

A T-printed dipole element has low profile, light weight, low cost, and compact size, and is widely used for building phased arrays. Fig. 2.1 shows the configurations of a basic T-printed dipole element and the proposed one. These models are modified from the original model proposed in [8]. The substrate used in the proposed design is RT/Duroid Rogers 5880 with a relative permittivity of 2.2 and dielectric loss tangent of 0.009. The thickness of the dielectric and copper are 0.254 mm and 0.017 mm, respectively. The feedline consists of a microstrip and the balun, which are printed on the front

of the substrate. The dipole and the ground are at the back of the substrate. Impedance matching is achieved by adjusting the folded line and the gap of the slot (W_s). The design values for the geometric parameters of the structure are described in Table I. In order to improve the E-plane scanning characteristics of the printed dipole array, stubs and slits are added between the two printed dipole antennas in the proposed design, as illustrated in Fig. 2.1(b). The length of the stub is determined in accordance with Alhalabi and Rebeiz [9]. Slits are added at both sides of the feedline to the T-printed dipole element to complement the stubs. The role of the parasitic elements is described in detail in subsection 2.8.

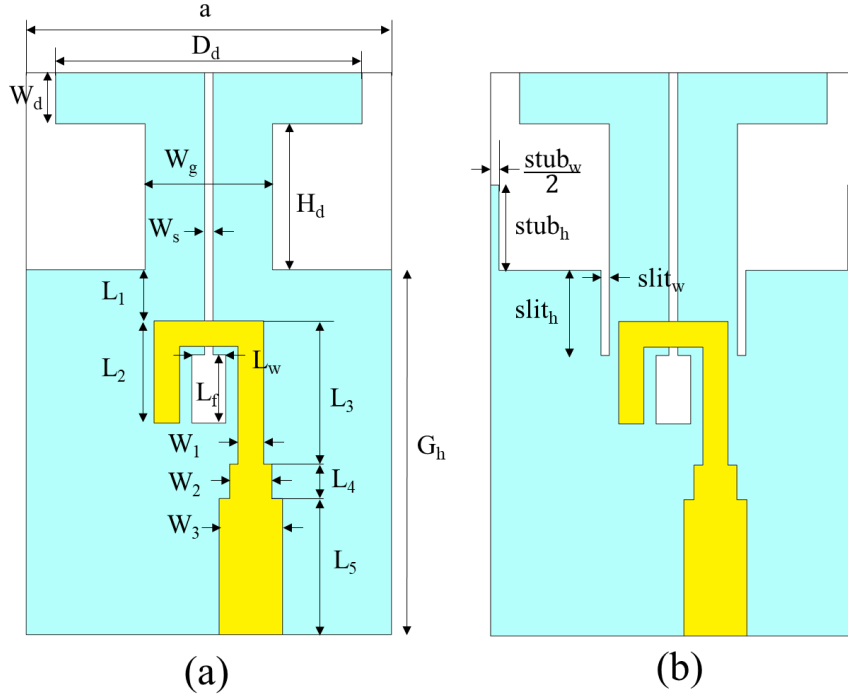


Fig. 2.1. Geometry of an element: (a) Basic T-printed dipole, and (b) T-printed dipole with slits and stubs.

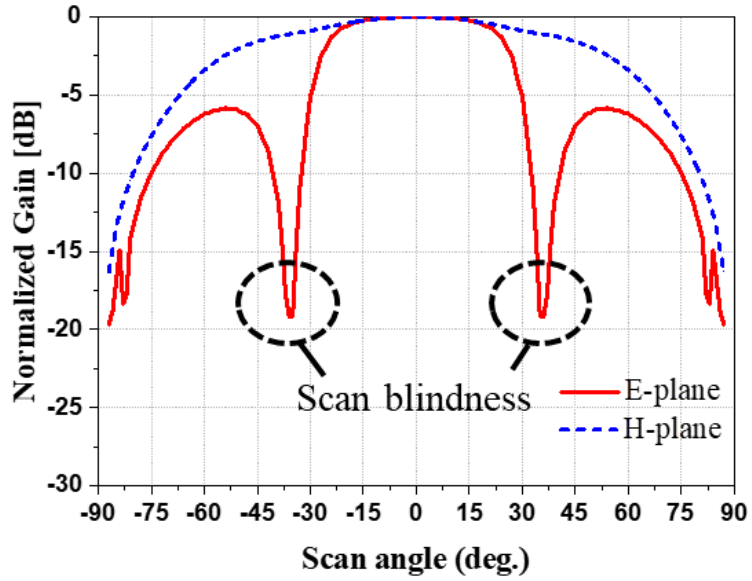
TABLE 2.1
DESIGN PARAMETERS OF T-PRINTED DIPOLE ELEMENT

D_a	W_d	W_g	W_s	W_{h1}	W_{h2}	W_{h3}
3.6	0.6	1.5	0.01	1.29	0.4	1.6
W_1	W_2	W_3	L_f	L_w	L_1	L_1
0.3	0.5	0.74	0.8	0.4	0.6	1.2
G_h	$stub_h$	$stub_w$	$slits_h$	$slit_w$	G_h	a
4.285	1	0.1	1	0.1	4.285	4.285

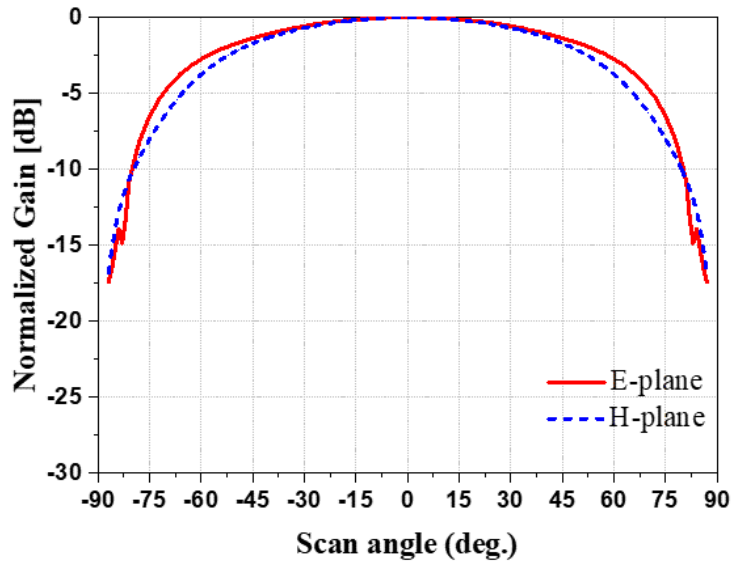
(Unit: mm)

2.3. Active Element Pattern in Infinite Array

The AEP is a good indicator for predicting the scan blindness of a phased array [3], [6]. The patterns used in our work are obtained using an electromagnetic simulator, CST Microwave Studio. A rectangular lattice is selected, with an element spacing “a” of $0.5 \lambda_0$ (where λ_0 is the free space wavelength) in the E and H-planes, to avoid a grating lobe. The AEP in an infinite array for a basic T-printed dipole is obtained in the E and H-planes as shown in Fig. 2.2 (a). The pattern in the E-plane shows scan blindness at $\pm 36^\circ$, and decays sharply near the blind angle, which is quite different from the behavior of the H-plane pattern. Fig. 2.2 (b) illustrates the AEP in an infinite array with slits and stubs. The scan blindness in the E-plane is eliminated, and the pattern in the H-plane shows little change when compared to Fig. 2.2 (a).



(a)

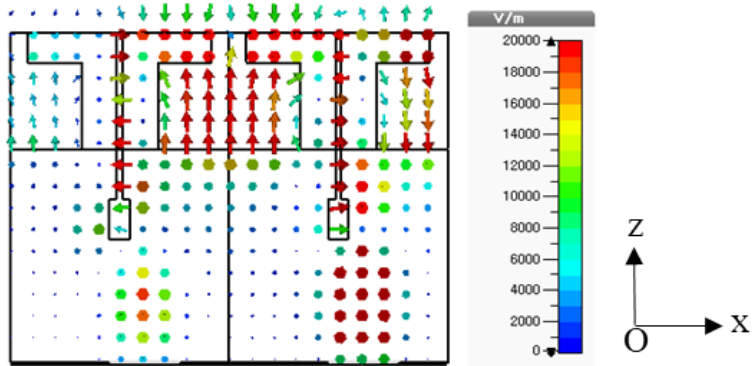


(b)

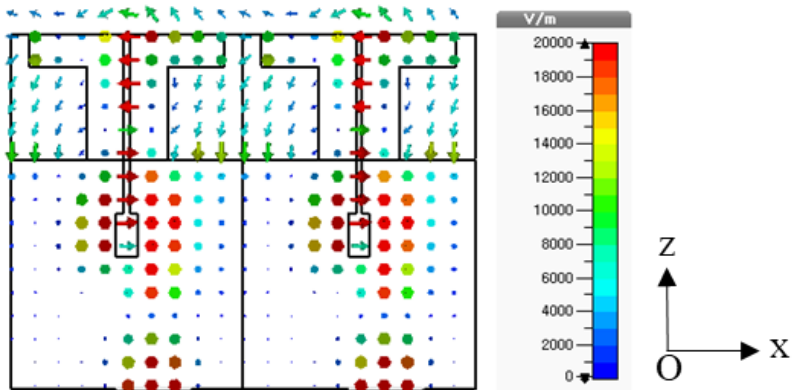
Fig. 2.2. Active element pattern in an infinite array (Comparison of E-plane and H-plane): (a) Basic T-printed dipole, and (b) T-printed dipole with slits and stubs.

2.4. E-field Distribution in Infinite Array

The E-field distribution in the infinite array is obtained by Floquet excitation. Fig. 2.3(a) shows the E-field distribution in the infinite array when Floquet excitation is performed such that the incident angle is the blind angle. Fig. 2.3(b) illustrates the E-field distribution when the elements are excited with uniform amplitudes without phase progression to steer the bore sight angle. The amplitude of the E-field in Fig. 2.3(a) is considerably higher than that in Fig. 2.3(b). The E-field in Fig. 2.3(a) is coupled strongly between two dipole arms and it is different from the fields at the other angles. When scan blindness occurs, only the z-direction component of the E-field is present, and the wave propagates in the x-direction. Thus, the dipole arms and ground plane operate as a transmission line. These guiding fields are described as the quasi-TEM mode.



(a)



(b)

Fig. 2.3. E-field distribution between two dipoles in infinite array when Floquet excitation is performed so that the incident angle is (a) blind angle (36°) and (b) boresight angle (0°).

2.5. Dispersion Diagram

To understand the relationship between the scan blindness and the dispersion properties of a unit cell of the basic T-printed dipole element, two types of simulations were carried out. The first simulated a trajectory of the scan blindness for an AEP in an infinite array, according to the frequency change. The AEP is expressed in terms of the active reflection coefficient, also known as the Floquet reflection coefficient (Γ^{FL}) if no grating lobe exists for the infinite array under Floquet excitation [10]. Thus, the active element gain G_{AEP} could be expressed as

$$G_{AEP} = \frac{4\pi A_{unitcell}}{\lambda_0^2} \sin \theta \times [1 - |\Gamma^{FL}|] \quad (2.1)$$

here $A_{unitcell}$ is a unit cell area. The scan blind angle can be verified from the singularity point traces of the active reflection coefficient in the infinite array, by sweeping the frequencies. Under such a condition, the amplitude of the guided wave increases, resulting in a very large input impedance and very poor matching. Thus, the active reflection coefficient converges to one, causing scan blindness [3]. The second is an eigen mode simulation to determine the resonances and dispersion properties of the unit cell. For the eigen mode analysis, the periodic boundary conditions (PBCs) are applied in both the x and y directions with a unit cell size “a” (4.285 mm). Only the phase shift

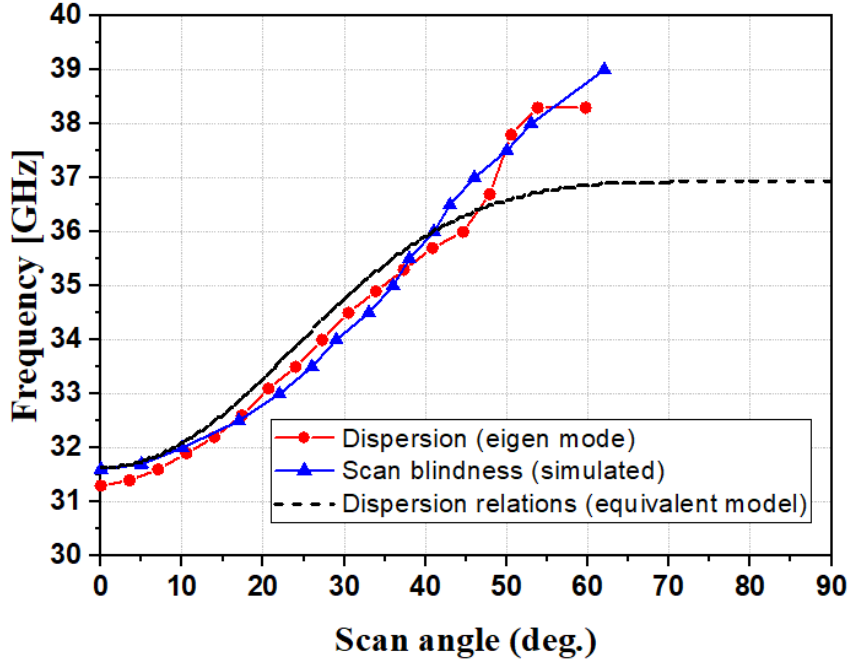


Fig. 2.4. Simulated dispersion diagrams of eigen mode, trajectory of scan blindness, and calculated dispersion relations obtained from Appendix A.1.

along the x -direction is considered because of the E -plane scanning. The trajectories of the scan blindness and dispersion properties are in good agreement, as shown in Fig. 2.4. The relationship between a propagation constant of the unit cell (β_{unit}) and a scan angle (θ_{scan}) can be expressed as

$$\beta_{unit} = k_0 \sin \theta_{scan} \quad (2.2)$$

In the dispersion diagram obtained from the eigen mode simulation, when the scan angle is 36° , the resonant frequency is 35

GHz, which corresponded to the scan blindness shown in Fig. 2.3. These results support the hypothesis that the propagation constant of a TEM guided mode coincides with that of a radiation mode, then two modes lead to a resonance and subsequent scan blindness.

2.6. Guided quasi-TEM mode

To support the guiding of the quasi-TEM mode, Fig. 2.5 shows the E-field simulation of the coupling between linear infinite dipole arrays placed 10 unit cells apart, describing the E-field magnitude of a T-printed dipole array in the E-plane. The PMC boundary to the y-direction is applied using the CST simulator, to implement an infinite array. Ports are set on both sides of the eleven-element array in the x-direction. Port 1 is excited to examine the E-field distribution guided along the antenna. It is observed that the guided wave is traveling in the direction of the antenna row when the antenna elements are coupled to each other. This simulation shows that the row of T-printed dipoles operates as a transmission line supporting the quasi-TEM mode.

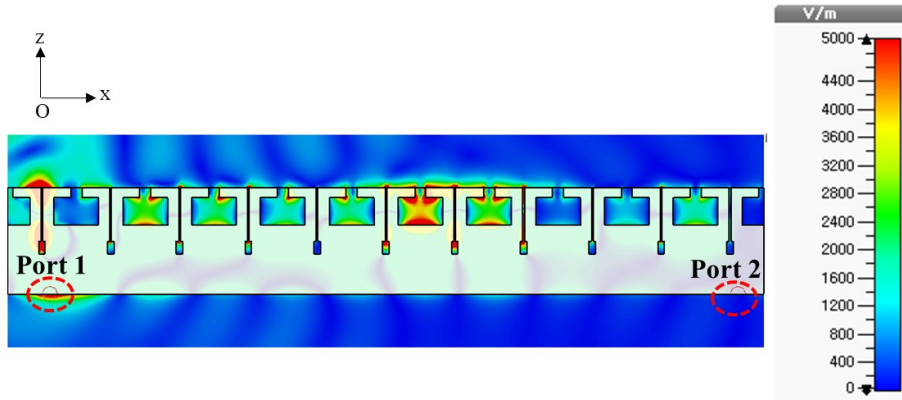


Fig. 2.5. Electric field distribution of coupling between linear infinite dipole arrays placed 10 unit cells apart at 35 GHz for basic T-printed dipole array.

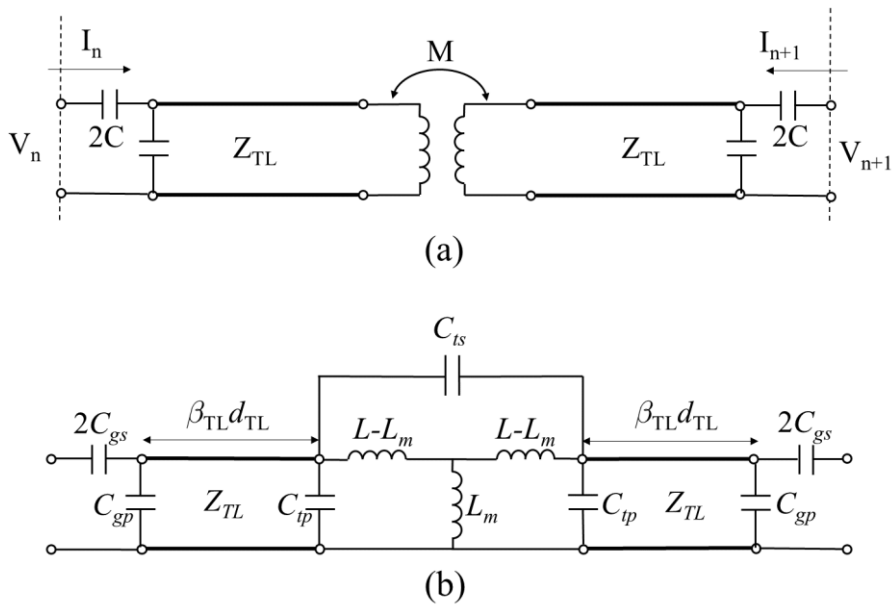


Fig. 2.6. (a) Equivalent topology of a T-printed dipole unit cell, and (b) Transformed equivalent circuit.

2.7. Equivalent Circuit

Based on the observation of the dispersion properties in Fig. 2.4 and the quasi-TEM wave propagation to the x-direction in Fig. 2.5, the basic topology of the unit cell could be expressed as shown in Fig. 2.6(a). For simplicity, only a one-dimensional (1D) equivalent circuit is considered, as the propagation constant $\beta_y = 0$ in the E-plane direction [26]. This topology is composed of a series capacitance, transmission line, and transformer. Its equivalent circuit is depicted in Fig. 2.6(b). A gap capacitance for series (C_{gs}) is characterized between two adjacent printed dipole arms and a gap capacitance for parallel (C_{gp}) occurs due to discontinuity from the edge. The printed dipole arms are considered to be similar to a transmission line along the x-direction, forming a quasi-TEM mode, which is described by the characteristic impedance Z_{TL} and propagation constant β_{TL} of the transmission line. The E-field is coupled to the adjacent dipole through the feeding line and the energy is guided along the row of antenna elements, as shown in Fig. 2.5. Hence, the antenna feeding network operates as a transformer. A mutual inductance (L_m) and self-inductance (L) are used to represent the transformer. C_{tp} is a parasitic shunt capacitance arising from the discontinuity between the transmission line and transformer. C_{ts} is a parasitic series capacitance that occurs because of the antenna feeding line. Using the equivalent circuit proposed in Fig. 2.6(b), the equation for the

dispersion relation is derived based on the TL theory [5]. β_{unit} is determined using the 1D periodic circuit network according to [6], [7]. The components in the unit cell are extracted from the ABCD matrix using the simulator and de-embedding methods [7]. Using the values of the elements obtained in Appendix, the dispersion relation curve is obtained as the dashed line in Fig. 2.4, which is compared with the trajectory of the scan blindness (blue line) and the eigen mode curve (red line). As the scan angle increases, the theoretically calculated results differ from the simulated or measured results. This could be because the quasi-TEM mode and the higher order mode are considered for the eigen mode simulated results, whereas the theoretical curves support only the quasi-TEM assumption. Within 45° , the calculation results fit well with those of the measurement and simulation.

2.8. Parasitic Elements for Eliminating Scan Blindness

To improve the scan performance of the printed dipole array, in the E-plane direction, a slit and stub structure is proposed, as shown in Fig. 2.1(b). The effect of the parasitic elements is confirmed by the active reflection coefficient and E-field distribution of the quasi-TEM guided wave. The resonance frequencies of the guiding mode, with and without the parasitic structures, are verified using the dispersion diagram.

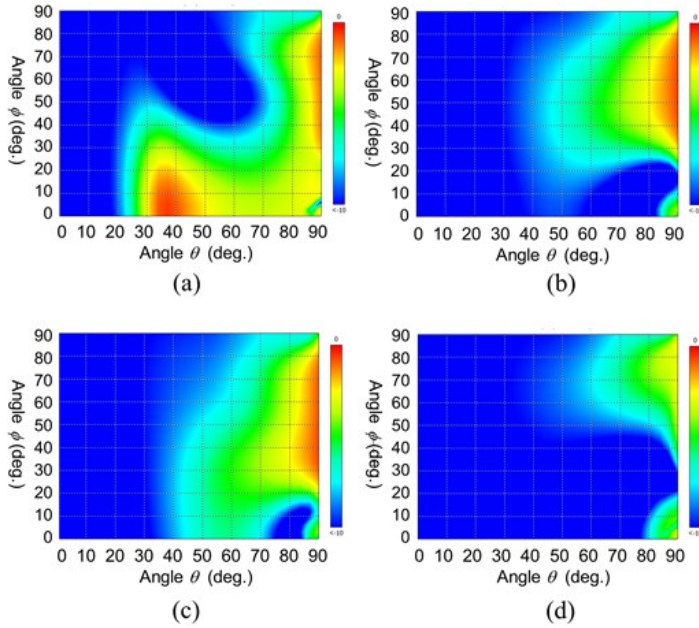


Fig. 2.7. Comparison of four types of two-dimensional active reflection coefficients: (a) basic T-printed dipole, (b) with stubs, (c) with slits, and (d) with slits and stubs.

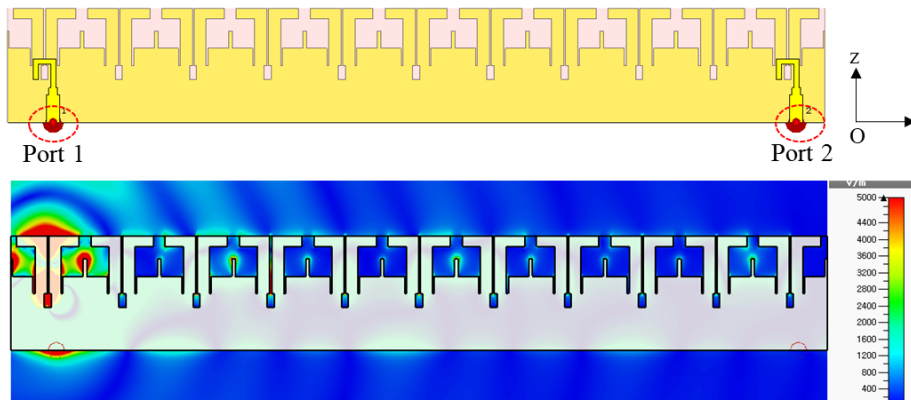


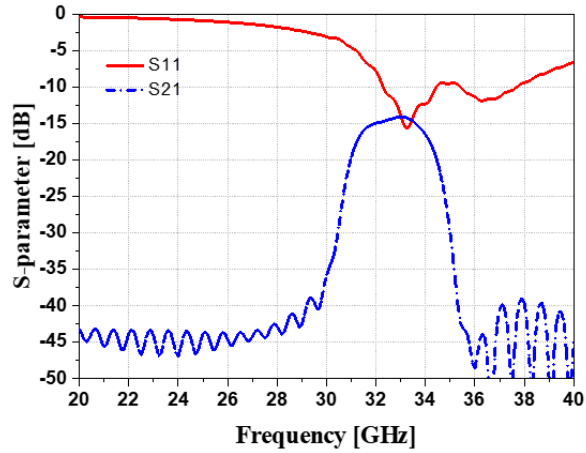
Fig. 2.8. Electric field distribution of coupling between linear infinite dipole arrays placed 10 unit cells apart at 35 GHz for basic T-printed dipole array.

2.8.1 Comparison of Active Reflection Coefficients

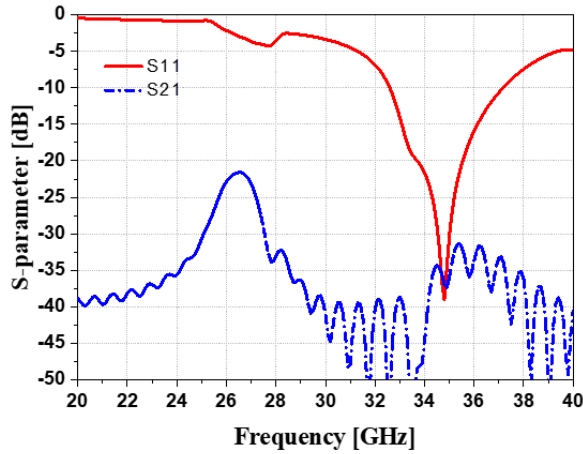
The simulated active reflection coefficients for four cases in the 2D infinite array are shown in Fig. 2.7. The blue part indicates that the active reflection coefficient is less than -10 dB. Fig. 2.7(a) indicates that reflection occurs around $\varphi = 0^\circ$, $\theta = \pm 36^\circ$ for a basic T-printed dipole, which is the scan blindness in the E-plane. To eliminate the scan blindness effect, three configurations of parasitics are considered. The first case is an element with stub, as depicted in Fig. 2.7(b). The second case is an element with slit, as depicted in Fig. 2.7(c). The third case is the elements with slits and stubs, shown in Fig. 2.7(d). The graph shows that the reflection coefficient is less than -10 dB for all φ directions and θ within $\pm 45^\circ$, which is the best case among the four types in Fig. 2.7.

2.8.2 Guiding Wave Suppression

The presence of a guided wave is discussed in subsection 2.4~2.6. To observe the changes to the guided wave, caused by the parasitic structures, slits and stubs are added to the original array model depicted in Fig. 2.5. When Port 1 is excited, the amplitude of the E-field in the proposed array is suppressed, as shown in Fig 2.8. This indicates that the stubs and slits play a significant role in impeding the quasi-TEM guided wave along the printed dipole array in the E-plane. An S-parameter graph is depicted in Fig. 2.9. Fig.



(a)



(b)

Fig. 2.9. S-parameter comparison of (a) basic T-dipole array, from Fig. 5, and (b) T-dipole with slits and stubs as parasitic structures, from Fig. 2.8.

2.9(a) describes the S-parameter characteristics for Fig. 2.5. The transmission coefficient is improved from -25 dB to -35 dB at 35 GHz, as shown in Fig. 2.9(b). Decreasing the amplitude of the guided wave, using parasitic structures, reduced the mutual coupling and improved the return loss.

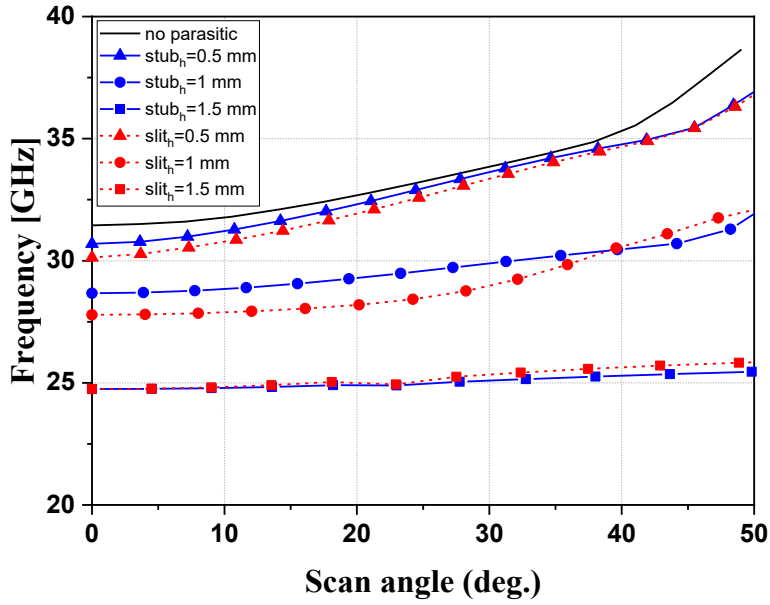


Fig. 2.10. Simulated dispersion diagram of eigen mode for different length of the slit (slith) and stub (stubh).

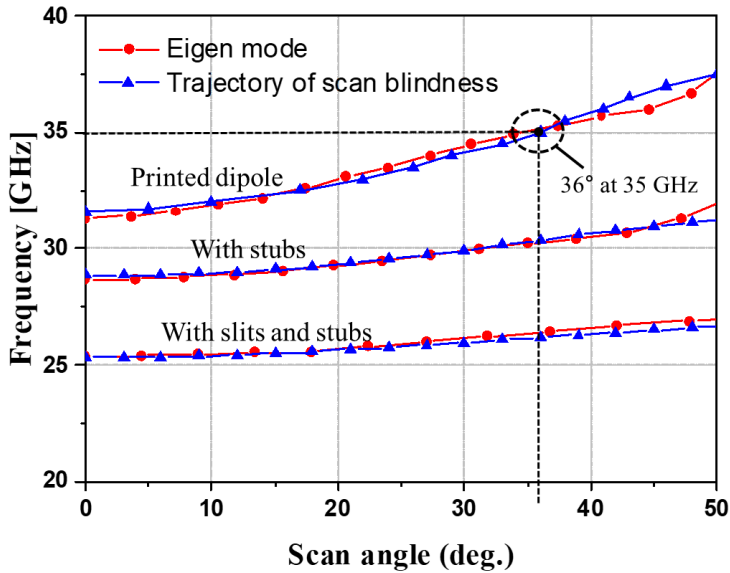


Fig. 2.11. Electric field distribution of coupling between linear infinite dipole arrays placed 10 unit cells apart at 35 GHz for basic T-printed dipole array.

2.8.3 Comparison of Dispersion Relations

To understand the propagation and suppression characteristics of the guided wave along the printed dipole, a dispersion diagram is used, as described in Fig 2.10. The dispersion diagram shown in Fig. 10 is the result of parametric studies on the length of slits and stubs. The idea of inserting stub structures between printed dipoles is proposed in [1]; these can be equalized with an LC resonator to suppress leakage current [10]. The stubs and slits are characterized by a shunt capacitance (C_{shunt}) and series inductance (L_{series}), respectively. As L_{series} and C_{shunt} are added, β_{unit} is increased, which has the effect of lowering the resonance frequency of the quasi-TEM mode. Consequently, as the length of the stub or slit becomes longer in Fig. 2.10, C_{shunt} or L_{series} increases, such that the dispersion curve moves toward lower frequencies. At this time, if the length of the slit or stub exceeds 1 mm, the parasitic structure acts as a resonator, which affects the radiation pattern. Thus, the length of the parasitic element is determined to be 1 mm in order to avoid the resonance of the quasi-TEM mode at a given design frequency. Fig. 2.11 shows the results of the trajectory of scan blindness in an infinite array and the simulated dispersion diagram of eigen modes for the three structures. The first structure is a basic printed dipole element. The second is a unit cell with stubs. The third structure is one wherein the stubs and slits are inserted in a unit cell,

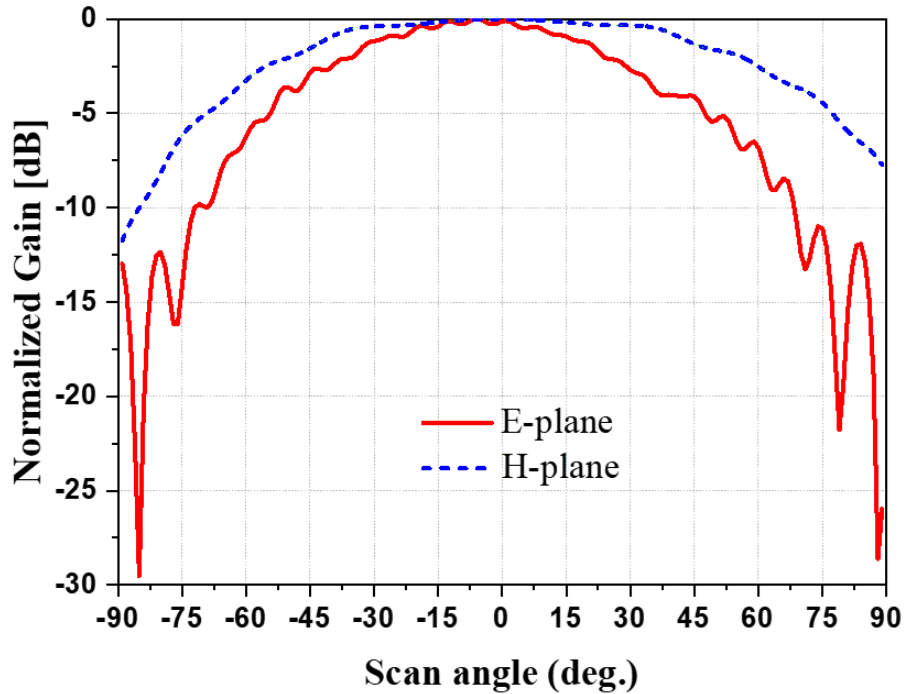


Fig. 2.12. 1D Active element pattern.

supplementing the stub structures. The third case shows that the resonant frequencies are shifted to a value lower than when only the stub structures are present.

2.9. 1D Array Analysis

Fig. 2.12 shows AEP in E and H-plane for 1D array. At this time, an AEP is obtained by using the radiation pattern of the element in the center of a 1D array (21 elements), which is sufficiently large. In the case of a 1D array, scan blindness does not occur in both the E

and H-plane. To check the resonance characteristics, dispersion relations for the unit cell are obtained using eigen mode simulation of HFSS. For a 1D array, a periodic boundary condition is set in the x-axis direction and a perfect matched layer (PML) is set in the y-axis direction. When the dispersion relations of the unit cell for 1D and 2D arrays and the scan blindness diagram are compared as shown in Fig. 2.13, all three graphs are matched well. To analyze the loss of two unit cells for 1D and 2D arrays, calculate the Q value for the phase difference of the unit cells as shown in Fig 2.14. At this time, the Q value corresponds to the frequency and phase difference of the dispersion relations obtained in Fig. 2.13. The Q value of the unit cell for the 1D array is formed between 1 and 10, whereas the value for the 2D array is over 1,000. In particular, when the phase difference of the unit cell is calculated using equation (1), 36° , which is the angle at which scan blindness occurs at the target frequency, it becomes about 108° , where the Q value of the unit cell in the 1D array is 1.4, In, the Q value of the unit cell is 2438. This means that the 1D array has more external losses than when the resonance mode energy is 2D array.

In 1D array and 2D array, two types of simulation are conducted as shown in Fig. 2.15 to investigate the external loss and coupling effect of the printed dipole. Fig. 2.15 shows 11 printed dipole elements arranged in a line. In addition, port 1 and port 2 are set at both ends of the element, and the amplitude of the field going between the two ports can be observed. In Fig 2.15(a), in order to equalize the 1D

array, the open boundary is set so that the distance is $0.5 \lambda_0$ in the H-plane direction. In the case of open boundary, it shows that the electric field is not well guided and attenuated. In Fig. 2.15(b), in order to implement a 2D array, it can be equalized with a perfect magnetic wall (PMC) so that the distance is $0.5 \lambda_0$ in the H-plane direction. When power is excited to port 1, it shows the amplitude of the guided electric field along the dipole column as shown in Fig. 2.15(a). In the structure of Fig. 5, the mutual coupling can be verified through the S-parameter as shown in Fig. 2.16. In the case of the open boundary at 35 GHz, the S21 value is -38.9 dB, whereas at the PMC boundary, the value of S21 is -30 dB, and the amount of mutual coupling increases by 9 dB from the open boundary. The scan blindness is difficult to occur in a 1D array unlike a 2D array. Because the radiation loss increases as the field induced in the E-plane direction loses energy to the open boundary, and the Q value decreases. At the same time, the guided mode that propagates along the antenna row is attenuated, reducing mutual coupling as shown in Fig. 2.15.

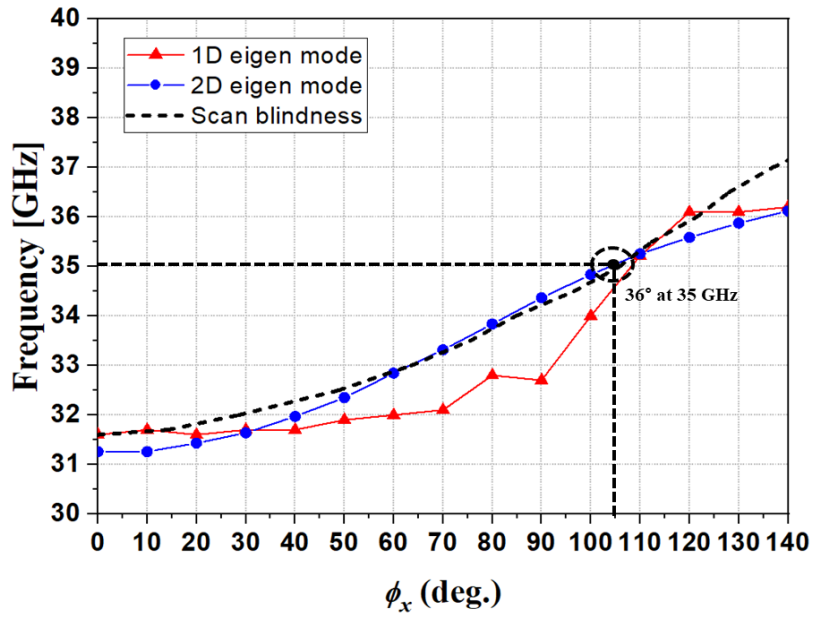


Fig. 2.13. Dispersion relations comparison between eigen mode simulation and scan blindness.

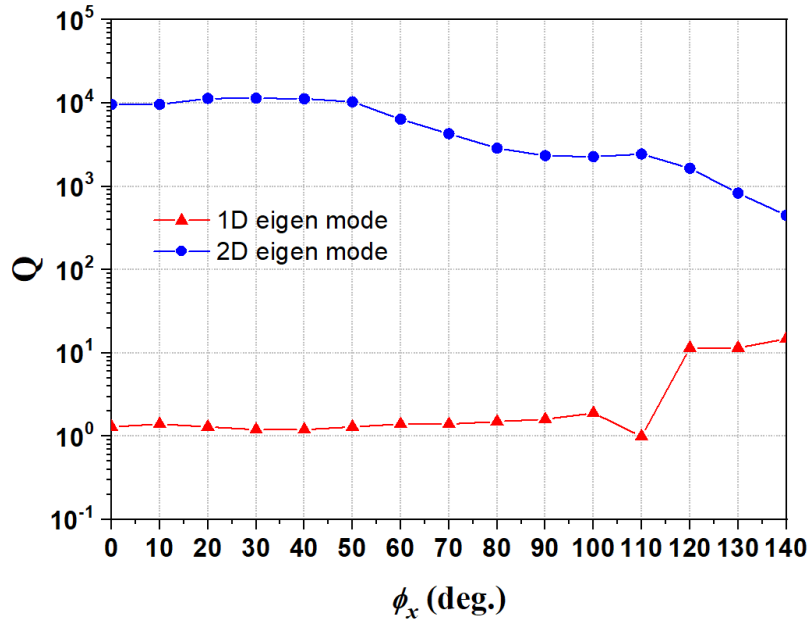
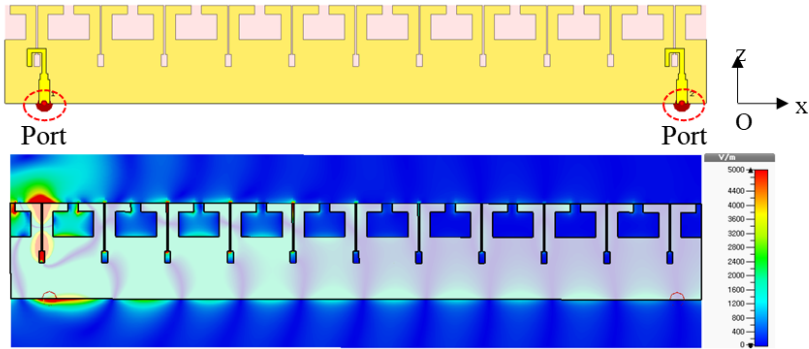
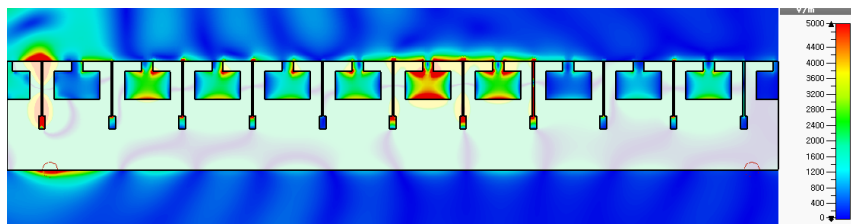


Fig. 2.14. Q factor comparison between 1 D and 2 D.



(a)



(b)

Fig. 2.15. Electric field simulation of coupling between linear dipole arrays placed 9 unit cells apart for open boundary. (a) Open boundary and (b) PMC boundary.

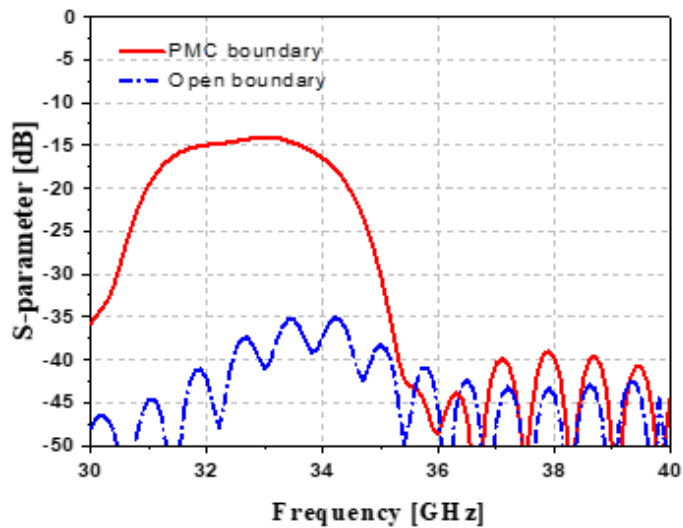


Fig. 2.16. S-parameter between linear dipole arrays placed 9 unit cells apart.

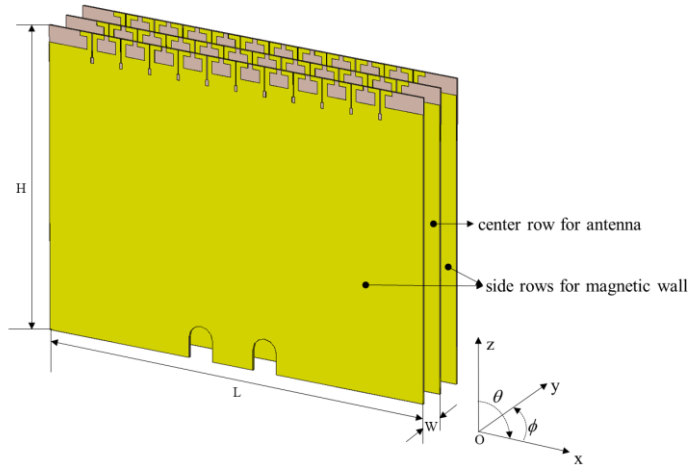


Fig. 2.17. Geometry of 11×3 basic T-printed dipole array for a finite active element pattern.

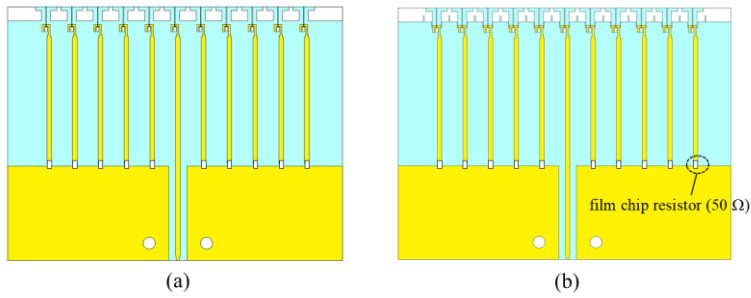


Fig. 2.18. Structure of an active element pattern of the 11×3 array. (a) Basic printed dipole. (b) Proposed.

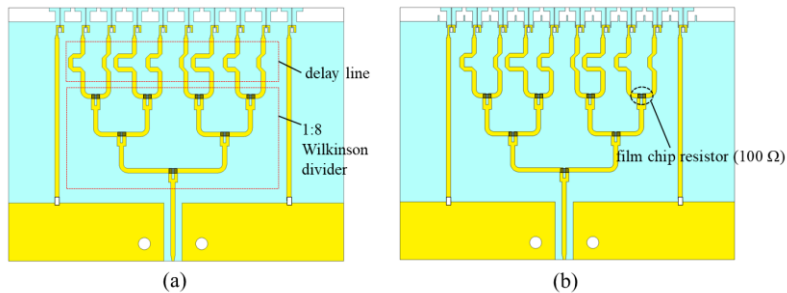


Fig. 2.19. Structure of fully excited 8×1 arrays in E-plane with 41° scan angle: (a) Basic printed dipole, and (b) Proposed.

2.10. Finite Array and Measurements

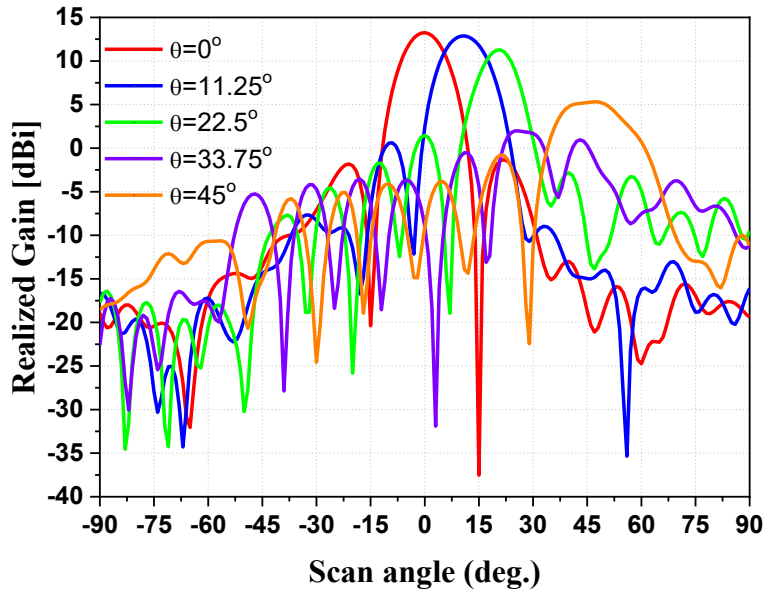
2.10.1 Physical Explanation for Finite Array

In the previous section, the scan blindness mechanism for infinite arrays of T-printed dipole has been discussed. Using stubs and slits, the scan blindness phenomenon is improved for the E-plane, but there is almost no pattern change for the H-plane. Therefore, for the purpose of measuring only the E-plane, the geometry of an 11×3 basic T-printed dipole array for a finite AEP is proposed in Fig. 12. The design parameters are: $L = 42$ mm, $W = 30$ mm and $D = 4.28$ mm. First, two types of 11×3 finite T-printed dipole arrays are illustrated in Fig. 2.17. The AEP structures based on the basic printed dipole model and the proposed elements are presented in Fig. 2.18(a) and Fig. 2.18(b), respectively. For AEP implementation, a center element of the middle row substrate is excited, and all other elements are matched and terminated with 50Ω thin-film chip resistors (0402 size, Vishay). Similarly, all elements of the first and third substrate are matched and terminated with 50Ω chip resistors so that the two substrates worked as a magnetic wall. The other two types of antennas consist of 10×3 elements, but these operate as an 8×1 array. The substrate located in the middle row consists of eight excited elements and two matched terminated elements. In the case of a finite array, the AEP of the element near the edge differs from that of the center element [11]. Therefore, the edge elements of the

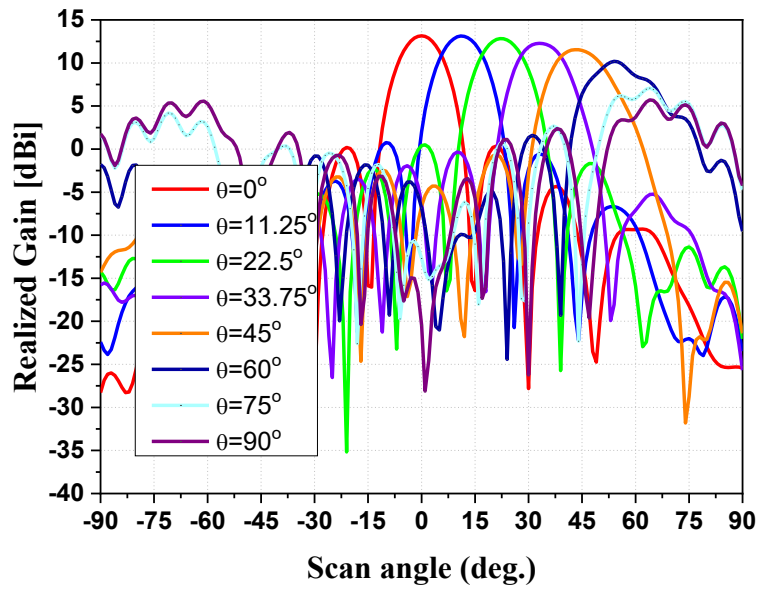
substrate are used as dummy elements to preserve the uniformity of the AEP of the feeding elements, as shown in Fig. 2.19. Elements of the first and third rows of the array are terminated with 50Ω , similar to the AEP structures. The design model in Fig. 2.19(a) is realized as a basic printed dipole array and the second one in Fig. 2.19(b) depicted a printed dipole array with slits and stubs. A 1:8 Wilkinson divider is designed for Floquet excitation so that each element is isolated and excited uniformly. The microstrip delay line in the feeding is a phase shifter. The phase difference of each device is 120° at 35 GHz, making the scan angle of the designed array 41° , which is close to the scan blind angle of 36° . Chip resistors are used for matched termination, similar to the finite AEP structure mentioned above.

2.10.2 Scanning Performance

Fig. 2.20 shows the scanning performance of the 11×3 arrays with an excited 8-element linear array for the basic printed dipole and proposed printed dipole, respectively. The array is fed to the same amplitude and scanned at 11.25° intervals by controlling the phases at eight-ports. In Fig. 2.20(a), when the scan angle is 33.75° near the scan blind angle, the co-polarization realized gain pattern is deteriorated by the scan blindness effect. On the contrary, the pattern is improved as shown in Fig. 2.20(b), using the slits and the stubs.



(a)



(b)

Fig. 2.20. Simulated scanning performance in the E-plane for the 11×3 arrays with an excited 8-element linear array: (a) Basic printed dipole, and (b) Proposed.

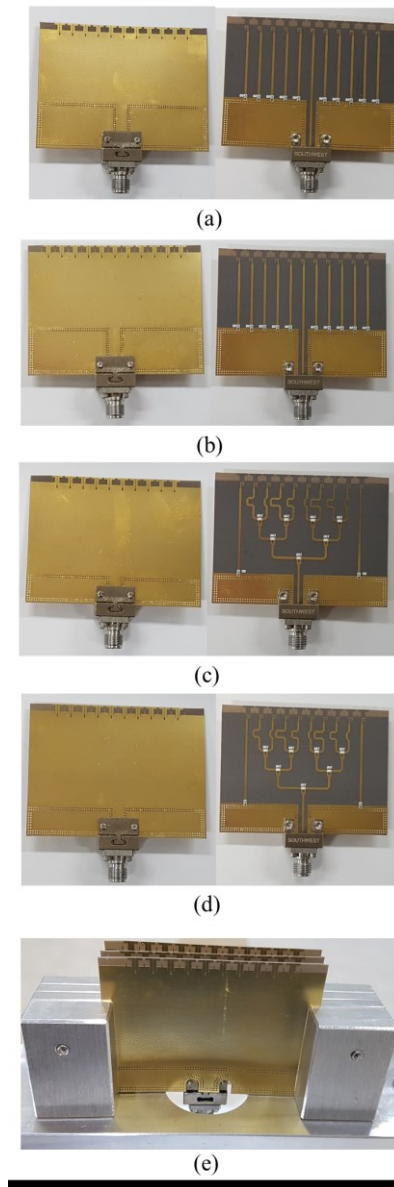
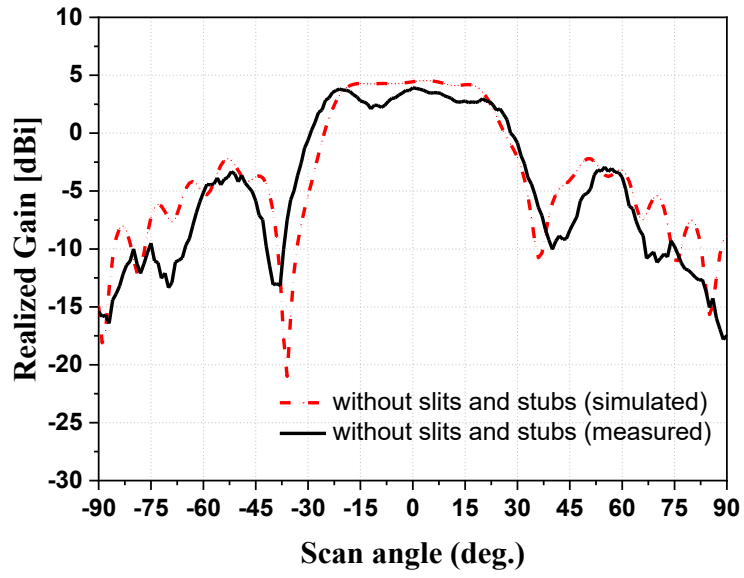


Fig. 2.21. Four types of center row substrate arrays fabricated: (a) Active element pattern (AEP) of the 11×3 arrays for the basic T-printed dipole, (b) AEP of the 11×3 arrays for the proposed T-printed dipole, (c) Fully excited 8×1 arrays for the basic T-printed dipole, (d) Fully excited 8×1 arrays for the proposed T-printed dipole, and (e) Array of printed dipoles with slits and stubs mounted on the antenna bracket.

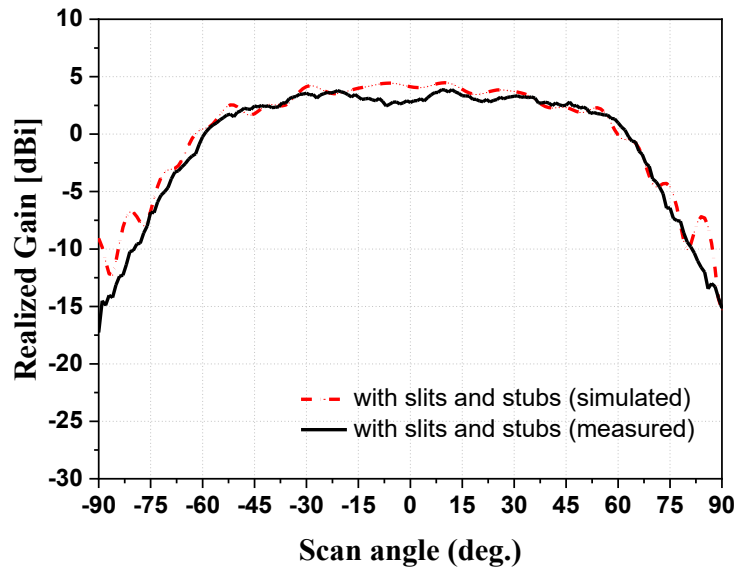
2.10.3 Simulations and Measurements

As explained in the previous section, four types of prototypes were fabricated and measured. Fig. 2.21(a)–(d) show the front and back views of the center row substrates with end launch connectors (type 2.92 mm). Fig. 2.21(e) depicts a photograph of the 11×3 T-printed dipole array with slits and stubs for finite AEP mounted on an antenna bracket made of aluminum. To validate the simulation results, experiments were performed in a far-field anechoic chamber. Fig. 2.22(a) and (b) present the finite AEP simulated and measured in the E-plane at a fixed frequency for a basic T-printed dipole array and the proposed array, respectively. Scan blindness around $\pm 36^\circ$ is observed in both the measured and simulated results in Fig. 2.22(a). Fig. 2.22(b) illustrates that the scan blindness is eliminated in the AEP. The scan range of the AEP is $\pm 57^\circ$. At the broad side, the realized gain is 4.1 dBi and 2.8 dBi for the simulated and measured values, respectively. Although a slight gain variation occurred in the measurement results owing to the scattering of the antenna bracket, the measured patterns are in good agreement with the simulated patterns. The measured and simulated realized gains were obtained as illustrated in Fig. 2.23, which shows the fully excited array for scanning toward 41° in the E-plane. Fig. 2.23(a) shows that the main beam is distorted because of the scan blindness. By adding a parasitic element, as shown in Fig. 2.23(b), the gain measured is

improved by 9 dB compared to the original model. At the intended angle (41°), the realized gain is 10.6 dBi and 11.7 dBi for the simulated and measured values, respectively. Figure 2.19(a) is the AEP measurement result for 1D array. Figure 2.19(b) is the AEP result with slit and stub. It shows that the beam characteristics are improved due to resonant mode shift. Fig. 2.25 shows the measurements of the scan blindness traces for E-plane scanning obtained by sweeping the frequencies from 32.5 GHz to 37 GHz with 0.25 GHz intervals. The measured data are matched with the eigen modes simulated for a basic T-printed dipole. From the results in Fig. 2.25, it can be inferred that the quasi-TEM wave guided along a row of T-printed dipole elements is the main cause of the scan blindness.

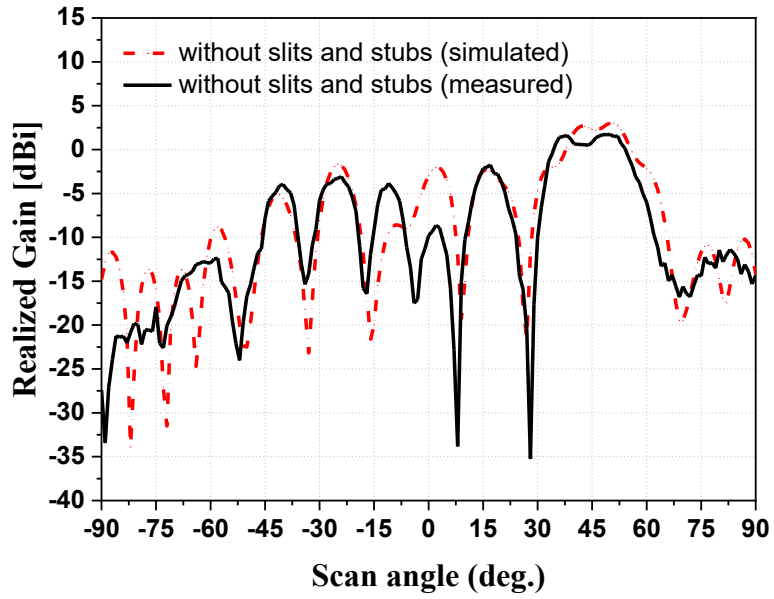


(a)

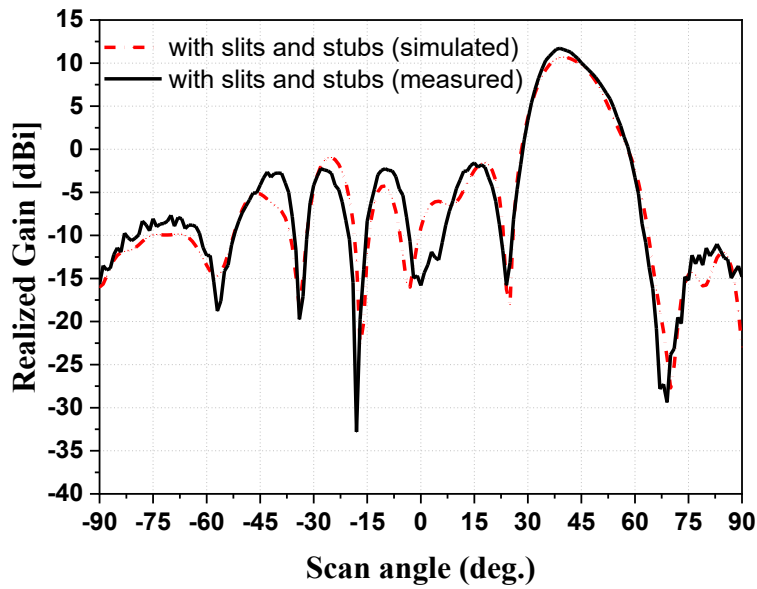


(b)

Fig. 2.22 E-plane co-polarization active element pattern of the 11×3 arrays: (a) Basic printed dipole, and (b) Proposed

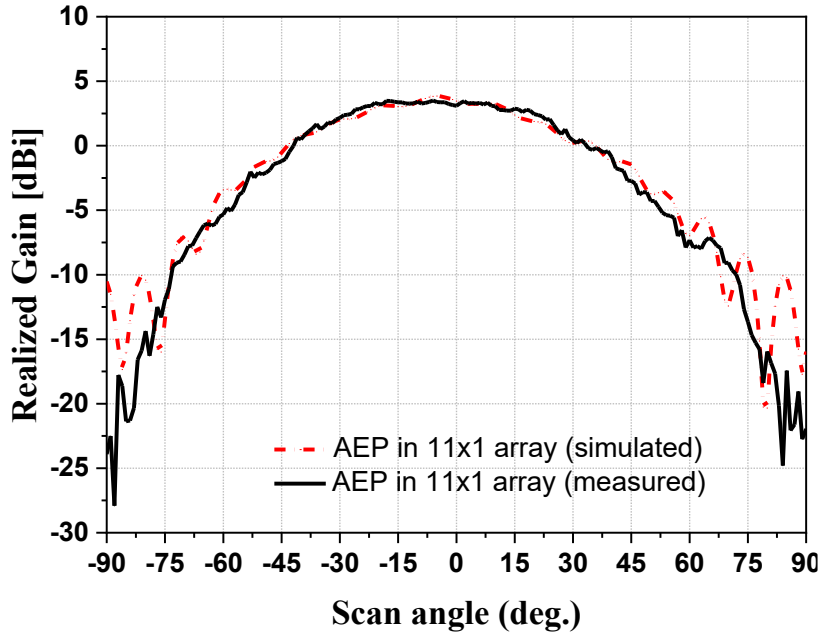


(a)

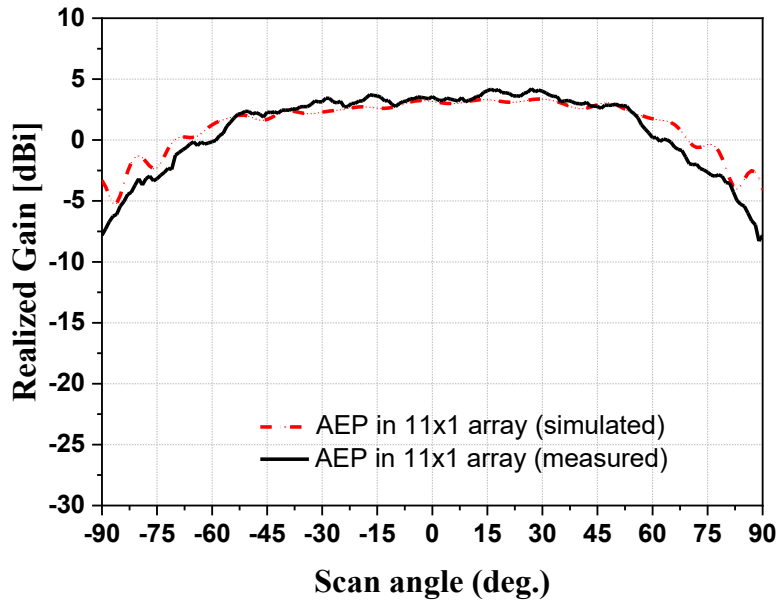


(b)

Fig. 2.23. Fully excited 8×1 arrays in E-plane co-polarization at 41° scan angle: (a) Basic printed dipole, and (b) Proposed.



(a)



(b)

Fig. 2.24. Printed Dipole AEP in the E-plane for 1-D array: (a) 11x1 sub array for printed dipole, and (b) 11x1 sub array for printed dipole with slit and stub.

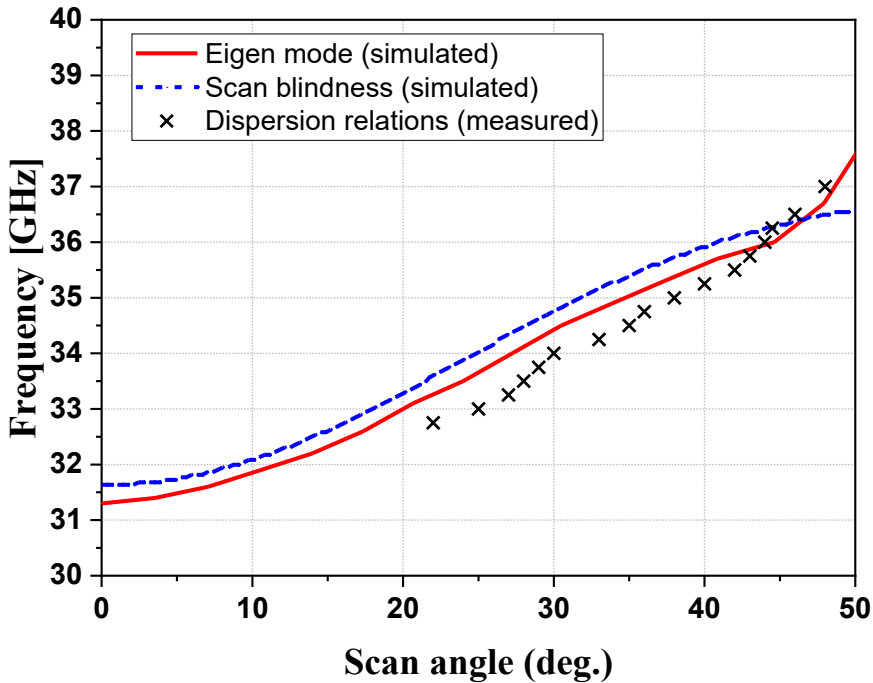


Fig. 2.25. Comparison of scan blindness occurrences when the printed dipole array antenna is steering from broadside to 50° in the E-plane. Eigen mode (simulated) vs. dispersion relations (calculated) vs. scan blindness (measured).

2.11. Conclusions

In this study, the scan blindness in the T-printed dipole was analyzed and an elimination technique proposed. The main cause of the scan blindness was found to be a quasi-TEM guided wave mode traveling along the printed dipole substrate in the E-plane through an infinite rectangular array. The existence of a guided wave was analyzed by confirming that the eigen mode and scan blindness curves are identical. Moreover, this mode could be predicted using a

proposed simple equivalent circuit and a dispersion relation formula. Through this equation, it was verified that this guiding wave can be described as a quasi-TEM mode. It was also found that adding slits and stubs in the unit cell plays an important role in lowering the resonant frequencies in the printed dipole structure. Therefore, it could be considered an efficient method for eliminating the scan blindness at the desired frequencies.

The difference between the scan blindness of the 1-D and 2-D arrays was clarified using the comparison of the Q value in the unit cell in the 1-D and 2-D arrays. The scan blindness in the 2D array occurred in the E-plane direction at around $\pm 36^\circ$; however, it was barely observed in the 1-D array. The Q value of the unit cell for the 1-D array is formed between 1 and 10, whereas the value for the 2-D array is over 1,000. This means that the 1-D array has more external losses than when the resonance mode energy is 2-D array.

The analysis was verified by simulations and experiments conducted on four types of models, AEP and array prototype with and w/o parasitic structures. The proposed concept provides improvements in the gain and scan range. The analysis of the scan blindness and its elimination method can be applied to various types of half wave dipole antennas with balun in a rectangular array. The analysis of the scan blindness will be extended to other lattice configurations of dipole antennas in future work.

2.12. References

[1] D. Sievenpiper, L. Zhang, R. F. J. Broas, N. G. Alexopolous, and E. Yablonovitch, “High-impedance electromagnetic surfaces with a forbidden frequency band,” *IEEE Trans. Microwave Theory Tech.*, vol. 47, pp. 2059–2074, Nov. 1999.

[2] F. Elek and G. V. Eleftheriades, “Dispersion analysis of Sievenpiper’s shielded structure using multi-conductor transmission-line theory,” *IEEE Microwave Wireless Components Lett.*, vol. 14, no. 9, pp. 434–436, Sep. 2004.

[3] A. K. Bhattacharyya, *Phased Array Antennas: Floquet Analysis, Synthesis, BFNs and Active Array Systems*. Hoboken, NJ, USA: Wiley, 2006.

[4] D. M. Pozar, “The active element pattern,” *IEEE Trans. Antennas Propag.*, vol. 42, no. 8, pp. 1176–1178, Sep. 1994.

[5] D. M. Pozar, *Microwave Engineering*, 4th ed. New York, NY, USA: Wiley, 2011, pp. 288–293.

[6] G. V. Eleftheriades, A. K. Iyer, and P. C. Kremer, “Planar negative refractive index media using periodically L-C loaded transmission lines,” *IEEE Trans. Microw. Theory Tech.*, vol. 50, no. 12, pp. 2702 – 2712, Dec. 2002.

[7] Raza S, “Characterization of the Reflection and Dispersion Properties of Mushroom-Related Structures and Their Application to

Antennas,” Thesis on Master of Applied Science, Dept. Elect. Comput. Eng., Univ. Toronto, Toronto, Canada, 2012.

[8] S. X. Ta, H. Choo, and I. Park, “Broadband printed–dipole antenna and its arrays for 5G applications,” *IEEE Antennas Wireless Propag. Lett.*, vol. 16, pp. 2183–2186, 2017.

[9] S. X. Ta and I. Park, “Broadband printed–dipole antennas for millimeter wave applications,” in *Proc. Int. Symp. IEEE Radio Wireless*, Phoenix, AZ, USA, Jan. 2017, pp. 65–67.

[10] S. Lim, W. Choi, and Y. Yoon, “Miniaturized radio frequency choke using modified stubs for high isolation in MIMO systems,” *J. Electromagn. Eng. Sci.*, vol. 15, no. 4, pp. 219–223, Oct. 2015.

[11] A. K. Bhattacharyya, “Active element pattern symmetry for asymmetrical element arrays,” *IEEE Antennas Wireless Propag. Lett.*, vol. 6, pp. 275–278, June 2007.

[12] E. Holzman, “On the use of dummy elements to match edge elements in transmit arrays,” in *Proc. IEEE Int. Symp. Phased Array Syst. Technol.*, Oct. 2013, pp. 549–552.

Chapter 3. Analysis of an HED on a Truncated Dielectric Slab over the Ground Plane

3.1. Motivation

In this chapter, it is introduced a bow-tie array with broadband characteristics in the H-plane. In that case, the antenna is physically separated, various guided modes can be avoided and a wide beam pattern can be obtained over a broadband. In addition, we will discuss a method to reduce the coupling by using a substrate with a high dielectric constant and the diffraction effect.

In this Chapter, we obtain the physical intuition for for high dielectric printed antennas by using the physical-optics (PO) approximation. By applying the equivalence theorem, the dielectric slab is replaced by polarization currents. Then, current can be derived by using multilayered structure theory [1]. And then, the far-field can be expressed as a Sommerfeld type representation. The saddle-point method for the asymptotic evaluation of an integral is introduced to implement the integration of the far-field equation. Through PO methods, the far-field results can be described in terms of a geometrical optics(GO) contribution and ray-diffracted contributions from space waves, surface waves, and leaky waves [2],[3]. Furthermore, by using these various rays as multipath

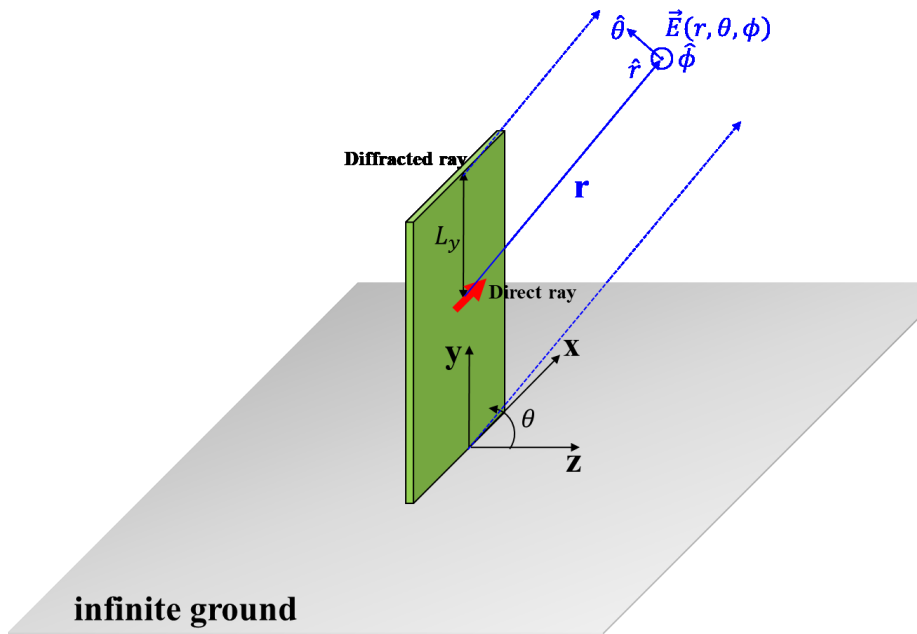


Fig. 3.1. Geometry of an HED on a truncated dielectric slab over the ground plane.

cancellation, mutual coupling of the array antennas can be reduced.

3.2. Basic Formulation for PO

This procedure leads to the far field expression

$$\mathbf{E}(\mathbf{r}, \boldsymbol{\theta}, \boldsymbol{\phi}) = -jk_0\eta \frac{e^{-jk_0r}}{4\pi r} (F_\theta \hat{\boldsymbol{\theta}} + F_\phi \hat{\boldsymbol{\phi}}) \quad (3.1)$$

Where is $F_\xi(\boldsymbol{\theta}, \boldsymbol{\phi})$ is the electric far-field pattern given by

$$F_\xi(\boldsymbol{\theta}, \boldsymbol{\phi}) = (\hat{\mathbf{x}} \cdot \hat{\boldsymbol{\xi}}) + F_\xi^{PO}(\boldsymbol{\theta}, \boldsymbol{\phi}), \quad \xi = \theta, \phi \quad (3.2)$$

and

$$F_\xi^{PO}(\boldsymbol{\theta}, \boldsymbol{\phi}) = \int_{-\infty}^{\infty} \int_{-\infty}^{L_y} \int_{-d}^0 \mathbf{J}^{PO}(\mathbf{x}, \mathbf{y}, \mathbf{z}) \cdot \hat{\boldsymbol{\xi}} e^{j(k_{x0}x + k_{y0}y + k_{z0}z)} dx dy dz \quad (3.3)$$

And h is the thickness of the substrate. It is worth noting that the term in (3.2) represents the direct contribution from the unit dipole.

3.3. Polarization Current in Multilayered Structures

PO current $\mathbf{J}^{PO}(\mathbf{x}, \mathbf{y}, \mathbf{z})$ can be described as displacement current in the dielectric slab. By invoking the equivalence principle, the polarization currents are related to the electric (E) and magnetic (H) fields within the infinite dielectric slab as shown in Fig. 3.2. Fig

3.2. illustrates a dielectric slab, of thickness d and with a dielectric constant. An Herzian electric dipole source is located at $\mathbf{x} = \mathbf{0}$, $\mathbf{y} = \mathbf{0}$, $\mathbf{z} = \mathbf{0}$ and is parallel to the \mathbf{yz} plane. This current source may be represented as follows:

$$\mathbf{J}_{se} = \hat{x}\delta(x)\delta(y) \quad (3.4)$$

and its equation is given as $\mathbf{J}_d(\mathbf{x}, \mathbf{y}, \mathbf{z})$ in the dielectric slab.

$$\mathbf{J}_d(\mathbf{x}, \mathbf{y}, \mathbf{z}) = j\omega\varepsilon_0(\varepsilon_r - 1)\mathbf{E}(\mathbf{x}, \mathbf{y}, \mathbf{z}) \quad (3.5)$$

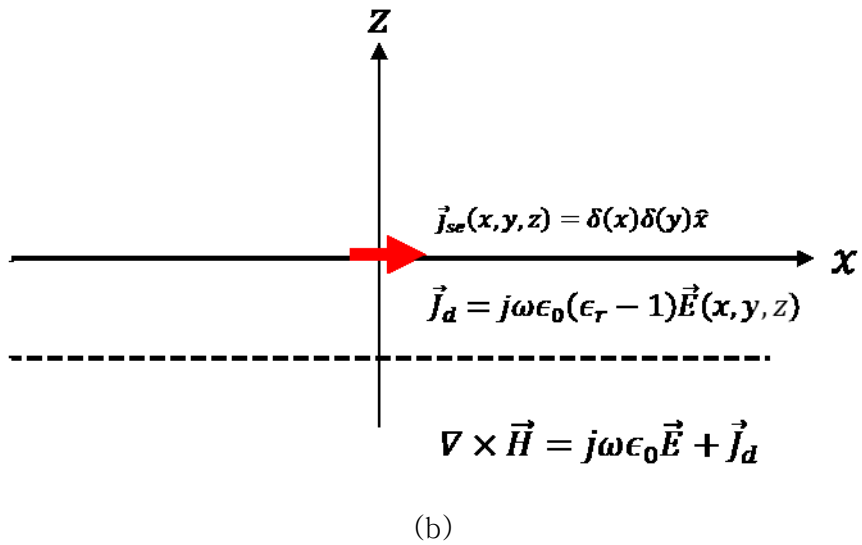
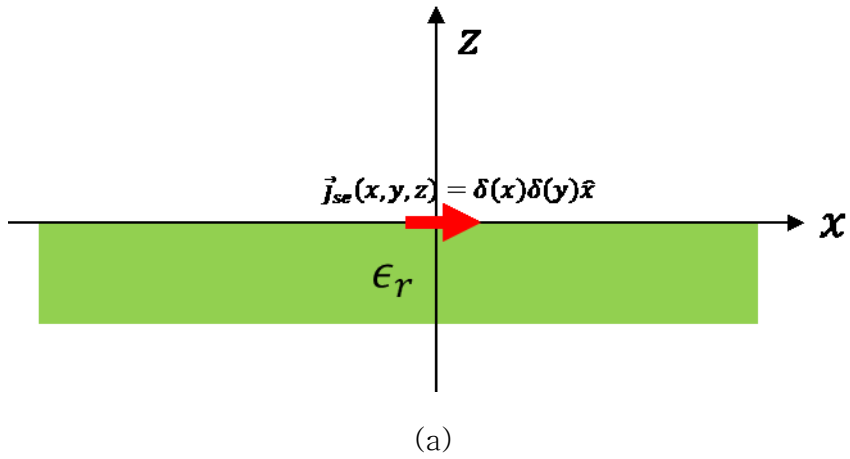
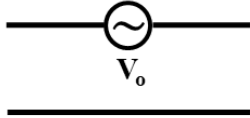
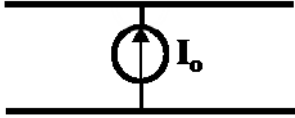


Fig. 3.2. Equivalence theorem: (a) current on dielectric slab, and (b) Equivalent current source.

TABLE 3.1
SPECTRAL EQUIVALENT CIRCUIT FOR ELECTRIC CURRENT

Expression	TM_z	TE_z
Equivalent Voltage	\tilde{B}_z	\tilde{D}_z
Characteristic Admittance	$y_i^m = \frac{jk_{zi}k_0}{\epsilon_i}$	$y_i^e = \frac{jk_{zi}k_0}{\mu_i}$
TL Equivalent Source	$V_0 = \frac{\mathbf{k}_\rho \cdot \tilde{\mathbf{J}}_{se}}{\omega}$	$I_0 = -j\hat{z} \cdot (\mathbf{k}_\rho \times \tilde{\mathbf{J}}_{se})$
Characteristic Admittance		

Note: $\mathbf{k}_\rho = \hat{x}k_x + \hat{y}k_y$

This section presents EM field using spectral domain analysis. The source will excite the TE_z and TM_z modes. It is important to know the longitudinal components of the electric and magnetic displacement vectors, D_z and B_z . To determine D_z and B_z we express the field quantities in terms of their two dimensional Fourier spectra. In the spectral domain, the quantities D_z and B_z follow transmission line equations. The transmission line parameters are functions of the electrical parameters of a medium. The conventional transmission line theory is then used to obtain the Fourier spectra for D_z and B_z . The complete field solution is the superposition of the TE_z and TM_z fields. The spectral domain equivalent circuits and

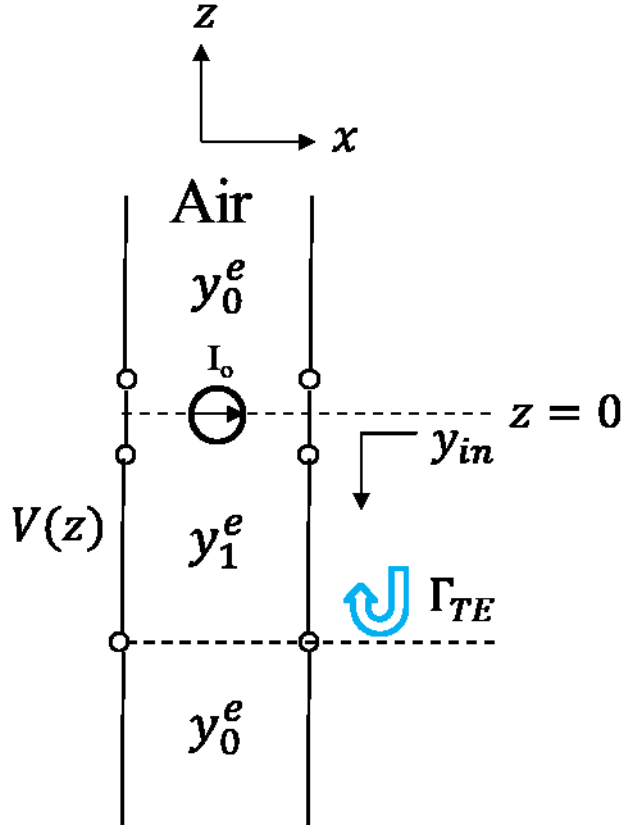


Fig. 3.3. Spectral equivalent circuit for the TE_z mode.

related parameters for the TE_z and TM_z modes are given in Table 3.1.

3.3.1 TE_z Mode Solution in Spectral Domain

Fig. 3.3 shows the structure of a layered medium for TE_z mode. Two-dimensional Fourier transform of the surface current \mathbf{J}_{se} is

$$\tilde{\mathbf{J}}_{se} = \frac{1}{4\pi^2} \int_{-\infty}^{\infty} \int_{-\infty}^{\infty} \mathbf{J}_{se} e^{j(k_x k_0 x + k_y k_0 y)} dx dy = \hat{x} \frac{1}{4\pi^2} \quad (3.6)$$

For the TE_z modal solution we need to solve for B_z . The Spectral TL equivalent circuit for \tilde{B}_z as the TL voltage is show below. The voltage at $z = 0$ is

$$V_0 = \frac{I_0}{y_{tot}^e} \quad (3.7)$$

Where $y_{tot}^e = y_{in}^e + y_0^e$, y_{in}^e and y_0^e are the input admittances seen at the two sides of the soure. Using table 3.1 and the equivalent transmission line shown in Fig 3.3, input impedance y_{in}^e and y_0^e are given as

$$y_0^e = \frac{jk_z k_0}{\mu} \quad (3.8)$$

$$y_{in} = y_1^e \frac{e^{jk_{z1}d} - \Gamma_{TE} \cdot e^{-jk_{z1}d}}{e^{jk_{z1}d} + \Gamma_{TE} \cdot e^{-jk_{z1}d}} = y_1^e \frac{y_0^e + jy_1^e \tan(k_{z1}k_0d)}{y_1^e + jy_0^e \tan(k_{z1}k_0d)} \quad (3.9)$$

$$\Gamma_{TE} = \frac{y_1^e - y_0^e}{y_1^e + y_0^e} \quad (3.10)$$

The transmission line current I_0 is given by

$$I_0 = -j \left(\vec{k}_\rho \times \tilde{J}_{se} \right) \cdot \hat{z} = j \frac{k_y}{4\pi^2 \omega} \quad (3.11)$$

Therefore the voltage distribution $V(z)$ in the region $-d < z < 0$,

is given by

$$V(z) = V_0 \frac{e^{jk_{z1}k_0(z+d)} + \Gamma_{TE} e^{-jk_{z1}k_0(d+z)}}{e^{jk_{z1}k_0d} + \Gamma_{TE} e^{-jk_{z1}k_0d}} \quad (3.12)$$

\tilde{B}_z is considered as the transmission line voltage V

$$V(z) = \tilde{B}_z(z) \quad (3.13)$$

Thus, for $-d < z < 0$, equation (3.12) can be expressed as

$$\tilde{B}_z(z) = -j \frac{k_y \mu}{4} \cdot \frac{(k_{z1} + k_z) e^{jk_{z1}k_0(z+d)} + (k_{z1} - k_z) e^{-jk_{z1}k_0(z+d)}}{TE_e \cdot TE_o} \quad (3.14)$$

The complete field solution can be obtained from the magnetic vector potential F_z , that can be expressed in terms of B_z . In the Fourier domain the

$$\tilde{F}_z(z) = \frac{j\omega\varepsilon}{k_\rho^2} \tilde{B}_z(z) \quad (3.15)$$

The EM field components are obtained using

$$\mathbf{D} = -\nabla \times (\hat{z} \tilde{F}_z) \quad (3.16)$$

The component \tilde{D}_x , \tilde{D}_y , \tilde{D}_z are

$$\tilde{D}_x = jk_y \tilde{F}_z = -\frac{k_y \omega \varepsilon}{k_\rho^2} \tilde{B}_z \quad (3.17)$$

$$\tilde{D}_y = jk_x \tilde{F}_z = \frac{k_x \omega \varepsilon}{k_\rho^2} \tilde{B}_z \quad (3.18)$$

$$\tilde{D}_z = 0 \quad (3.19)$$

Substituting equation (3.17)~(19) into equation (3.4), the spectral components for TE are given as

$$\begin{aligned} \tilde{J}_{x_{TE}}^{\tilde{a}}(k_x, k_y, z) &= -j \frac{k_y \omega^2 \varepsilon}{k_\rho^2} (\varepsilon_r - 1) \cdot \tilde{B}_z \\ &= -j \frac{k_y^2}{k_\rho^2} \cdot \frac{(\varepsilon_r - 1)}{4} \cdot \frac{(k_{z1} + k_z) \cdot e^{jk_{z1}k_0(z+d)} + (k_{z1} - k_z) \cdot e^{-jk_{z1}k_0(d+z)}}{TE_e \cdot TE_o} \end{aligned} \quad (3.20)$$

$$\begin{aligned} \tilde{J}_{y_{TE}}^{\tilde{a}}(k_x, k_y, z) &= -j \frac{k_y \omega^2 \varepsilon}{k_\rho^2} (\varepsilon_r - 1) \cdot \tilde{B}_z \\ &= j \frac{k_x k_y}{k_\rho^2} \cdot \frac{(\varepsilon_r - 1)}{4} \cdot \frac{(k_{z1} + k_z) \cdot e^{jk_{z1}k_0(z+d)} + (k_{z1} - k_z) \cdot e^{-jk_{z1}k_0(d+z)}}{TE_e \cdot TE_o} \end{aligned} \quad (3.21)$$

$$\tilde{J}_{z_{TE}}^{\tilde{a}}(k_x, k_y, z) = 0 \quad (3.22)$$

3.3.2 TM_z Mode Solution in Spectral Domain

From the Table 3.1, the electric surface current corresponds to a series voltage V_0 in the TL equivalent circuit as shown in Fig 3.4.

$$V_0 = \frac{\vec{k}_\rho \cdot \tilde{J}_{se}}{\omega} = \frac{k_x}{4\pi^2\omega} \quad (3.22)$$

The voltage inside a dielectric slab can be expressed as

$$V_0^- = -\frac{y_0^m}{y_{tot}^m} V_0 \quad (3.23)$$

Where $y_{tot}^m = y_{in}^m + y_0^m$, y_{in}^m and y_0^m are the input admittances seen at the two sides of the source. Using Table 3.1 and the equivalent transmission line shown in Fig. 3.3, input impedance y_{in}^m and y_0^m are given as

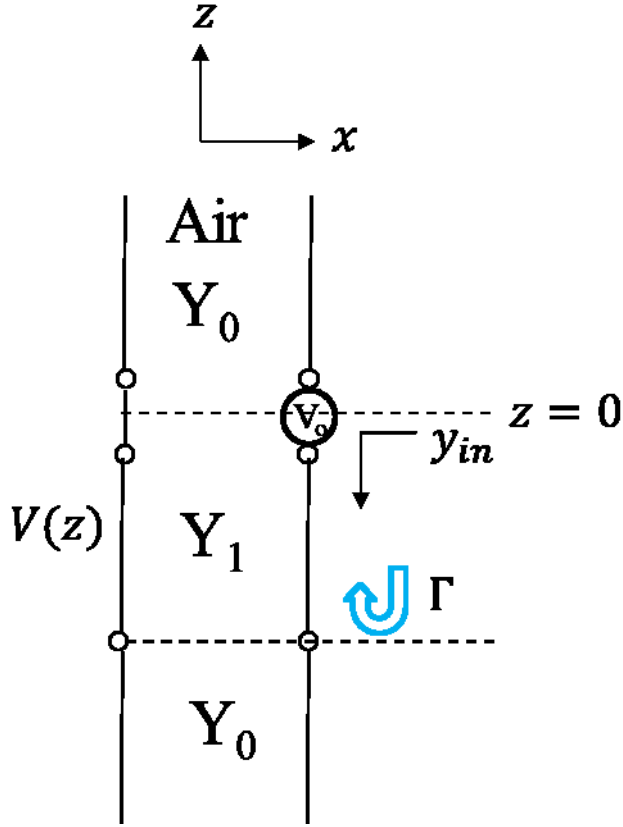


Fig. 3.4. Spectral equivalent circuit for the TMz mode.

$$y_0^m = \frac{jk_z k_0}{\epsilon_0} \quad (3.24)$$

$$y_{in}^m = y_1^m \frac{e^{jk_{z1}d} - \Gamma_{TM} e^{-jk_{z1}d}}{e^{jk_{z1}d} + \Gamma_{TM} e^{-jk_{z1}d}} \quad (3.25)$$

The total admittance y_{tot}^m is given by

$$y_{tot}^m = \frac{e^{jk_{z1}k_0 d} (y_0^m + y_1^m) - e^{-jk_{z1}k_0 d} \Gamma_{TM} (y_0^m - y_1^m)}{e^{jk_{z1}k_0 d} + \Gamma_{TM} e^{-jk_{z1}k_0 d}} \quad (3.26)$$

$$\Gamma_{TM} = \frac{y_1^m - y_0^m}{y_1^m + y_0^m} \quad (3.27)$$

$$y_1^m = \frac{jk_{z1}k_0}{\epsilon_r \epsilon_0} \quad (3.28)$$

The voltage V_0^- (3.23) becomes

$$V_0^- = \frac{k_x}{\omega} \frac{(e^{jk_{z1}k_0d} + \Gamma_{TM}e^{-jk_{z1}k_0d})y_0^m}{e^{jk_{z1}k_0d}(y_1^m + y_0^m) - \Gamma_{TM}e^{-jk_{z1}k_0d}(y_1^m - y_0^m)} \quad (3.29)$$

The voltage distribution in the region $-d < z < 0$, is given by

$$\begin{aligned} V(z) &= V_0^- \frac{e^{jk_{z1}k_0(z+d)} + \Gamma_{TM}e^{-jk_{z1}k_0(d+z)}}{e^{jk_{z1}k_0d} + \Gamma_{TM}e^{-jk_{z1}k_0d}} \\ &= -\frac{k_x k_z \epsilon_r}{4\omega} \cdot \frac{e^{jk_{z1}k_0(z+d)}(k_{z1} + \epsilon_r k_z) + \Gamma_{TM}e^{-jk_{z1}k_0(d+z)}(k_{z1} - \epsilon_r k_z)}{TM_e \cdot TM_o} \end{aligned} \quad (3.30)$$

\tilde{D}_z is considered as the transmission line voltage V

$$V(z) = \tilde{D}_z(z) \quad (3.31)$$

The field components, in terms of \tilde{A}_z , are expressed in (3.32).

$$\tilde{A}_z(z) = \frac{j\omega\mu}{k_\rho^2} \tilde{D}_z(z) \quad (3.32)$$

The EM field components are obtained using

$$\mathbf{B} = \nabla \times (\hat{z}\tilde{A}_z) \quad (3.33)$$

$$j\omega\epsilon\mathbf{E} = \nabla \times \mathbf{H} \quad (3.34)$$

Using the source-free Maxwell's equations (3.32~33), The component \tilde{D}_x , \tilde{D}_y , \tilde{D}_z in dielectric slab can be derived as

$$\tilde{D}_x = \frac{jk_x k_{z1}}{\omega\mu} \tilde{A}_z = \frac{k_x k_{z1}}{k_\rho^2} \tilde{D}_z \quad (3.35)$$

$$\tilde{D}_y = \frac{jk_y k_{z1}}{\omega\mu} \tilde{A}_z = \frac{k_y k_{z1}}{k_\rho^2} \tilde{D}_z \quad (3.36)$$

Substituting equation (3.17)~(19) into equation (3.4), the spectral components for TM are given as

$$\tilde{J}_{xTM}^d = -j \frac{k_x^2 \cdot k_z k_{z1}}{k_\rho^2} \cdot \frac{(\epsilon_r - 1)}{4} \cdot \frac{(k_{z1} + \epsilon_r k_z) \cdot e^{jk_{z1}k_0(z+d)} - (k_{z1} - \epsilon_r k_z) \cdot e^{-jk_{z1}k_0(d+z)}}{TM_e \cdot TM_o} \quad (3.37)$$

TABLE 3.2
DISPERSION EQUATION

Expression	Expression
TE_{even}	$k_{z1} \cdot \cos\left(k_{z1}k_0 \frac{d}{2}\right) + jk_z \cdot \sin\left(k_{z1}k_0 \frac{d}{2}\right)$
TE_{odd}	$k_z \cdot \cos\left(k_{z1}k_0 \frac{d}{2}\right) + jk_{z1} \cdot \sin\left(k_{z1}k_0 \frac{d}{2}\right)$
TM_{even}	$k_{z1} \cdot \cos\left(k_{z1}k_0 \frac{d}{2}\right) + j\varepsilon_r \cdot k_z \cdot \sin\left(k_{z1}k_0 \frac{d}{2}\right)$
TM_{odd}	$\varepsilon_r \cdot k_z \cdot \cos\left(k_{z1}k_0 \frac{d}{2}\right) + jk_{z1} \cdot \sin\left(k_{z1}k_0 \frac{d}{2}\right)$

$$\tilde{J}_{y_{TM}}^{\tilde{a}} = -j \frac{k_x k_y \cdot k_z k_{z1} \cdot (\varepsilon_r - 1)}{k_\rho^2 \cdot 4} \cdot \frac{(k_{z1} + \varepsilon_r k_z) \cdot e^{jk_{z1}k_0(z+d)} - (k_{z1} - \varepsilon_r k_z) \cdot e^{-jk_{z1}k_0(d+z)}}{TM_e \cdot TM_o} \quad (3.38)$$

$$\tilde{J}_{z_{TM}}^{\tilde{a}} = -j \cdot \frac{(\varepsilon_r - 1)}{4} \cdot k_x k_z \cdot \frac{(k_{z1} + \varepsilon_r k_z) \cdot e^{jk_{z1}k_0(z+d)} - (k_{z1} - \varepsilon_r k_z) \cdot e^{-jk_{z1}k_0(d+z)}}{TM_e \cdot TM_o} \quad (3.39)$$

Note that the denominators of (3.20) ~ (3.21), (3.37) ~ (3.39) indicate the dispersion equations of the dielectric slab waveguide, which is summarized in Table 3.2. In addition, its solutions will be considered in the subsection 3.4.

3.3.3 Complete Polarization Current Solution

The PO current components can be expressed by their spectral Fourier representation

$$J^{PO}(\mathbf{x}, \mathbf{y}, \mathbf{z}) = \frac{k_0^2}{4\pi^2} \int_{-\infty}^{\infty} \int_{-\infty}^{\infty} \tilde{J}^{PO} e^{-jk_0(k_x x + k_y y)} dk_x dk_y \quad (3.40)$$

PO spectral current can be decomposed into the components which are derived from chapter 3.3.1~3.3.2. The double spectral Fourier representation (3.3) is now introduced in (3.40), thus obtaining

$$F_{\xi}^{PO} = \frac{k_0^2}{(2\pi)^2} \int_{-\infty}^{\infty} \int_{-\infty}^{L_y} \int_{-\infty}^{\infty} \int_{-\infty}^{\infty} \int_{-d}^0 \tilde{J}^{PO} \cdot \hat{\xi} e^{-jxk_0(k_x - u) - jyk_0(k_y - v) + jzw} dz dk_x dk_y dy dx \quad (3.41)$$

in which

$$\begin{aligned} u &= \sin \theta \cos \phi \\ v &= \sin \theta \sin \phi \\ w &= \cos \theta \end{aligned} \quad (3.42)$$

and

$$B_{\xi}(k_x, k_y) = \int_{-d}^0 \tilde{J}^{PO} \cdot e^{-jk_0 z w} dz \quad (3.43)$$

The explicit expression of $B_\xi(k_x, k_y)$ is given in Appendix 2. Substituting (3.43) into equation (3.40),

$$F_\xi^{PO} = \frac{k_0^2}{(2\pi)^2} \int_{-\infty}^{\infty} \int_{-\infty}^{L_y} \int_{-\infty}^{\infty} \int_{-\infty}^{\infty} \widetilde{B}_\xi(k_x, k_y) \cdot e^{-jxk_0(k_x-u) - jyk_0(k_y-v)} dk_x dk_y dy dx \quad (3.44)$$

The integration in the x variable is easily recognized as a Dirac function, i.e.,

$$\int_{-\infty}^{\infty} e^{-jxk_0(k_x-u)} dk_x = \frac{2\pi}{k_0} \delta(u - k_x) \quad (3.45)$$

Thus allowing to evaluate the k_x integration in a closed form,

$$F_\xi^{PO} = \frac{k_0}{2\pi} \int_{-\infty}^{\infty} \int_{-\infty}^{L_y} \widetilde{B}_\xi(u, k_y) \cdot e^{-jyk_0(k_y-v)} dy dk_y \quad (3.46)$$

By assuming small losses in the surrounding medium, the y integration reduces to the end point at, i.e.,

$$F_\xi^{PO} = -\frac{e^{j\Omega v}}{2\pi j} \int_{-\infty}^{\infty} G_\xi(u, k_y) \cdot e^{-j\Omega k_y} dk_y \quad (3.47)$$

where

$$G_{\xi}(u, k_y) = \frac{B_{\xi}(u, k_y)}{(k_y - v)} \quad (3.48)$$

$$\Omega = k_{y0}L_y \quad (3.49)$$

The integrand in (3.47) exhibits a pole at $k_y = v$; due to the small losses that we have assumed, a clockwise indentation of the integration path around this pole is required. The integral in 3.47 is a Sommerfeld type representation in the k_y complex plane, which will be described in the subsection 3.6.

3.4. Dispersion Equation Solutions

In this section, the problem of an electric dipole source above a dielectric waveguide will be studied, in order to obtain the dispersion equation solutions. A discussion of the surface wave modes and complex modes are included. Various authors have examined similar problems.

3.4.1. Surface Wave Solutions

The problem of exciting surface waves has received considerable attention. Here, we set

$$D = k_{z1}k_0 = \frac{d}{2} \quad (3.50)$$

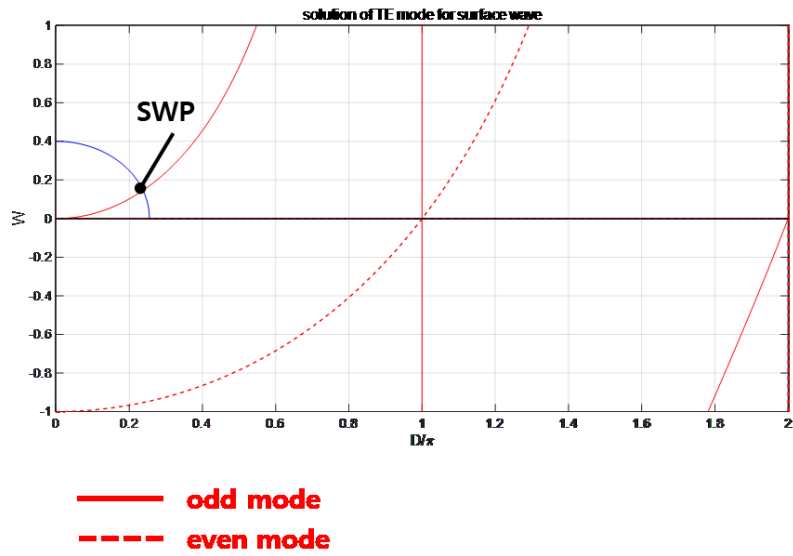
and

$$W = jk_z k_0 \frac{d}{2} \quad (3.51)$$

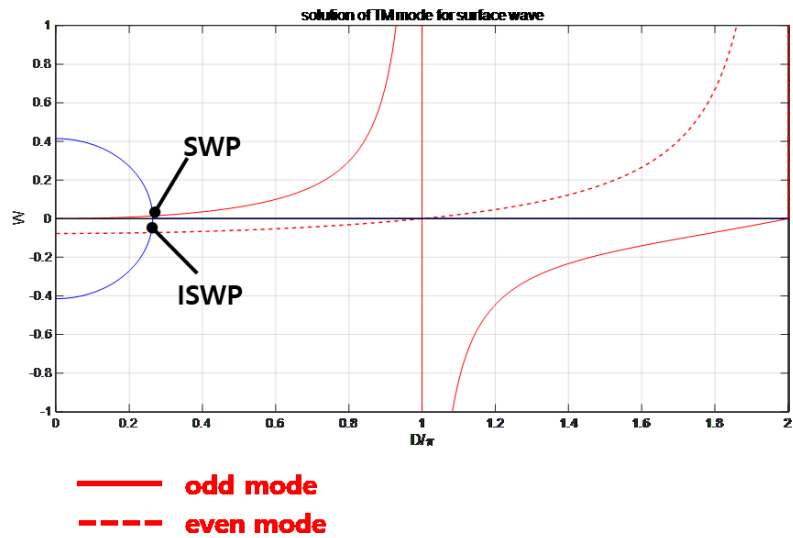
Using equation (3.50)~(3.51)

$$W^2 + Z^2 = (\epsilon_r - 1)k_0 \left(\frac{d}{2}\right)^2 = a^2 \quad (3.52)$$

Fig.3.5 shows the surface wave pole solutions. Blue circle means the curve of equation (3.52). And the red line and dashed line are derived from Table 3.3. When the solution of TM mode is $W > 0$, the surface wave pole exists, whereas when $W < 0$, iswp exists, which is called improper surface-wave poles (ISWP's) [4].



(a)



(b)

Fig. 3.5. Surface wave pole solutions: (a) TE mode, and (b) TM mode.

TABLE 3.3
DISPERSION EQUATION FOR COMPLEX WAVE

TE_{even}
$-W = Z \cdot \cot Z$ $TE_{even} = a \sin Z \pm Z$ $= a \sin(x + jy) - (-1)^n \cdot (x + jy)$ $n\pi < x < n\pi + \frac{1}{2}\pi$ $n = 1, 2, 3, \dots$
TE_{odd}
$W = Z \cdot \cot Z$ $TE_{odd} = a \cos Z \pm Z$ $= a \cos(x + jy) + (-1)^n \cdot (x + jy)$ $n\pi + \frac{1}{2}\pi < x < (n + 1)\pi$ $n = 0, 1, 2, 3, \dots$
TM_{even}
$-\varepsilon_r W = Z \cdot \cot Z$ $TM_{even} = \sin Z \sqrt{\varepsilon_r^2 (a^2 - Z^2) + Z^2} \pm Z$ $= \sin Z \sqrt{\varepsilon_r^2 (a^2 - (x + jy)^2) + (x + jy)^2} - (-1)^n \cdot (x + jy)$ $n\pi < x < n\pi + \frac{1}{2}\pi$ $n = 1, 2, 3, \dots$
TM_{odd}
$\varepsilon_r W = Z \cdot \tan Z$ $TM_{odd} = \cos Z \sqrt{\varepsilon_r^2 (a^2 - Z^2) + Z^2} \pm Z$ $= \cos Z \sqrt{\varepsilon_r^2 (a^2 - (x + jy)^2) + (x + jy)^2} + (-1)^n \cdot (x + jy)$ $n\pi + \frac{1}{2}\pi < x < (n + 1)\pi$ $n = 0, 1, 2, 3, \dots$

3.4.2. Complex Guided Wave Solutions

To determine the complex poles, let Z be the complex variables x , y , Z used here should not be confused with the rectangular coordinates.

$$Z = k_z k_0 \frac{d}{2} = x + jy \quad (3.51)$$

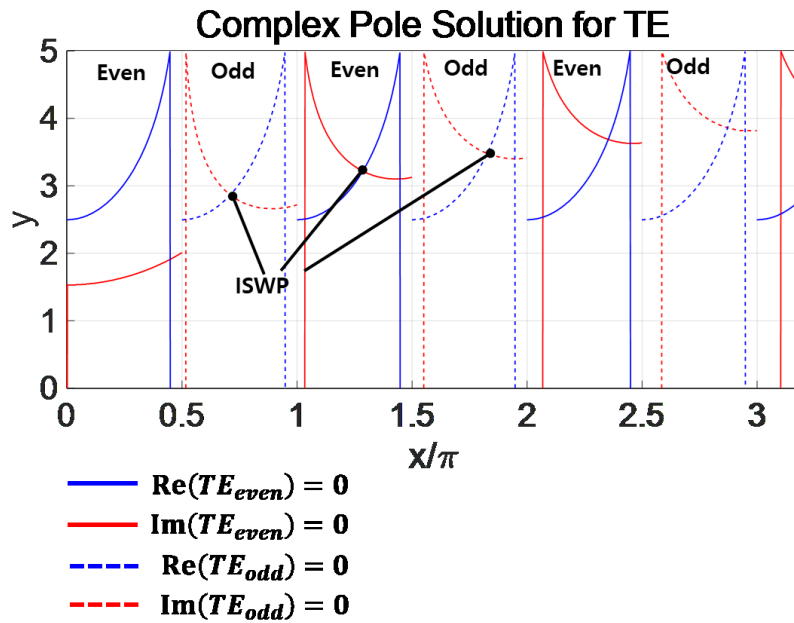
$$W = jk_z k_0 \frac{d}{2} \quad (3.52)$$

Substituting (3.51)~(3.52) into dispersion equation from table 3.2, equations are given as table 3.3. From table 3.3, four types of dispersion equations TE_{even} , TE_{odd} , TM_{even} , TM_{odd} can be obtained. We can find the solution of the real part and imaginary part of each equation. Then, a simultaneous solution of these two equations determines the complex roots for Z . For example, a solution that satisfies equations 3.53 and 3.54 simultaneously for TE_{even} mode is a complex pole [5].

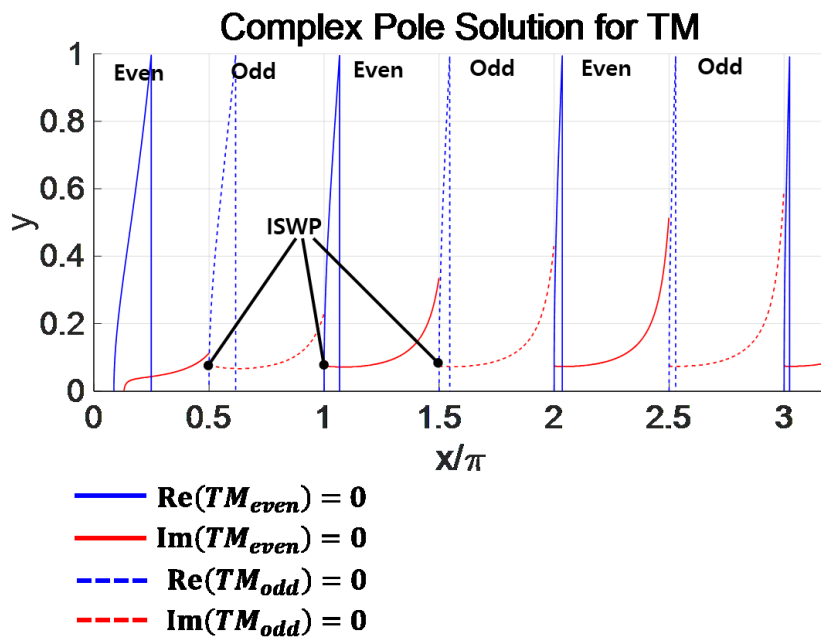
$$\text{Re}(TE_{even}) = 0 \quad (3.53)$$

$$\text{Im}(TE_{even}) = 0 \quad (3.54)$$

By plotting the two equations and on the xy plane, the roots are readily determined. Fig. 3.6 shows the graphical solution for complex pole solutions for four types of dispersion equations at $\epsilon_r = 12.2$ and $d = 0.035 \lambda_0$, and $\theta = \phi = 45^\circ$. Using equation 3.x, $a = 0.381$. The first root for TM is $x = 1.572$, $y = 0.081$, giving $k_y = 0.7 - j12.67$. And the first root for TE is $x = 2.225$, $y = 2.91$, giving $k_y = 24.47 - j18.47$.



(a)



(b)

Fig. 3.6. Graphical solution for complex pole solutions. Solid lines are for real part solution; broken lines are imaginary part solution: (a) TE mode, and (b) TM mode.

3.5. The Saddle-Point Method of Integration

The saddle-point method (also known as the method of steepest descent) for the asymptotic evaluation of an integral was introduced by Debye for obtaining asymptotic expansions of the Hankel functions [5].

As is usual in Sommerfeld-type integrals, the numerical evaluation of (3.47) presents two major difficulties. First, the poles have to be extracted to obtain a smooth function suitable for numerical integration. Next, the behavior of $B_\xi(k_x, k_y)$ for k_y , large is such that the integrand is a rapidly oscillating and slowly decaying function, thus leading to a poor convergent integral for large values

of Ω [2]. To overcome these limitations, asymptotic closed-form expressions of F_ξ^{PO} will be derived by introducing the change of variable as follow.

$$k_y = \alpha - js^2 \quad (3.55)$$

Equation (3.47) transforms into

$$F_\xi^{PO}(\theta, \phi) = -\frac{e^{j\Omega(\alpha-v)}}{2\pi j} \int_C G_\xi(s) e^{-j\Omega s^2} ds \quad (3.56)$$

Where

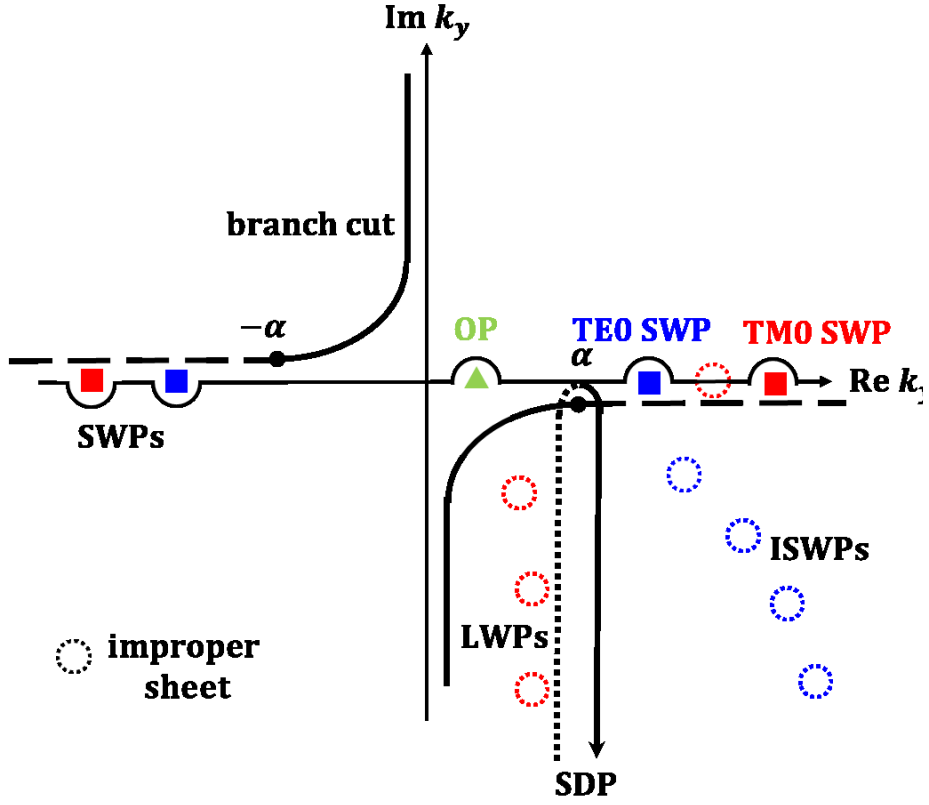


Fig. 3.7. Topology of the proper Riemann sheet of the complex k_y plane.

$$G_{\xi}(s) = \frac{2sB_{\xi}(u, k_y)}{s^2 - s_0^2} \quad (3.57)$$

$$s_0 = -e^{-j(\pi/4)} \sqrt{\alpha - v} \quad (3.58)$$

And the contour of integration $C \equiv (\infty e^{j3\pi/4}, \infty e^{j\pi/4})$ is depicted

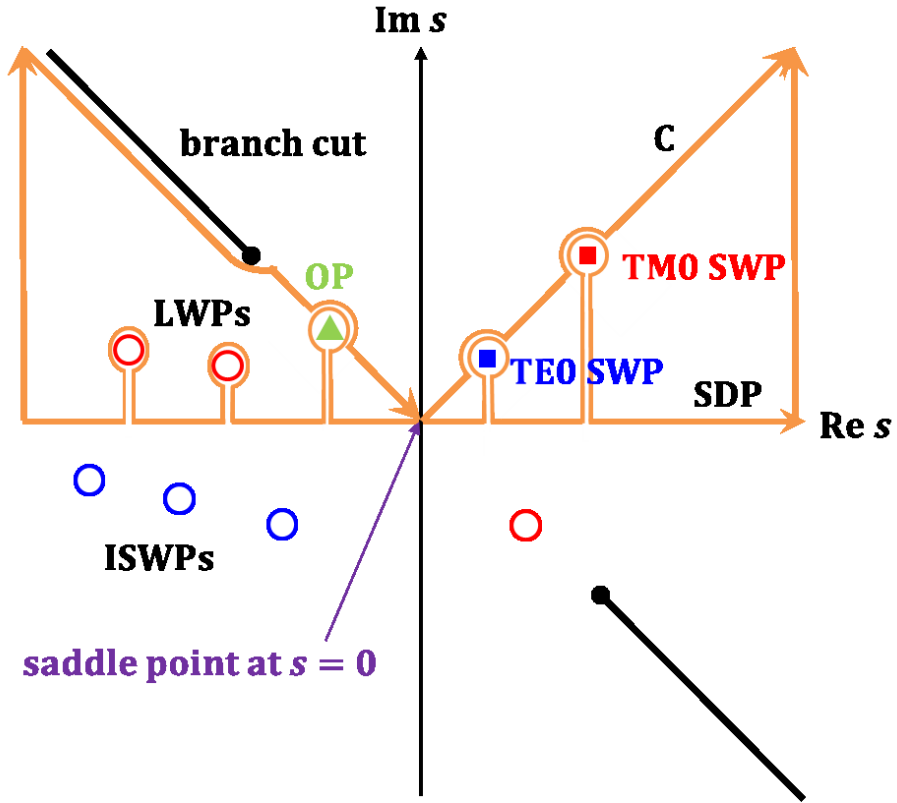


Fig. 3.8. Topology of the top Rieman sheet of the complex s plane.

in Fig.3.8. From the equation (3.55), k_z can be given as

$$k_z = -s\sqrt{s^2 - j2\alpha} \quad (3.59)$$

Using equation (3.55), two branch points $s = \pm\sqrt{2\alpha} \cdot e^{-j(\pi/4)}$ at are depicted in the s plane. The SWP's, the ISWP's and the LWP's are mapped by the transformation (3.55) on the proper sheet, as depicted in Fig 3.8. Their expressions are

$$s_i^{pw} = e^{j(\pi/4)} \sqrt{k_{yi}^{pw} - \alpha} \quad (3.60)$$

Where the subscript pw denotes sw, isw, or lw. As depicted in Fig. 3.8. the SWP's, the LWP's are located in the first and second quadrants of the proper s plane, respectively, while the ISWP's are located in the third and fourth quadrants. In the complex s plane, the steepest descent path (SDP) now goes through the saddle point $s = 0$. Then the original contour C is deformed as shown in Fig. 3.8. This SDP runs on the real axis of the s plane. Therefore we have

$$\int_C = \int_{SDP} - j2\pi \cdot \sum \text{residues} \quad (3.61)$$

The residue term in (3.61) is given by

$$-j2\pi \cdot \sum \text{residues} = -2\pi j \sum \frac{Num(k_{yi}^w)}{Den'(k_{yi}^w)} \cdot e^{-j\Omega(k_y - v)} \quad (3.62)$$

Where

$$G(k_{yi}^w) = \frac{Num(k_{yi}^w)}{Den'(k_{yi}^w)} \quad (3.63)$$

Using Equation A.1 in Appendix, Equation (3.62) can be expressed as

$$\begin{aligned}
\sum_i D_{\xi i}^w(k_{yi}^w) &= -2\pi \sum_i \frac{Num(k_{yi}^w)}{Den'(k_{yi}^w)} \\
&= -2\pi \sum_i \left[\left(\frac{b_{\xi}^{TE}(u, k_{yi}^w)}{TE'(k_{yi}^w) \cdot (k_{yi}^w - v) + TE(k_{yi}^w)} \right) + \left(\frac{b_{\xi}^{TM}(u, k_{yi}^w)}{TM'(k_{yi}^w) \cdot (k_{yi}^w - v) + TM(k_{yi}^w)} \right) \right] \\
(3.64)
\end{aligned}$$

Where $D_{\xi i}^w$ are the residues of the poles. The closed form equation of $D_{\xi i}^w$ for TE and TM modes are shown in Table 3.4. The summation in (3.2), in principle, includes all the SWP's, OP's, and LWP's. From the deformation in Fig 3.8., the SWP's, the LWP's and one of the two OP's are captured. This leads to the following expression for the E-field pattern.

$$F_{\xi} = f_{\xi}^{g0} + \sum_n f_{\xi n}^{sw} + \sum_m f_{\xi n}^{lw} + f_{\xi}^d \quad (3.65)$$

Where

$$f_{\xi}^{g0} = \hat{x} \cdot \hat{\xi} + g_{\xi} \quad (3.66)$$

$$f_{\xi}^d = D_{\xi} e^{-j\Omega(\alpha-v)} \quad (3.67)$$

$$f_{\xi n}^{sw} = D_{\xi n}^{sw} U[Im(s_n^{sw})] e^{-j\Omega(k_{yn}^{sw}-v)} \quad (3.68)$$

$$f_{\xi m}^{lw} = D_{\xi m}^{lw} U[Im(s_n^{sw})] e^{-j\Omega |Im(k_{ym}^{lw})|} U[Im(s_n^{sw})] e^{-j\Omega |Re(k_{ym}^{lw})-v|} \cdot e^{-j\Omega |Re(k_{ym}^{lw})-v|} \quad (3.69)$$

Where $U(x)$ is the Heavyside unit step function

$$g_{\xi} = \text{Res}[G_{\xi}(s); s_0] \quad (3.70)$$

$$D_{\xi j}^w = \text{Res}[G_{\xi}(s); s_j^w] \quad (j = n, m) \quad (3.71)$$

And

$$D_{\xi} = -\frac{1}{2\pi j} \int_{-\infty}^{\infty} G_{\xi}(s) e^{-j\Omega s^2} ds \quad (3.72)$$

Equation (3.70) applies to both SWP and LWP. In the following subsections, the asymptotic contributions in (3.65)–(3.72) are in which presented and discussed.

TABLE 3.4
DIFFRACTION COEFFICIENT

TE_{even}
$D_{\xi i}^{TE_e}(k_x, k_y) = - \left\{ \frac{k_{zi}^w \cdot b_{\xi}(u, k_{yi}^w)}{k_{yi}^w - v} \right\} \left\{ \frac{r_i^{TE_e}(k_{zi}^w)}{k_{yi}^w} \right\} \cdot \frac{1}{te_o}$ $r_i^{TE_e}(k_z) = \frac{k_{z1}^2}{j(\epsilon_r - 1) \sin\left(k_{z1}k_0 \frac{d}{2}\right) \cdot (1 + jk_z \frac{d}{2})}$
TE_{odd}
$D_{\xi i}^{TE_o}(k_x, k_y) = \left\{ \frac{k_{z1i}^w \cdot b_{\xi}(u, k_{yi}^w)}{k_{yi}^w - v} \right\} \left\{ \frac{r_i^{TE_o}(k_{zi}^w)}{k_{yi}^w} \right\} \cdot \frac{1}{te_e}$ $r_i^{TE_o}(k_z) = \frac{k_z^2}{j(\epsilon_r - 1) \sin\left(k_{z1}k_0 \frac{d}{2}\right) \cdot (1 + jk_z \frac{d}{2})}$
TM_{even}
$D_{\xi i}^{TM_o}(k_x, k_y) = - \left\{ \frac{k_{zi}^w \cdot b_{\xi}(u, k_{yi}^w)}{k_{yi}^w - v} \right\} \left\{ \frac{r_i^{TM_o}(k_{zi}^w)}{k_{yi}^w} \right\} \cdot \frac{1}{tm_e}$ $r_i^{TM_o}(k_z) = \frac{k_{z1}^2}{(\epsilon_r - 1) \cos\left(k_{z1}k_0 \frac{d}{2}\right) \cdot \left\{ \epsilon_r + jk_z \frac{d}{2} [1 - k_z^2(\epsilon_r + 1)] \right\}}$
TM_{odd}
$D_{\xi i}^{TM_e}(k_x, k_y) = \left\{ \frac{k_{z1i}^w \cdot b_{\xi}(u, k_{yi}^w)}{k_{yi}^w - v} \right\} \left\{ \frac{r_i^{TM_e}(k_{zi}^w)}{k_{yi}^w} \right\} \cdot \frac{1}{tm_o}$ $r_i^{TM_e}(k_z) = \frac{\epsilon_r k_z^2}{(\epsilon_r - 1) \cos\left(k_{z1}k_0 \frac{d}{2}\right) \cdot \left\{ \epsilon_r + jk_z \frac{d}{2} [1 - k_z^2(\epsilon_r + 1)] \right\}}$

3.6. Geometrical Optics

The term f_{ξ}^{go} is the GO contribution, that consists of the direct contribution $\hat{x} \cdot \hat{\xi}$ from the unit dipole and the contribution g_{ξ} .

For: $0^\circ < \beta < 180^\circ$

$$E_{\phi}(\theta, \phi) = \frac{jk_0\eta}{4\pi r} e^{-jk_0r} \frac{\sin \phi \cos \theta [T \cdot \cos(k_0Td) + j \cos \theta \sin(k_0Td)]}{tm_{even} \cdot tm_{odd}} \quad (3.73)$$

$$E_{\theta}(\theta, \phi) = \frac{-jk_0\eta}{4\pi r} e^{-jk_0r} \frac{\cos \theta \cos \phi [jT^2 \cdot \sin(k_0Td) + \epsilon_r T \cos \theta \cdot \cos(k_0Td)]}{tm_{even} \cdot tm_{odd}} \quad (3.74)$$

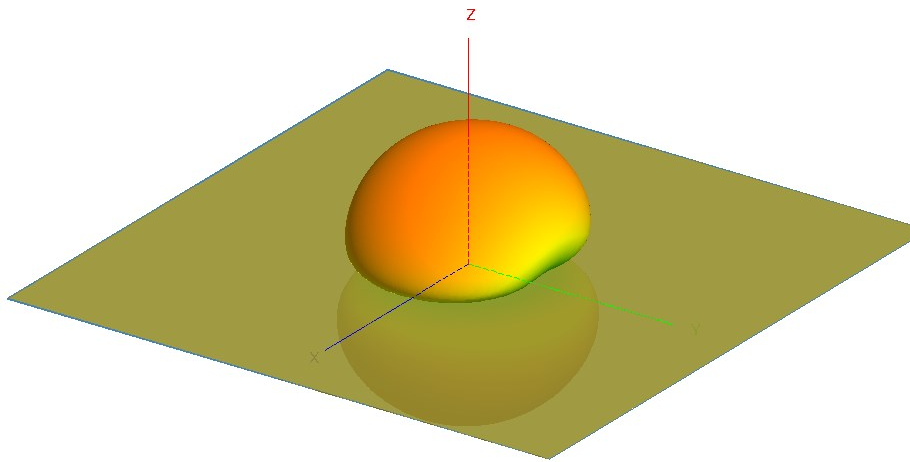
For: $180^\circ < \beta < 360^\circ$

$$E_{\phi}(\theta, \phi) = \frac{jk_0\eta}{4\pi r} e^{-jk_0r} \frac{\sin \phi \cos \theta T}{tm_{even} \cdot tm_{odd}} \quad (3.75)$$

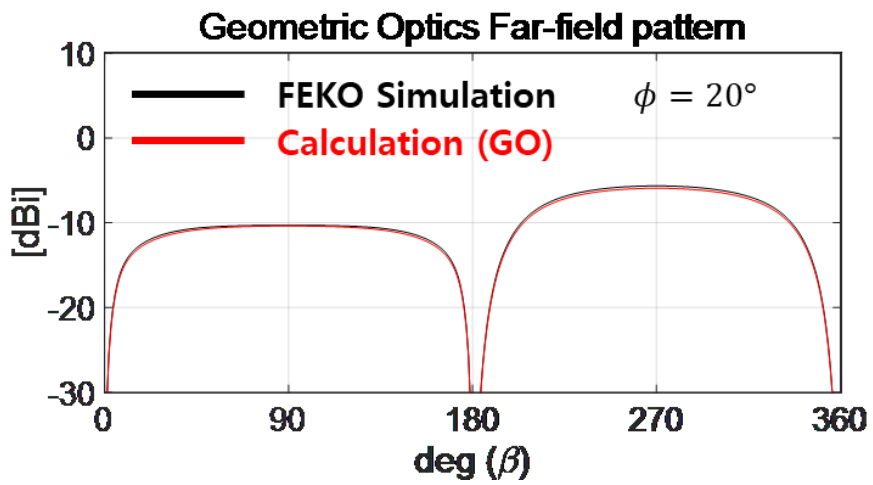
$$E_{\theta}(\theta, \phi) = \frac{-jk_0\eta}{4\pi r} e^{-jk_0r} \frac{\cos^2 \theta \cos \phi \epsilon_r T}{tm_{even} \cdot tm_{odd}} \quad (3.76)$$

where

$$T = \sqrt{\epsilon_r - \sin^2 \theta} \quad (3.77)$$



(a)



(b)

Fig. 3.9. Radiation Pattern for infinite dielectric slab: (a) 3D simulation results, and (b) comparison.

3.6. Diffracted Rays

3.6.1. Surface wave diffracted wave

Next, let us consider the SW diffraction mechanism. This mechanism has to satisfy the generalized Fermat principle. In applying this principle to the present case, it is worth noting that part of the ray path is defined in an inhomogeneous medium, where the phase velocity of the wave is less than the speed of the light in free space. Then, each SW ray emanating from the source diffracts on a cone whose aperture is smaller than that of the usual GTD diffraction cone. The location of Q depends on the phase velocity of the SW; in particular, according to the generalized Fermat principle, this location can be defined by

$$k_{\rho n}^{lw} \cos \Psi_n^{lw} = u \quad (3.78)$$

is the radial normalized wave number of the SW (it is greater than unity) and Ψ_n^{sw} is the angle between the x axis and the position vector L_n^{sw} of Q_n^{sw} .

$$\cos \Psi_n^{sw} = \frac{\vec{L}_n^{sw}}{L_n^{sw}} \hat{x} \quad (3.79)$$

From another point of view, the ray that contributes to a given observation point arises from a diffraction point Q at the upper edge of the truncation that precedes with respect to the ordinary diffraction point, defined by a free-space ray tracing. The phase term of this ray contribution is position vector

$$\begin{aligned}\Phi &= k_0 \left(-k_{\rho n}^{sw} L_n^{sw} + \vec{L}_n^{sw} \cdot \mathbf{r} \right) \\ &= k_0 L_y \left(k_{yn}^{sw} - \nu \right)\end{aligned}\tag{3.80}$$

Which is recognized as the phase term in (3.68). This leads to interpret the contribution $f_{\xi j}^{sw}$ in (3.65) as the ray field produced by diffraction of SW ray excited by the source. The above considerations allow us to use $D_{\xi j}^w$ as a diffraction coefficient. In other terms, $D_{\xi j}^w$ includes the amplitude of the SW excited by a unit dipole. Although this may be somewhat unconventional for a GTD diffraction coefficient, it is found convenient for the patch antenna applications with which we are concerned.

3.6.2. Leaky wave diffracted wave

As mentioned earlier, LWP's may be captured in the SDP deformation. At variance with the SWP contribution, the LWP's do not coalesce with the saddle point. their residues give the contributions $f_{\xi j}^{sw}$ that are recognized as the LW diffracted fields.

The LW diffracted ray arises from a point Q; that again satisfies the generalized Fermat principle. In this case, this principle can be expressed by

$$\operatorname{Re}(k_{\rho m}^{lw}) \cos \Psi_m^{lw} = u \quad (3.81)$$

Where is the radial, normalized propagation constant of the LW and denotes the position of the LW diffraction point with respect to the x axis. Similar considerations, as those for the SW diffraction, apply to the present case. In particular, the term

$$D_{\xi m}^{lw} e^{-\Omega | \operatorname{Im}(k_{ym}^{lw}) |} \quad (3.82)$$

Provides a diffraction coefficient to be applied to the current amplitude of the HED. In general, it gives a rather weak contribution due to the exponential decay which affects the LW before reaching the edge.

3.6.3. Space wave diffracted wave

Let us now consider the contribution f_{ξ}^d in (3.65). Its phase term $e^{-j\Omega(\alpha-v)}$ is that of a ray field emanating from an edge point \mathbf{Q}' that satisfies the ordinary Fermat principle in free-space. Then, f_{ξ}^d can be interpreted as the space-wave diffraction contribution, namely

the diffraction of the GO wave at the truncation.

3.7. Numerical Results

3.7.1. Analysis of both sides truncated substrate

In this section, comparison between PO and CST results will be presented, with an objective to find the range of validity of the PO approximation. The geometry we are dealing with is shown in Fig. 3.1, and consists of a dielectric slab with dielectric constant ϵ_r and thickness d , which is fed by an electric dipole source with unit current, located at the air–dielectric interface, the upper and lower edge of the truncation. Fig.3.10. shows the total ϕ component $|F_\phi|$ of the normalized far–field pattern (continuous line) for a HED which is placed at $L_y = 1 \lambda_0$ from the upper edge and at $L_y = 3 \lambda_0$ from the lower edge. It is worth noting that for the H plane cut, the TE0 surface wave diffraction, space wave diffraction and Geometric Optics are considered. In addition, the thickness of the substrate $d = 0.0381 \lambda_0$ and the permittivity $\epsilon_r = 4$ are given. The field equations for Fig 3.10 are given as

$$\begin{aligned}
 F_\xi &= F_\xi^{upper} + F_\xi^{lower} \\
 &= D_\xi^w(k_{yi}^w) \cdot e^{-j\Omega(k_{yi}^w - v)} + D_\xi^w(-k_{yi}^w) \cdot e^{-j3\Omega(-k_{yi}^w - v)}
 \end{aligned} \tag{3.83}$$

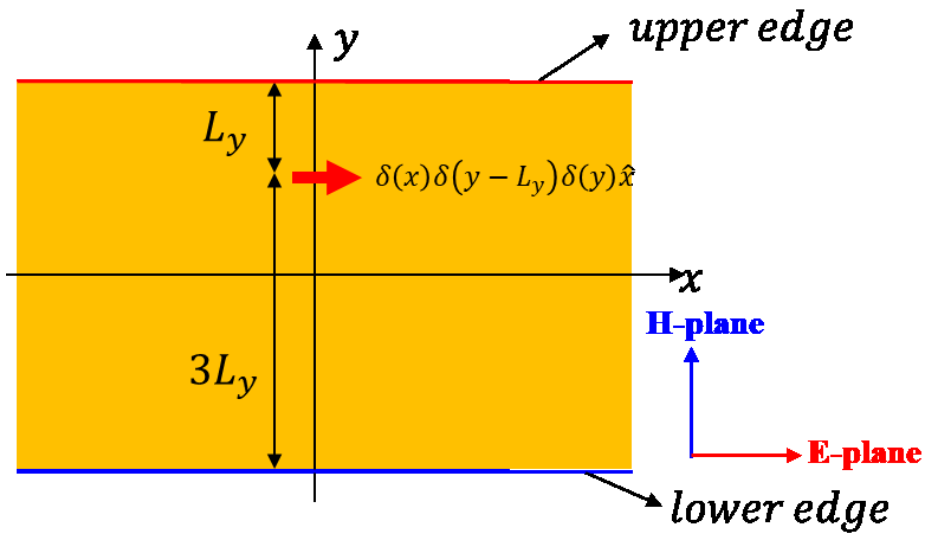


Fig. 3.10. Truncated dielectric slab modeling

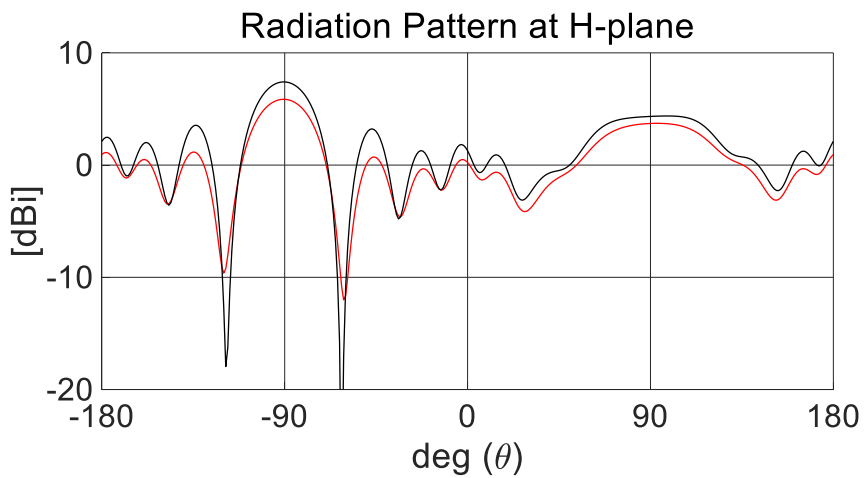
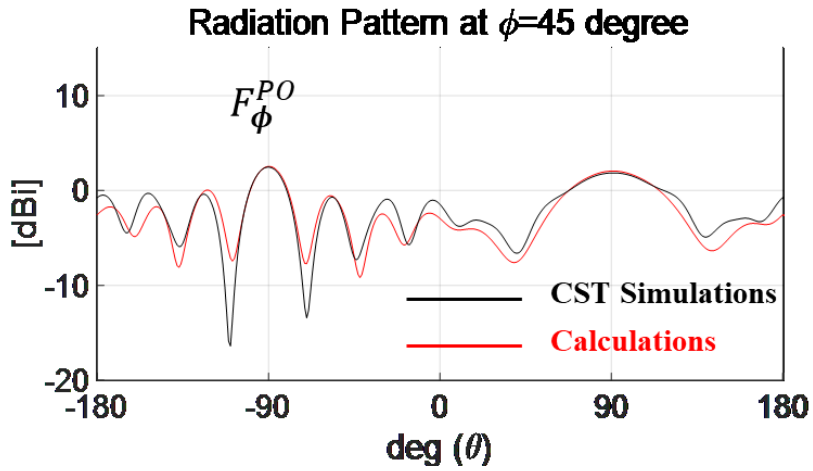
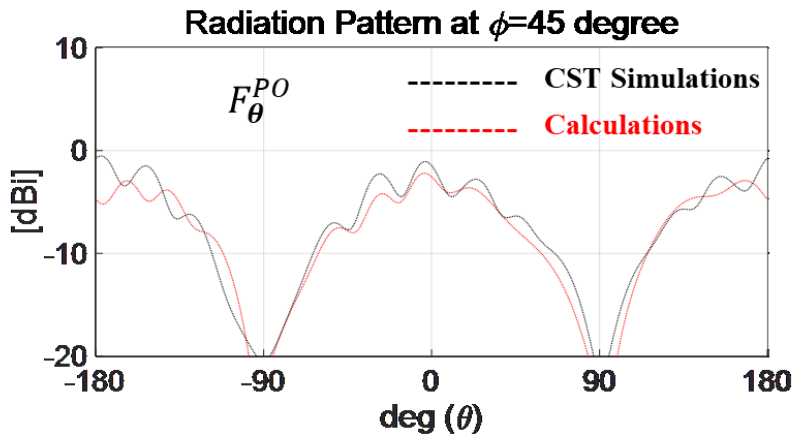


Fig. 3.11. Radiation pattern at H-plane for truncated dielectric slab (ϕ component, $\epsilon_r = 4$).

Fig. 3.11 shows the ϕ of the far-field radiation pattern in the plane cut $\phi = 90^\circ$ for the Fig. 3.10. And Fig. 3.12 shows the ϕ and θ of the far-field radiation pattern in the plane cut $\phi = 45^\circ$. Fig. 3.13~3.14 show the various diffracted ray components of the far-field. As shown in Fig. 3.13, the fundamental TE_{odd} and TM_{odd} modes are excited. At this time, the fundamental TE_{odd} mode becomes the dominant factor of the radiated field, while the TM surface wave diffraction provides a negligible contribution. This fact can be seen from Fig. 3.6 SDP diagram that the TE SW pole is closer to the saddle point than the TM SW pole, so it is more affected by the diffraction amplitude. Fig 3.14 shows the space-wave diffracted field amplitude for ϕ and θ , which is results from the direct numerical integration (dashed line) in equation (3.72). Finally, Fig. 3.15 shows the results for Geometric Optics for ϕ and θ . Through the surface wave diffraction and space-wave diffraction, it can be confirmed that the amplitude is maximized in the direction of $\theta=90^\circ$. On the other hand, in the geometric optics, the direct ray and the reflected ray are canceled and do not exist in the direction of $\theta=90^\circ$. Fig. 3.16 shows the far-field pattern and the components constituting it when the permittivity is given as $\epsilon_r = 12.2$ in the structure of Fig. 3.10. In this case, the diffraction contribution from the TE_{odd} SW's, is particularly noticeable, while the other components provides a negligible contribution. In particular, the higher the dielectric constant of the substrate, the smaller the GO contribution and the field diffraction by TE_{odd} becomes dominant. LW diffracted ray has the weakest



(a)



(b)

Fig. 3.12. Radiation pattern at Diagonal plane for truncated dielectric slab: (a) ϕ component, and (b) θ component

contribution due to the exponential decay before reaching the edge.

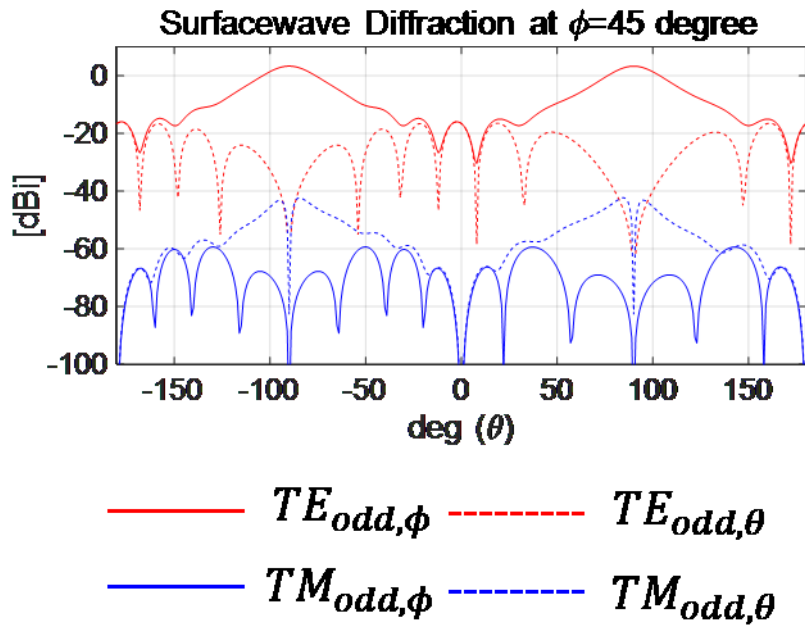


Fig. 3.13. Surface-wave diffraction contribution.

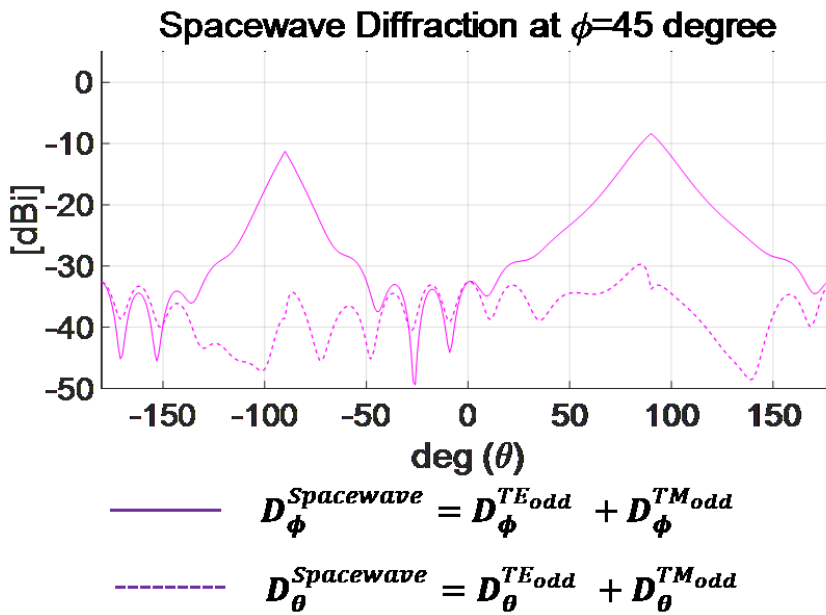


Fig. 3.14. Space-wave diffraction contribution.

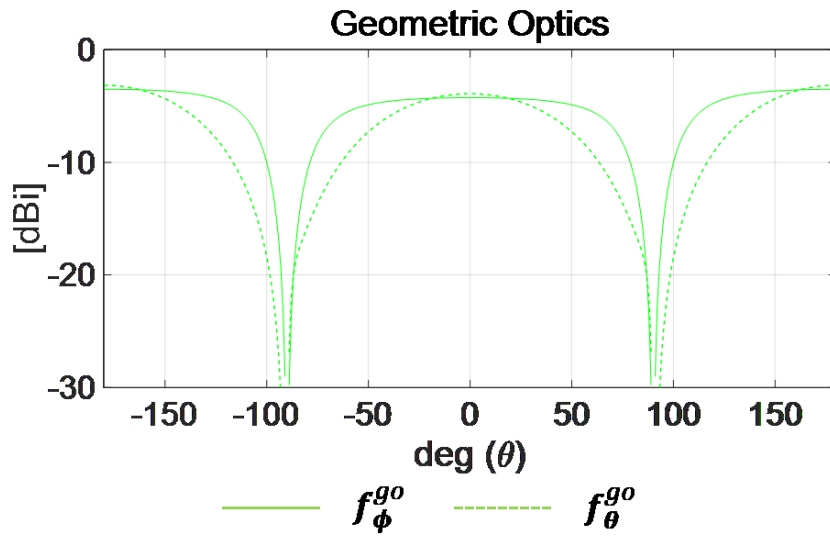
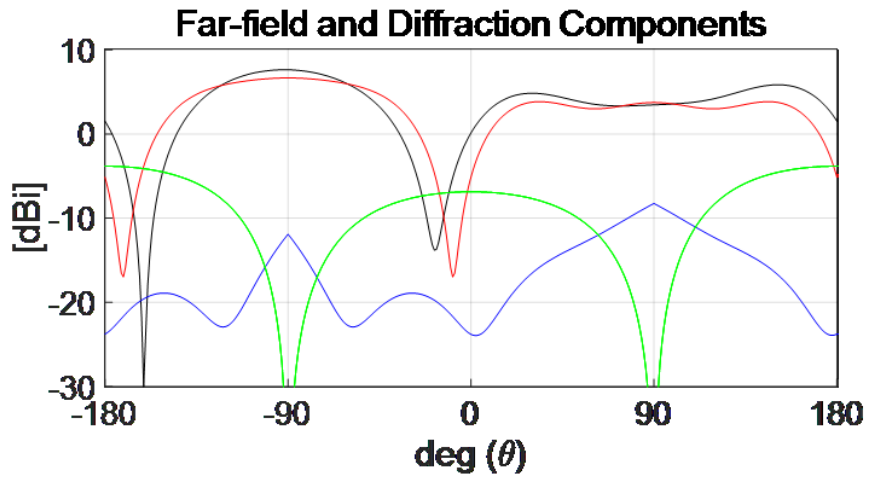


Fig. 3.15. Geometric Optics contribution.



Far field at H-plane

TE0 Surface wave diffraction

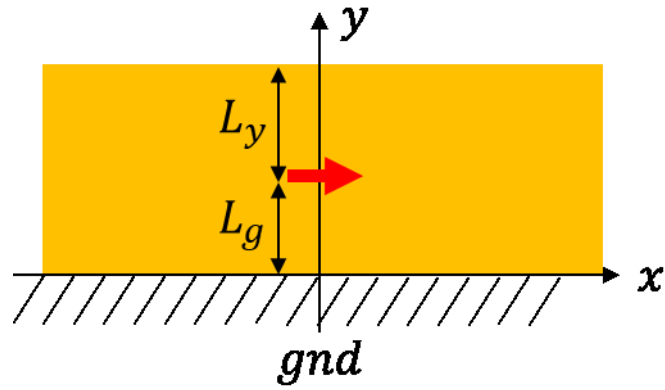
Space wave diffraction

Geometric Optics : Direct Wave and Reflected Wave

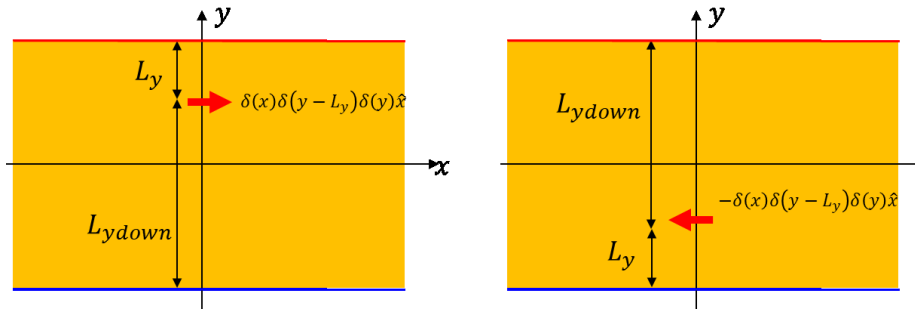
Fig. 3.16. Diffracted ray and GO contributions for $\epsilon_r = 12.2$.

3.7.2. Analysis of a substrate standing perpendicular to the ground plane

Fig 3.17 (a) shows the structure in which the truncated dielectric slab is perpendicular to the ground plane. The structure of Fig 3.17 (a) can be equivalent to the sum of two structure as shown in Fig.3.17 (b) using image theory. At this time, Fig 3.17(b) is covered in Fig 3.10 in subsection 3.7.1. Fig 3.17(c) is a structure in which the sign of the dipole source is opposite to that of the Fig 3.17 (b) and is symmetrical to each other. Fig 3.18 presents the far-field pattern in H-plane for a structure with permittivity $\epsilon_r = 12.2$, $L_y = 0.2 \lambda_0$ In particular, the directivity of radiation has a high gain of 4.5 dBi. The design of the subarray antenna using high dielectric will be discussed in subsection 3.8.

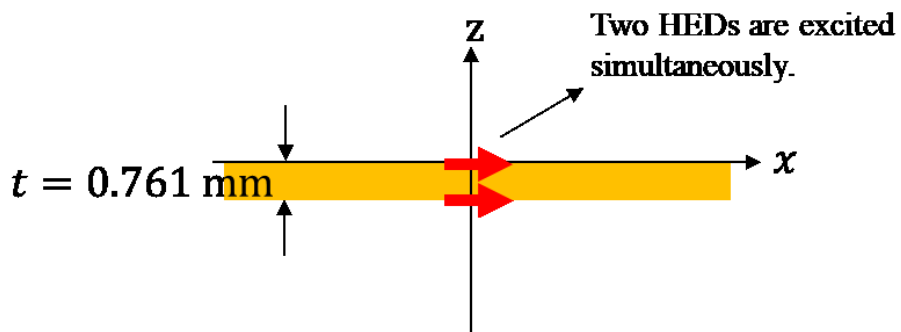


(a)



(b)

(c)



(d)

Fig. 3.17. (a) Truncated dielectric slab over the ground plane, (b) Image theory model 1, (c) Image theory model 2, and (d) top view for two HEDs on the substrate.

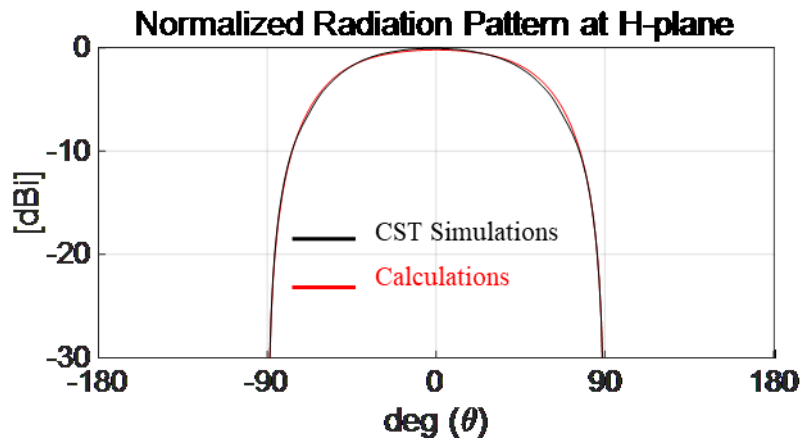
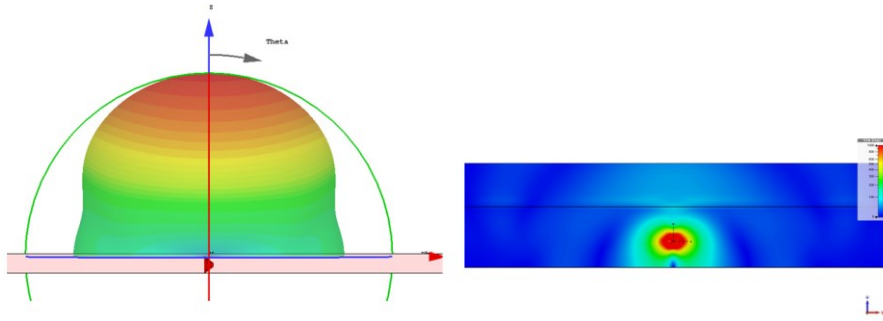


Fig. 3.18. Far-field pattern for $\epsilon_r = 12.2$, $L_y = 0.2 \lambda_0$.

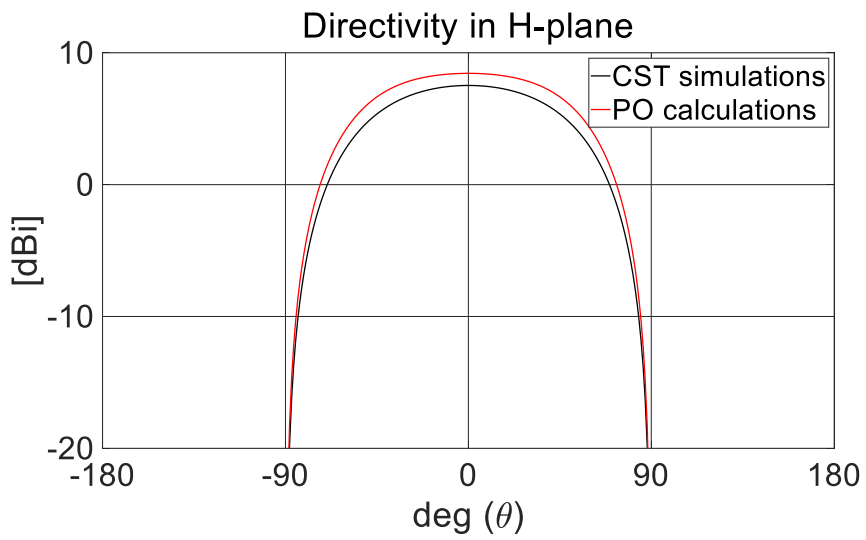
3.7.3. Limitation of the Physical Optics.

The reflection and the scattering properties of surface wave in an abruptly ended dielectric slab waveguide have been analyzed in a few papers [7], [8]. The most evident lack of PO for grounded-slab configurations is the absence of an estimate of the guided waves reflection at the open ended interface [2]. Fig. 3.19 and Fig.3.20. show the directivity calculated using PO and the directivity using simulation when the dielectric constant is 5 and 12, respectively.

When the dielectric constant is 12, the electric energy distribution presents on the substrate looks much larger than the dielectric constant is 5, which is in the abruptly ended structure. It is caused by surface wave reflection. However, for low dielectric constant, PO is relatively well matched, and overall, the radiation component of dielectric slab antenna is composed of TE₀ mode and GO component.

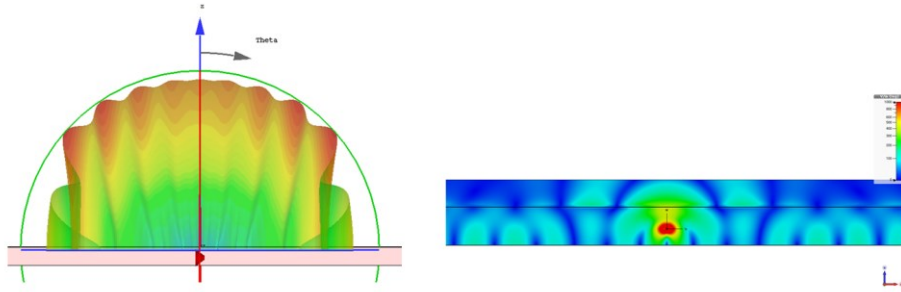


(a)

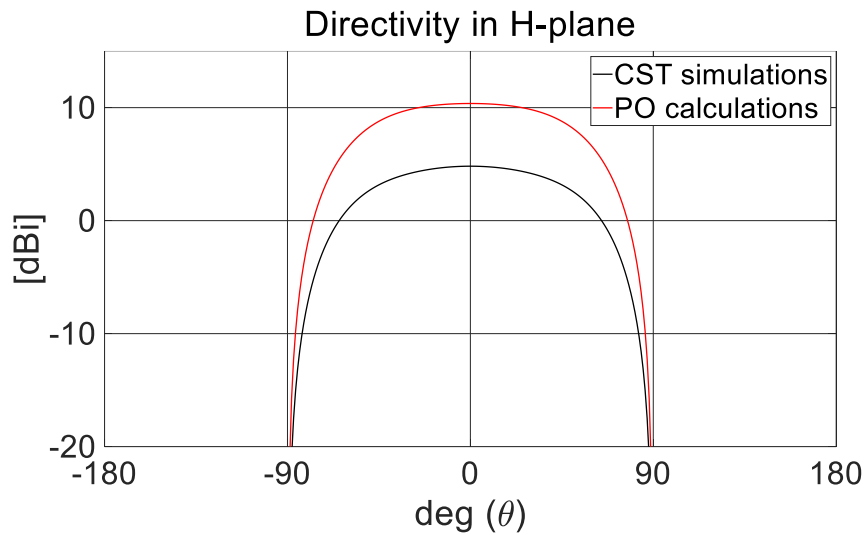


(b)

Fig. 3.19. Directivity for $\epsilon_r = 5$, $L_y = 0.2 \lambda_0$: (a) Radiation pattern and E-field distribution, and (b) comparison PO calculations with CST simulations.



(a)



(b)

Fig. 3.20. Directivity for $\epsilon_r = 12$, $L_y = 0.2 \lambda_0$. : (a) Radiation pattern and E-field distribution, and (b) comparison PO calculations with CST simulations.

3.8. Implementation of Bow-tie printed Dipole Array

3.8.1. Motivation

In an antenna array, mutual coupling between antenna elements degrades the performance of the array signal processing algorithm [9]. There are various way of reducing the mutual coupling. Electromagnetic band-gap (EBG) structures is an attractive way to suppress the mutual coupling. However it occupies a large area and has the complex structure. So it is usually difficult to implement. Parasitic elements in an antenna is another way to reduce mutual coupling. Parasitic elements make a double-coupling path. So it can be used to cancel out direct coupling depending on the position of the antenna and the parasitic elements [10], [11].

In this subsection, we analyze an effect of surface wave on the mutual coupling for H-plane bow-tie array antenna. But a surface wave guided along the substrate is observed in the antenna having a substrate. The diffracted field at the edge of the substrate can be used to improve the mutual coupling characteristic. An 15 by 1 bow-tie array is designed and simulation shows that the coupling between two adjacent antennas is less than -20 dB in the $13.6 \sim 17.8$ GHz band.

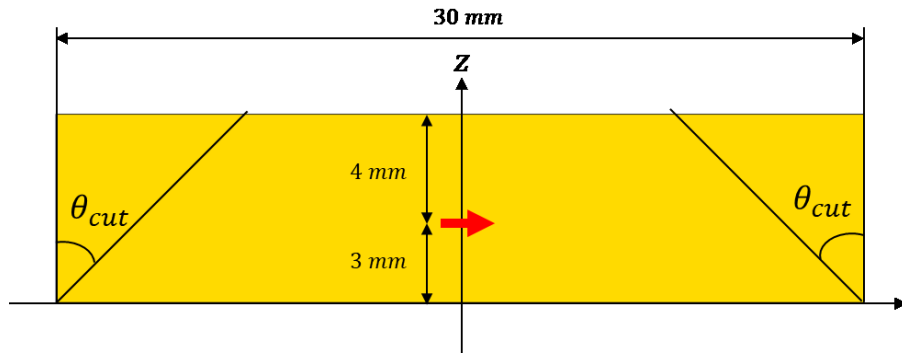
In this chapter, we propose a ka-band bow tie array antenna with low mutual coupling using surface wave diffraction. In addition, the

ohmic sheet is introduced to maximize the effect of the coupling reduction. Then, the 15 by 1 1D bow-tie array with ground is implemented using a substrate with a high dielectric constant.

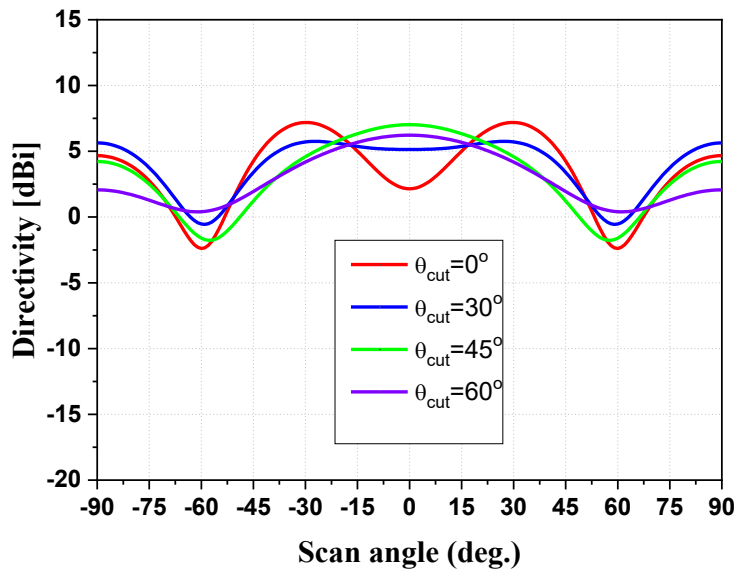
3.8.2 Single Antenna Design

The proposed printed bow-tie element is designed on the substrate with $\epsilon_r = 12.2$, loss tangent = 0.0023 and thickness = 0.761 mm (Roger TMM13i) and the antenna structure is mounted on a ground plane. In Fig 3.21(a), the E-plane pattern at 18 GHz is plotted as shown in Fig.3.21(b) when the side of the antenna is cut at 0, 30, 45 and 60 degrees. If the side of the substrate doesn't be cut, an unwanted radiation pattern is formed as null is generated in broadside as shown in Fig 3.21(b). To eliminate the broadside null phenomenon, the beam pattern is observed by increasing the side tapering angle at the edge of the substrate. At $\theta_{cut} = 60^\circ$, the beam pattern is the broadest and the side lobe is the lowest. In Fig. 3.22, 3D patterns are compared when the $\theta_{cut} = 0^\circ$ and $\theta_{cut} = 60^\circ$. After several fine tunings, the geometry, parameters, and top and bottom views for a prototype of the proposed antenna can be shown in Fig. 3.23. The antenna consists of two identical printed bow-ties, one on the top and one on the bottom of the substrate material. The top and bottom bows are connected to the parallel feedline. Between the parallel feedline, there are two half air holes. These holes plays a

role to meet the impedance matching. Fig 3.24 shows the radiation pattern results according to the ground size as shown in Fig 3.23 (d). When the length L of one side of the ground is 100 mm and 400 mm, there is little difference in the pattern, so L is designed as 100 mm. As shown in Fig 3.23 (c), the edge of the substrate be cut in the direction of 45 degrees so that the reflection of surface wave traveling along the substrate is minimized.

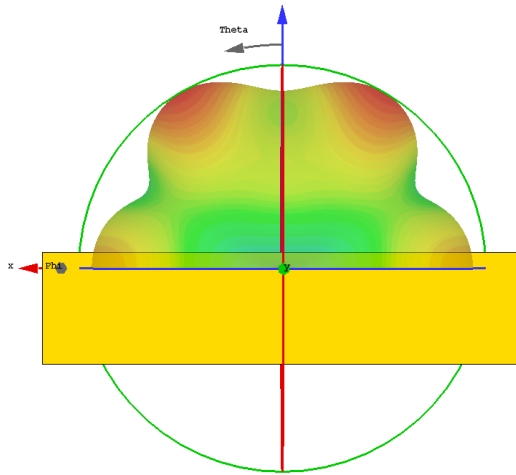


(a)

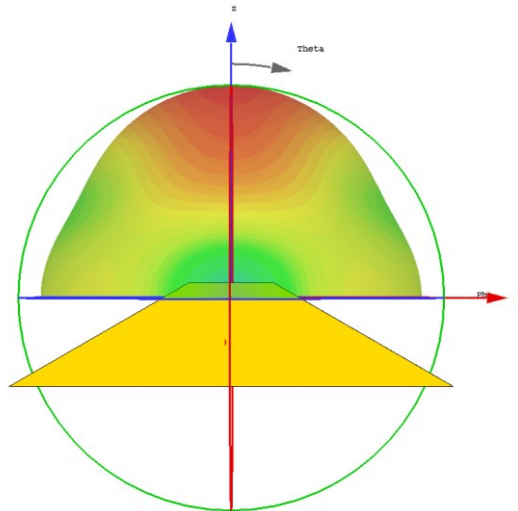


(b)

Fig. 3.21. (a) An HED on the finite dielectric substrate over the ground, and its (b) directivity pattern depend on cutting angle.

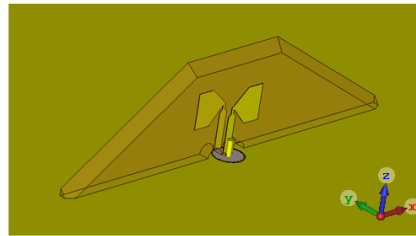
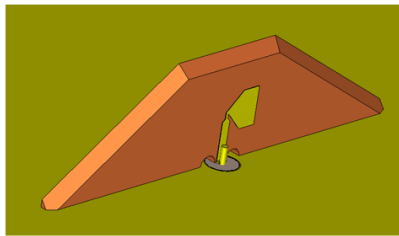
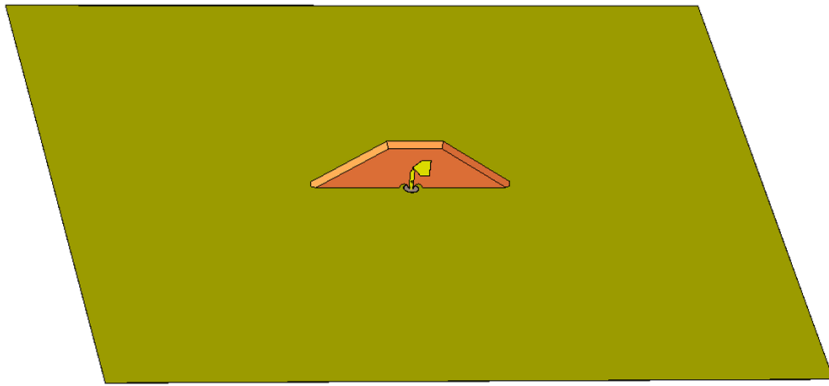


(a)

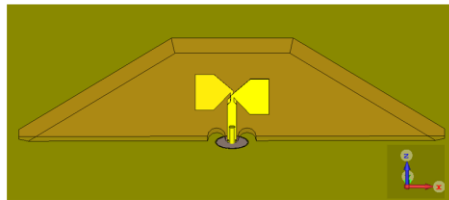
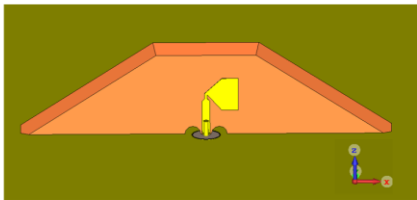


(b)

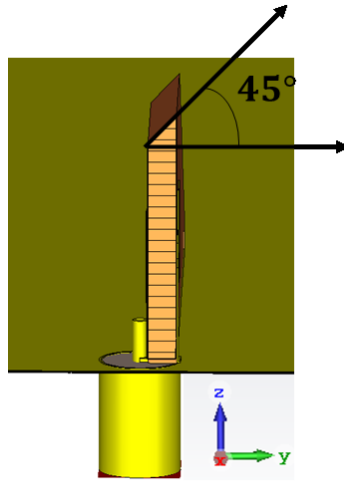
Fig. 3.22. 3D directivity pattern for Fig.3.21: (a) $\theta_{cut} = 0^\circ$, and
 (b) $\theta_{cut} = 60^\circ$.



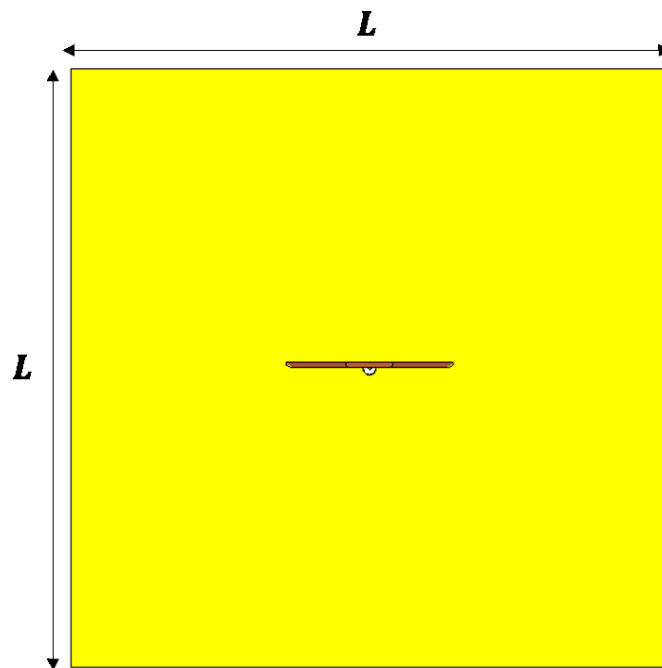
(a) Perspective view



(b) Front view



(c) Side view



(d) Top view

Fig. 3.23. An HED on the substrate with trapezoidal type over the ground: (a) Perspective view, (b) Front view, (c) Side view, and (d) Top view.

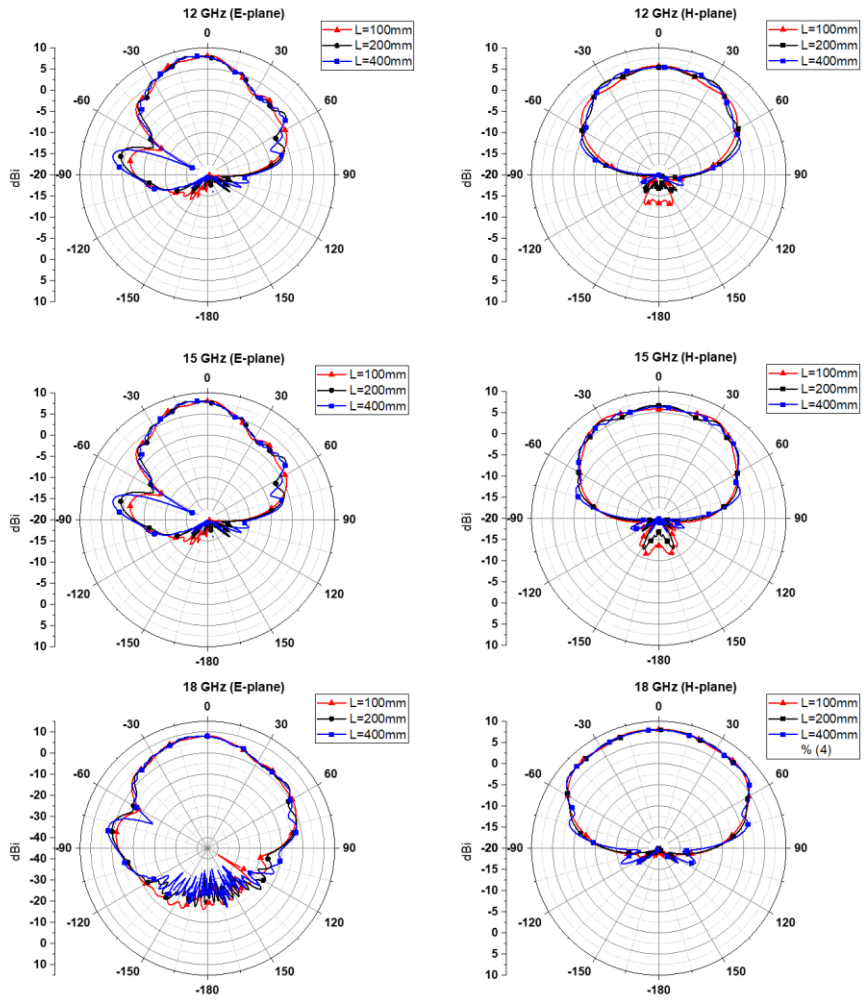
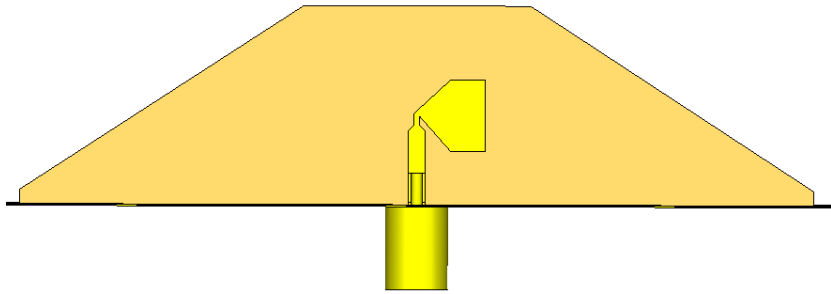
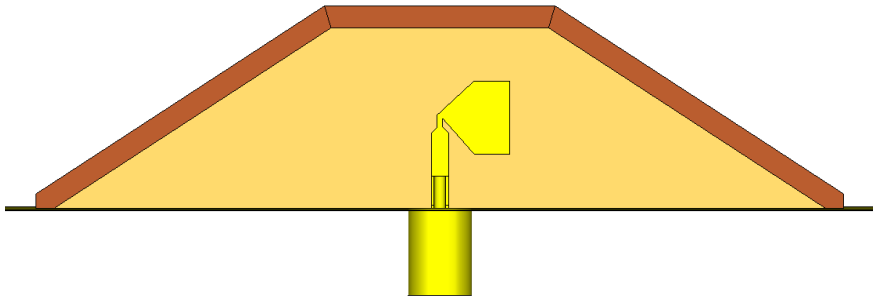


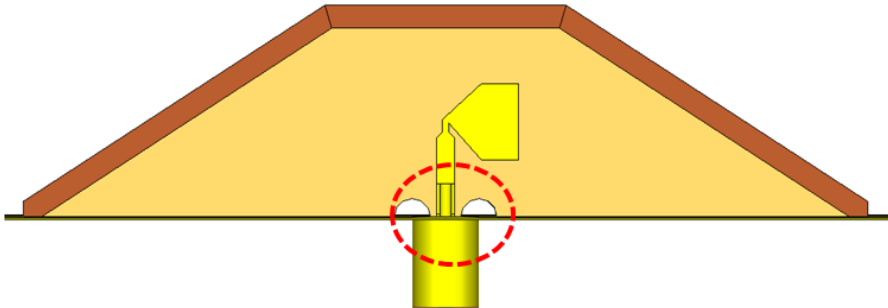
Fig. 3.24. E and H-plane single element pattern.



(a)



(b)



(c)

Fig. 3.25. Single element model: (a) model 1, (b) model 2, and (c) model 3.

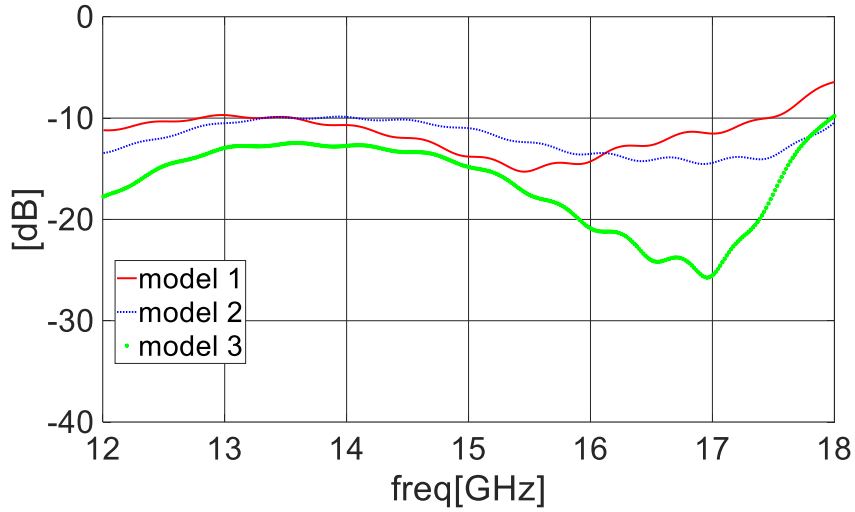


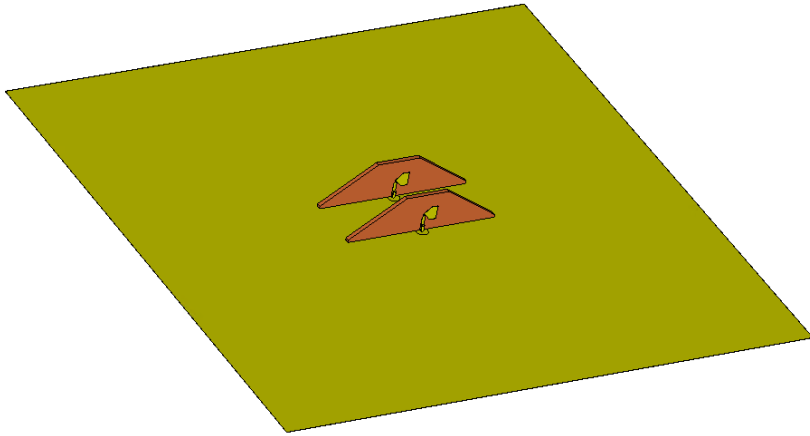
Fig. 3.26. Return loss characteristics for Fig. 3.25.

3.8.3 Return Loss Characteristics

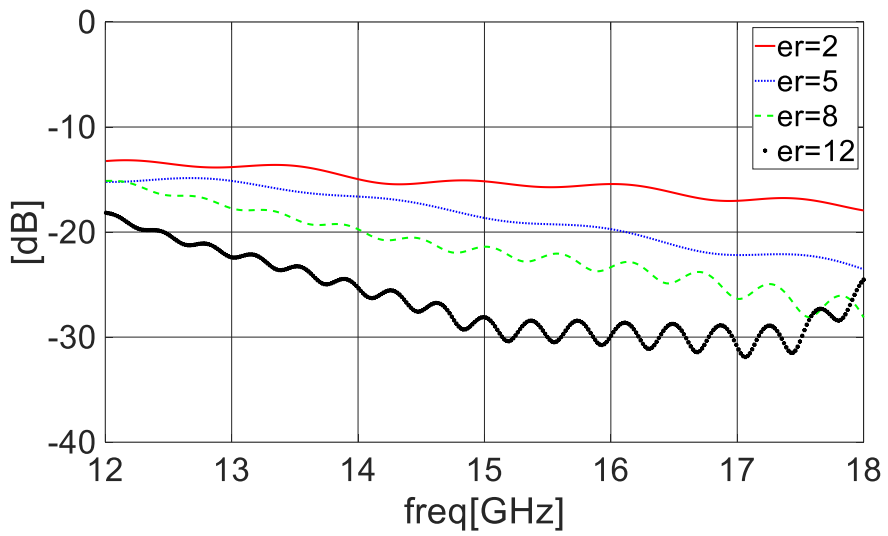
Fig. 3.25 (a) shows the model 1, which is the basic model. Antenna matching is difficult, because the teflon permittivity of coaxial feeding is 2.2 and the substrate permittivity is 12.2, so reflection occurs due to a very large difference in permittivity. To reduce the effect of the difference in permittivity, if a hole is drilled in the area where the teflon and TMM substrate abut as shown in Fig. 3.25 (c), then, the reflection effect can be reduced as shown in Fig. 3.26.

3.8.4 Mutual Coupling

Fig. 3.27 (a) shows the two element array model. The array is in the H-plane direction and the spacing between elements is 10 mm to be $0.5 \lambda_0$ at 15 GHz. Fig. 3.27 (b) shows the mutual coupling characteristic that the coupling decreases over the entire band as the permittivity increases. As the dielectric constant increases, the surface wave power increases, which causes a cancellation effect between GO and surface wave each other and contributing to coupling reduction.



(a)



(b)

Fig. 3.27. Two element array: (a) geometrical model, and (b) mutual coupling on dielectric constant changes.

3.8.3 Measurements

3.8.3.1 Single Element

Fig. 3.28 shows the fabricated single element. At this time, copper ground is used as the ground. Fig. 3.29 (a) is the result of comparing the measurement and CST simulation results in H-plane at 15 GHz. Also, Fig. 3.29 (b) shows the PO calculations and measurements.

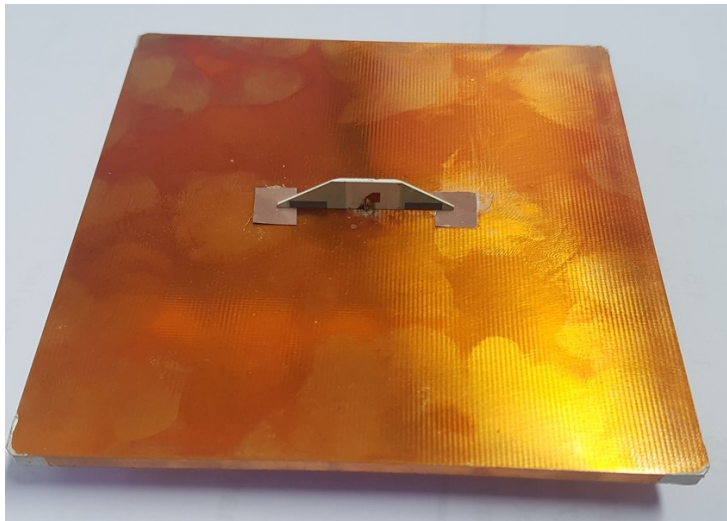
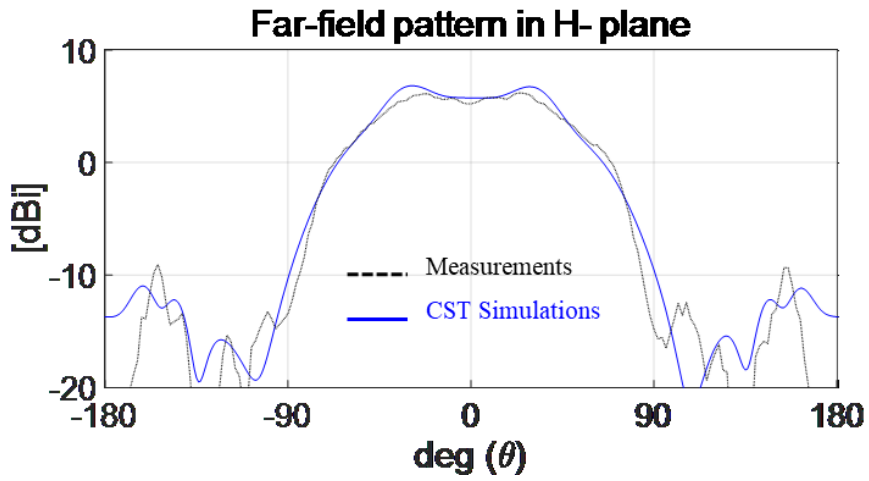
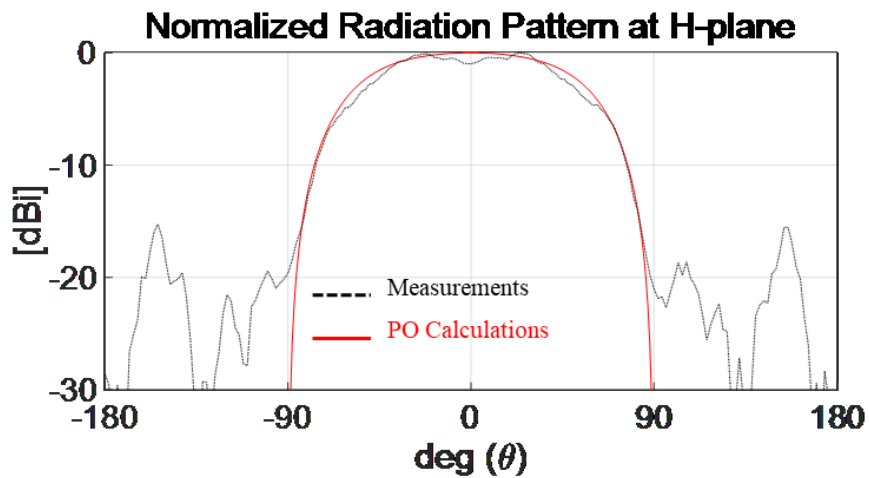


Fig. 3.28. Fabricated single element.



(a)



(b)

Fig. 3.29. Far-field pattern in H-plane: (a) Measurements VS CST Simulations, and (b) Measurements VS PO Calculations.

3.8.3.2 H-plane 1-D Array

Fig. 3.30 shows the fabricated 15x1 subarray. At this time, copper ground is used as the ground. A rectangular 250 Ohm Ohmic sheet is attached to both sides of the printed bow-tie. By investigating the current density distribution on the substrate with frequency, the appropriate positions of the resistive films are determined [12]. Ohmic sheet plays a role of reducing mutual coupling by attenuating the surface wave traveling in the x direction. Fig. 3.31 is the result of comparing the simulation and measurement of the return loss (a) and the coupling between the center element and the adjacent element (b). In particular, the coupling was less than -20 dB in the band after 12.8 GHz. Fig 3.32 compares the radiation patterns of the ku-band in the E and H-plane at 12,14,16,18 GHz.

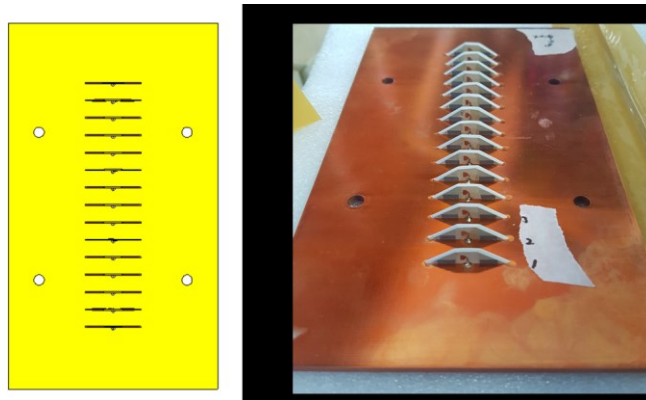
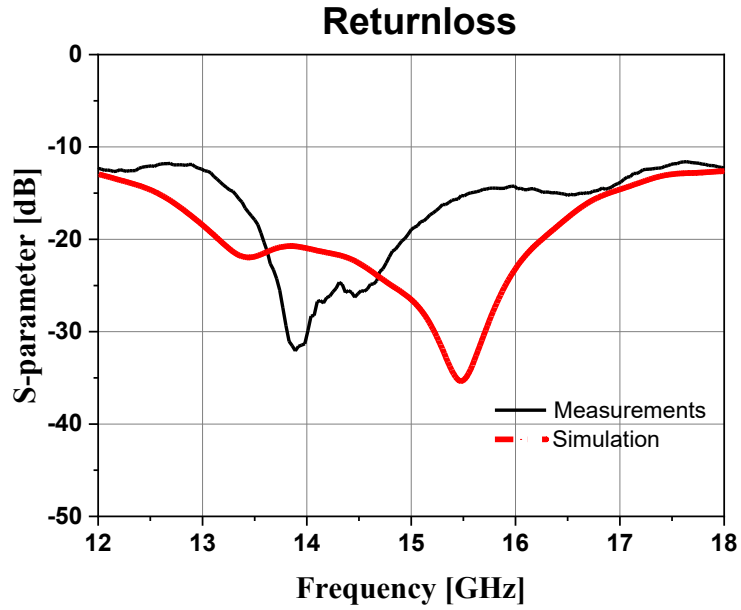
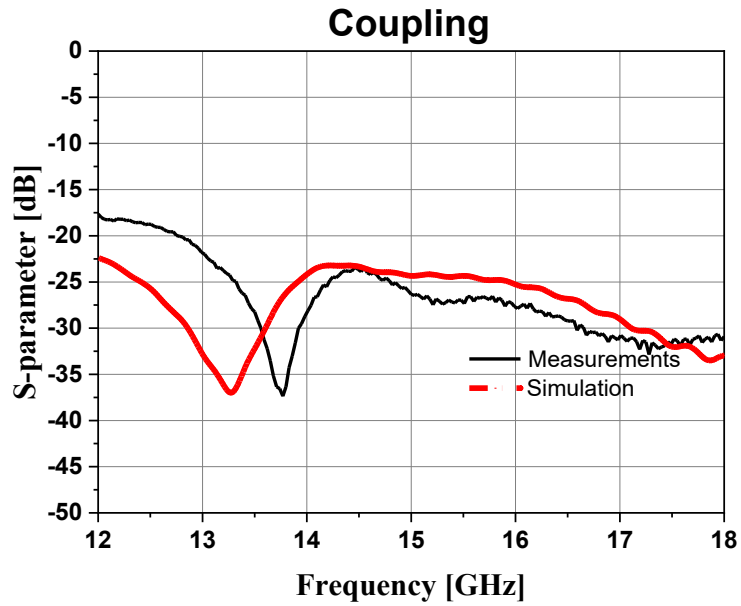


Fig. 3.30. Fabricated 15x1 H-plane Array.



(a)



(b)

Fig. 3.31. S-parameter results: (a) Return loss, and (b) Mutual coupling between the center element and the adjacent element

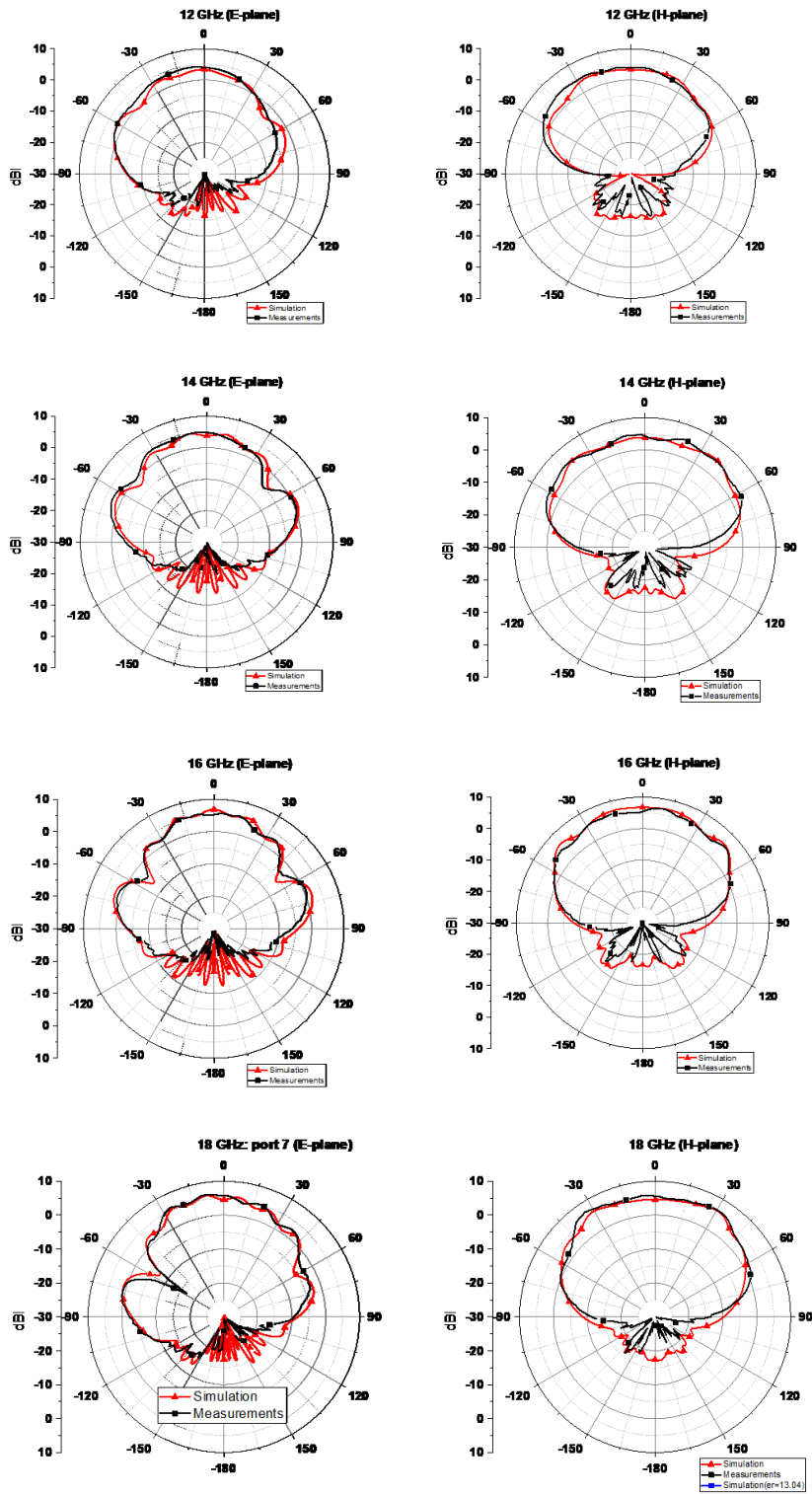


Fig. 3.32 E and H-plane co-polarization active element pattern of 15x1.

3.9. Conclusions

The principle of a printed bow-tie antenna on a high dielectric substrate is presented. For the sake of simplicity, it is assumed that the infinitesimal horizontal-electric dipole (HED) with unit current is located on the dielectric slab. Throughout this chapter the effectiveness of the PO approximation has been demonstrated in describing diffraction effects of the various wave species excited by an HED on a dielectric substrate.

By using the equivalence principle and the multilayered structure theory, the polarization currents are derived in the form of the spectral domain. And then, the far-field can be expressed as a Sommerfeld type representation. The saddle-point method for the asymptotic evaluation of an integral is introduced to implement the integration of the far-field equation.

Through these PO calculation process, it is theoretically concluded that the components of the antenna far-field are composed of geometric optics in which the direct ray radiated directly from the HED and the reflected wave by the dielectric are combined, and the diffracted ray generated by the space wave, surface wave, and leaky wave. In order to verify the validity of the theory, the electromagnetic wave analysis programs CST MWS and FEKO are used to compare and verify the theoretically obtained closed form.

According to the results of the study, in the case of a high dielectric substrate with dielectric constant of 10 or more, the main component that constitutes the radiation pattern is TE_0 surface-wave (SW) diffracted ray generated from the edge of the dielectric slab. In addition, the directivity of the antenna can obtain a high gain of 6 dBi or more, which is advantageous for single antenna design.

Finally, based on the previously derived theory, a ku-band printed Bow-tie array antenna with low mutual coupling is proposed. The diffracted ray induced at the edge of the truncated dielectric slab not only generates high gain, but also can reduce mutual coupling due to the cancellation effect of direct ray and reflected ray. In addition, an ohmic sheet is added on the dielectric slab of the single element to attenuate the surface waves traveling to the side and it leads to minimize the mutual coupling. In particular, there is an advantage of obtaining high gain and low mutual coupling without adding additional structures. The single element is designed and fabricated as a 1D sub-array in the H-plane. It is confirmed that the gain is higher than 6 dBi, and the mutual coupling is less than -20 dB in the band after 12.8 GHz. The proposed model doesn't need any other structure such as EBG or parasitic elements. So it is very easy to implement compared with the conventional array antenna.

3.10. References

[1] A. K. Bhattacharyya, *Electromagnetic Fields in Multilayered Structures Theory and Applications.*, 1994.

[2] S. Maci, L. Borselli, and L. Rossi, "Diffraction at the edge of a truncated grounded dielectric slab," *IEEE Trans. Antennas Propagat.*, vol. 44, pp. 863–873, June. 1996.

[3] S. Maci, L. Borselli, and A. Cucurachi, "Diffraction from a truncated grounded dielectric slab: A comparative full-wave/physical-optics analysis," *IEEE Trans. Antennas Propag.*, vol. 48, no. 1, pp. 48–57, Jan. 2000.

[4] R.E. Collin, *Field Theory of Guided Waves* 2nd Ed., 1990.

[5] A. Ishimaru, *Electromagnetic Wave Propagation Radiation and Scattering*, Englewood Cliffs, NJ:Prentice Hall, 1991.

[6] P. Gelin, M. Petenzi, and J. Citerne, "Rigorous analysis of the scattering of surface waves in an abruptly ended slab dielectric waveguide," *IEEE Trans. Microwave Theory Tech.*, vol. MTT–29, pp. 107–114, Feb.1981.

[7] C. N. Capsalis, J. G. Fikioris, and N. K. Uzunoglu, "Scattering from an abruptly terminated dielectric–slab waveguide," *J. Lightwave Technol.*, vol. LT–3, pp. 408–415, Apr. 1985.

[8] Hoi–Shun LUI, Han Tat HUI, and Mook Seng Leong, "A Note on the Mutual–Coupling Problems in Transmitting and Receiving Antenna Arrays " *IEEE Antennas and Propagation Magazine*, Vol. 51,

No.5, October 2009.

[9] Ramesh K Choudhary, *Advanced Computing and Communication Technologies*, Springer Science+Business Media, Singapore, 2016.

[10] Zhengyi Li, Zhengwei Du, Masaharu Takahashi, M. Kazuyuki Saito, and K. Ito, "Reducing Mutual Coupling of MIMO Antennas With Parasitic Elements for Mobile Terminals," *IEEE Trans. on Antennas and Propagat.*, vol. 60, pp. 473–481, Feb. 2012.

[11] S. Kim and S. Nam, "A compact and wideband linear array antenna with low mutual coupling," *IEEE Trans. Antennas Propag.*, vol. 67, no. 8, pp. 5695–5699, Aug. 2019.

Chapter 4. Conclusion

In this thesis, two types of printed dipole are introduced. The first of them describes the scan blindness effect and causes that may occur in T-printed dipoles. Second, the operation principle of bow-tie element printed on a substrate with high dielectric is explained. The contents of the study carried out are as follows.

First, in Chapter 1, First, the Evolution of the printed dipole antenna was introduced. In addition, various issues of scan blindness in the phased array antenna system are discussed. In section 1.3, it is explained why it would be reasonable to interpret the high dielectric antenna as PO.

Second, in Chapter 2, the mechanism of the scan blindness in a T-printed dipole array is analyzed, and an elimination strategy is proposed. The main cause of the scan blindness was found to be a quasi-TEM guided wave mode traveling along the printed dipole substrate in the E-plane through an infinite rectangular array. The existence of a guided wave was analyzed by confirming that the simulated eigen mode, dispersion relations derived from the equivalent circuit of unitcell and scan blindness curves are identical. It was also found that adding slits and stubs in the unit cell plays an important role in lowering the resonant frequencies in the printed dipole structure. Then, the difference between the scan blindness of

the 1D and 2D arrays was clarified using the comparison of the Q value in the unit cell in the 1D and 2D arrays. The proposed concept provides improvements in the gain and scan range.

Third, in Chapter 3, the principle of a printed bow-tie antenna on a high dielectric substrate is presented. The effectiveness of the PO approximation has been demonstrated in describing diffraction effects of the various wave species excited by an HED on a dielectric substrate. To implement the PO, the multilayered structure theory, complex solutions for dispersion equation and saddle-point method are introduced. According to the results, in the case of a high dielectric substrate with dielectric constant of 10 or more, the main component that constitutes the radiation pattern is TE_0 surface-wave (SW) diffracted ray generated from the edge of the dielectric slab. Based on the previously derived theory, a ku-band printed Bow-tie array antenna with low mutual coupling is proposed.

In conclusion, this thesis propose that the electromagnetic mechanism of the two printed type antenna. For the T-printed dipole, it is revealed that the cause of the scan blindness is TEM guided mode. And it is theoretically revealed that the main cause of the printed bow tie antenna with high permittivity is the diffracted ray of TE_0 Surface wave generated from the antenna.

Appendix

A.1. Derivation of Dispersion Relations

In this appendix, the derivation of dispersion relations and the method of the components extractions are introduced from the equivalent circuit of the T-printed dipole unit cell shown in Fig. 2.6. Each element in Fig. 2.6(b) is expressed in terms of the ABCD parameters as T.

$$T_{CapL} = \begin{bmatrix} 1 & \frac{1}{j2\omega C_{gp}} \\ 0 & 1 \end{bmatrix} \begin{bmatrix} 1 & 0 \\ \frac{1}{j2\omega C_{gp}} & 1 \end{bmatrix} \quad (\text{A.1.1})$$

$$\beta_{unit} = k_0 \sin \theta_{scan} \quad (\text{A.1.2})$$

$$T_{CapR} = \begin{bmatrix} 1 & 0 \\ \frac{1}{j2\omega C_{gp}} & 1 \end{bmatrix} \begin{bmatrix} 1 & \frac{1}{j2\omega C_{gp}} \\ 0 & 1 \end{bmatrix} \quad (\text{A.1.3})$$

$$T_{TL} = \begin{bmatrix} \cos \psi & jZ_{TL} \sin \psi \\ jZ_{TL} \sin \psi & \cos \psi \end{bmatrix} \quad (\text{A.1.4})$$

In this case, the phase of the transmission line (ψ) is given by

$$\psi = \beta_{TL} d_{TL} = \frac{2\pi\sqrt{\epsilon_{eff}}}{\lambda_0} d_{TL} \quad (\text{A.1.5})$$

where the length of the dipole arm d_{TL} is 1.3925 mm.

$$T_{TL} = \begin{bmatrix} 1 & 0 \\ 1 & 1 \\ j\omega C_{tp} & 1 \end{bmatrix} \begin{bmatrix} A_{TF} & B_{TF} \\ C_{TF} & D_{TF} \end{bmatrix} \begin{bmatrix} 1 & 0 \\ 1 & 1 \\ j\omega C_{tp} & 1 \end{bmatrix} \quad (\text{A.1.6})$$

$$T_{TL} = \begin{bmatrix} A_{TF} & B_{TF} \\ C_{TF} & D_{TF} \end{bmatrix} = \begin{bmatrix} \frac{-Y_{22,TF}}{Y_{21,TF}} & \frac{-1}{Y_{21,TF}} \\ \frac{Y_{11,TF}Y_{22,TF} - Y_{11,TF}Y_{22,TF}}{Y_{21,TF}} & \frac{-Y_{11,TF}}{Y_{21,TF}} \end{bmatrix} \quad (\text{A.1.7})$$

$$Y_{11,TL} = j\omega C_{ts} + \frac{L}{j\omega(L - L_m)(1 + 2L_m)} \quad (\text{A.1.8})$$

$$Y_{21,TL} = -j\omega C_{ts} + \frac{L}{j\omega(L - L_m)(1 + 2L_m)} \quad (\text{A.1.9})$$

$$Y_{12,TL} = -j\omega C_{ts} + \frac{L}{j\omega(L - L_m)(1 + 2L_m)} \quad (\text{A.1.10})$$

$$Y_{22,TL} = j\omega C_{ts} + \frac{L}{j\omega(L - L_m)(1 + 2L_m)} \quad (\text{A.1.11})$$

The unit cell matrix T_{unit} is expressed as follows:

$$T_{unit} = T_{CapL}T_{TL}T_{TF}T_{TL}T_{CapR} \quad (\text{A.1.12})$$

According to the dispersion relation theory, (A.1.12) can be derived as

$$\cos \beta_{unit} a = 2B_{unit}C_{unit} + 1 \quad (\text{A.1.13})$$

Using (2.2) and (A.1.13), the dispersion relation is expressed as

$$\cos k_0 a \sin \theta_{scan} = 2B_{unit}C_{unit} + 1 \quad (\text{A.1.14})$$

In principle, any EM simulator can simulate the two port network parameters of a unit cell. Each values of components in unit cell are determined by field distribution, geometry and the boundary conditions. Since the boundary in the y -direction of the unit cell does not have phase differences, it acts as act as H-wall.

A.1.1 Transmission Line

The arm of the T-printed dipole operates as a transmission line as shown in Fig. A.1.1(a). The values of Impedance (Z_{TL}) and the effective dielectric constant (ϵ_{eff}) obtained by exciting the waveguide port at both ends are shown in Fig. A.1.1(b).

A.1.2 Capacitance

The lumped capacitance can be extracted from the Y matrix for a Pi-type network. The waveguide ports at both ends are de-embedded by the length of the transmission line as shown in Fig. A.1.2(a). Using (A.1.15) ~ (A.1.17), we obtain the gap capacitances as shown in Fig. 21(b).

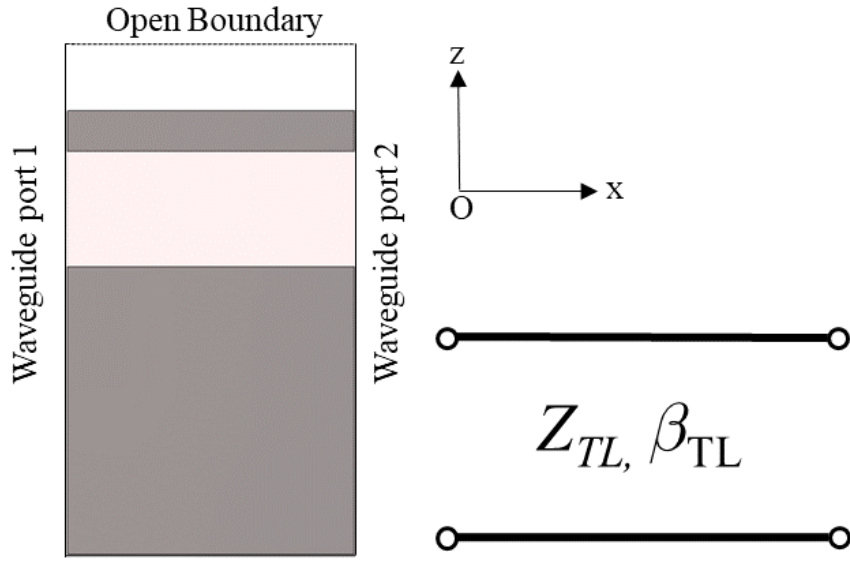
$$Y_{Cap} = \begin{bmatrix} Y_{11,cap} & Y_{11,cap} \\ Y_{11,cap} & Y_{11,cap} \end{bmatrix} \quad (\text{A.1.15})$$

$$C_{gs} = -\frac{\text{Im}(Y_{21,cap})}{\omega_0} \quad (\text{A.1.16})$$

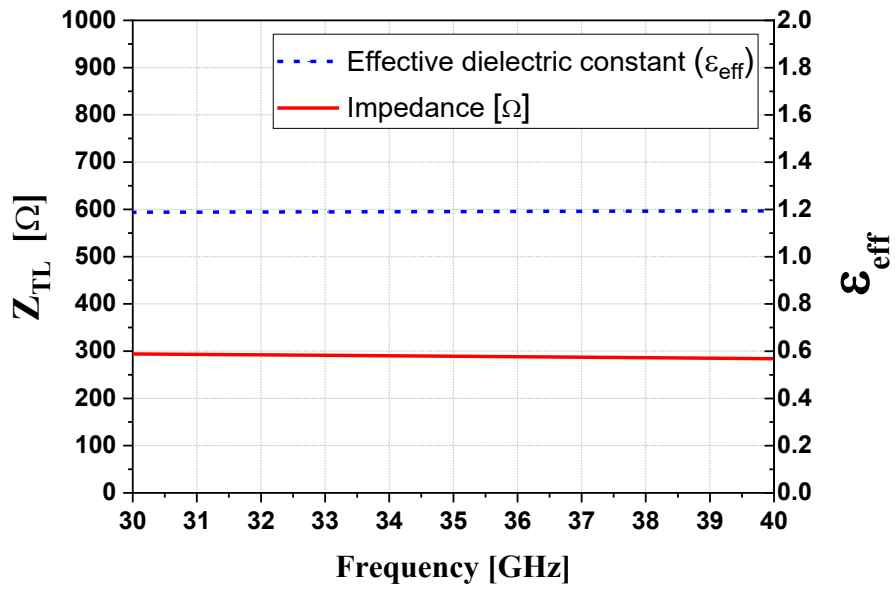
$$C_{gs} = -\frac{\text{Im}(Y_{11,cap} + Y_{21,cap})}{\omega_0} \quad (\text{A.1.17})$$

A.1.3 Transformer

Like capacitance, each component of the transformer can be calculated from the Z matrix extracted from the simulation. The self-inductance (L) and the mutual inductance (L_m) can be derived from (9), but the appropriate parasitic shunt capacitance (C_{tp}) and parasitic series capacitance (C_{ts}) values need to be determined. The parameter study determines the appropriate the C_{tp} so that the L has an independent value for the frequency. In the same way, C_{tp} associated with the L_m can be determined. Fig. A.1.3(a) shows the transformer geometry de-embedded by the length of the transmission line, and the mutual inductance and the self-inductance can be calculated as A.1.3(b). The values of the components are calculated as follows: $Z_{TL} = 288 \Omega$, $\epsilon_{\text{eff}} = 1.19$, $C_{gs} = 0.026 \text{ pF}$, $C_{gp} = 0.004 \text{ pF}$, $C_{tp} = 0.01 \text{ pF}$, $C_{ts} = 0.02 \text{ pF}$, $L = 0.46 \text{ nH}$, and $L_m = 0.24 \text{ nH}$.

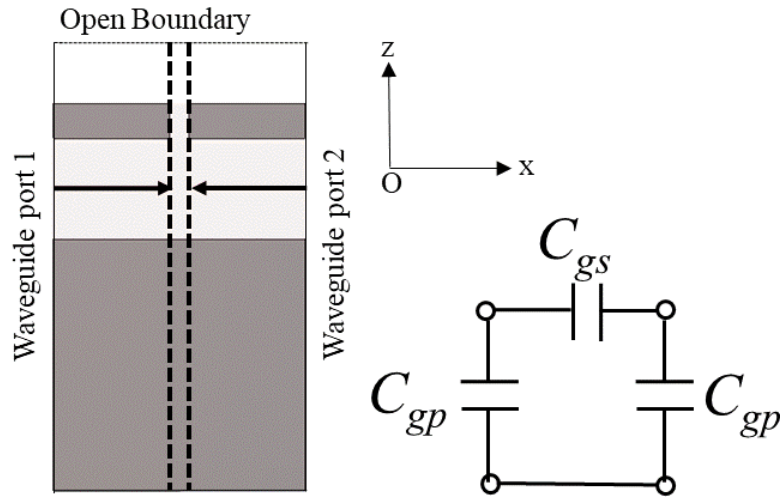


(a)

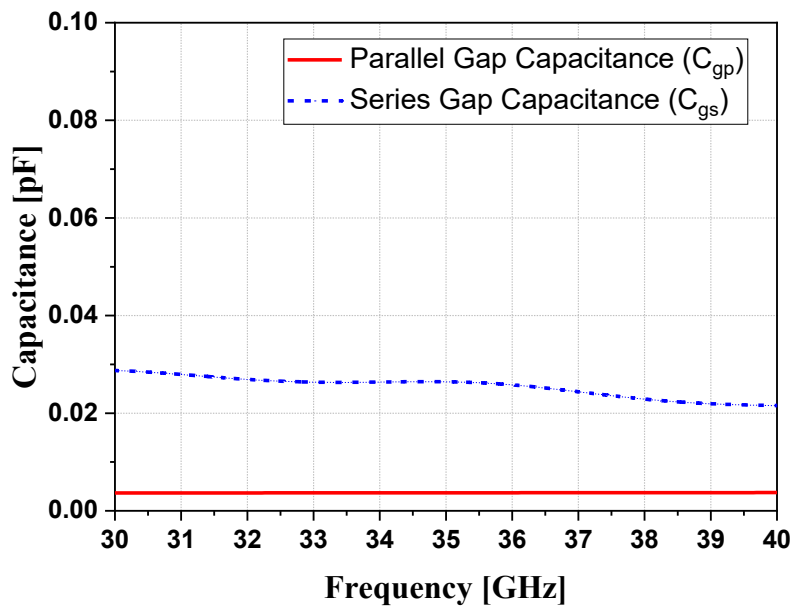


(b)

Fig. A.1.1 Extraction of TL parameters. (a) Simulation setup for TL parameters. (b) Characteristic Impedance Z_{TL} and phase constant β_{TL} .

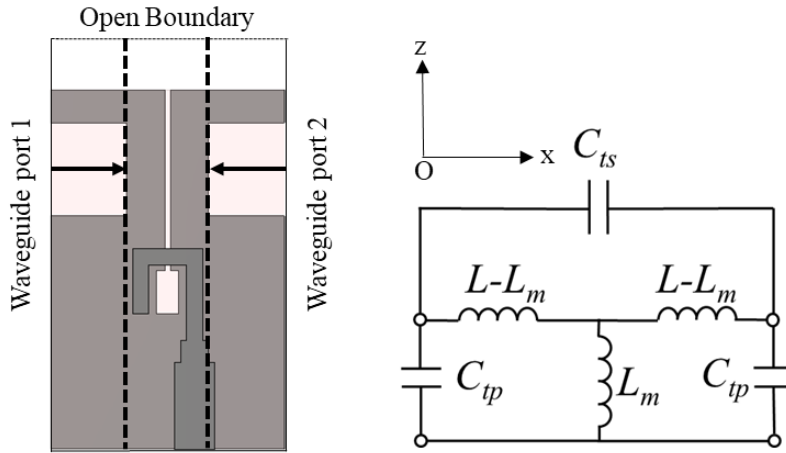


(a)

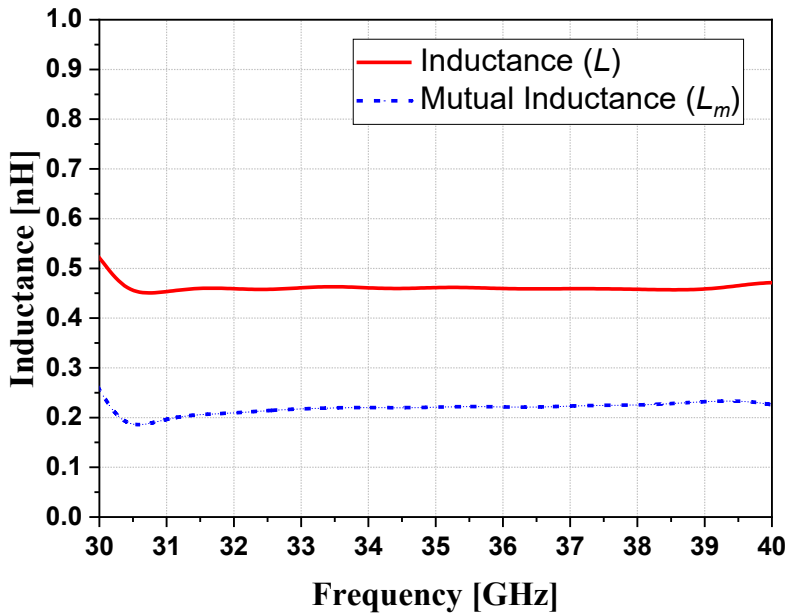


(b)

Fig. A.1.2 Extraction of gap capacitance parameters. (a) Simulation setup for gap capacitance parameters. (b) Gap capacitance for series (C_{gs}) and gap capacitance for parallel (C_{gp}).



(a)



(b)

Fig. A.1.3 Extraction of transformer parameters. (a) Simulation setup for transformer parameters. (b) Self-inductance (L) and mutual inductance (L_m).

A.2. Detailed Derivation of (3.43)

$$\widetilde{\mathbf{J}}^{\mathbf{PO}}(k_x, k_y, z) = (\widetilde{J}_{x_{TM}}^{\mathbf{a}} + \widetilde{J}_{x_{TE}}^{\mathbf{a}}) \hat{x} + (\widetilde{J}_{y_{TM}}^{\mathbf{a}} + \widetilde{J}_{y_{TE}}^{\mathbf{a}}) \hat{y} + (\widetilde{J}_{z_{TM}}^{\mathbf{a}}) \hat{z} \quad (\text{A.2.1})$$

Explicit expressions of the $\widetilde{J}_{x_{TM}}^{\mathbf{a}}$, $\widetilde{J}_{y_{TM}}^{\mathbf{a}}$, $\widetilde{J}_{z_{TM}}^{\mathbf{a}}$, $\widetilde{J}_{x_{TE}}^{\mathbf{a}}$ and $\widetilde{J}_{y_{TE}}^{\mathbf{a}}$ are given in Appendix A.

$$\widetilde{J}_{\phi_{TM}}^{\mathbf{PO}} = \widetilde{\mathbf{J}}_{\phi_{TM}}^{\mathbf{PO}} \cdot \hat{\phi} = -\sin \phi \cdot \widetilde{J}_{x_{TM}}^{\mathbf{a}} + \cos \phi \cdot \widetilde{J}_{y_{TM}}^{\mathbf{a}} \quad (\text{A.2.2})$$

$$\widetilde{J}_{\theta_{TM}}^{\mathbf{PO}} = \widetilde{\mathbf{J}}_{\theta_{TM}}^{\mathbf{PO}} \cdot \hat{\theta} = -\cos \theta \cos \phi \cdot \widetilde{J}_{x_{TM}}^{\mathbf{a}} + \cos \theta \cos \phi \cdot \widetilde{J}_{y_{TM}}^{\mathbf{a}} - \sin \theta \cdot \widetilde{J}_{z_{TM}}^{\mathbf{a}} \quad (\text{A.2.3})$$

$$\widetilde{J}_{\phi_{TE}}^{\mathbf{PO}} = \widetilde{\mathbf{J}}_{\phi_{TE}}^{\mathbf{PO}} \cdot \hat{\phi} = -\sin \phi \cdot \widetilde{J}_{x_{TE}}^{\mathbf{a}} + \cos \phi \cdot \widetilde{J}_{y_{TE}}^{\mathbf{a}} \quad (\text{A.2.4})$$

$$\widetilde{J}_{\theta_{TE}}^{\mathbf{PO}} = \widetilde{\mathbf{J}}_{\theta_{TE}}^{\mathbf{PO}} \cdot \hat{\theta} = -\cos \theta \cos \phi \cdot \widetilde{J}_{x_{TE}}^{\mathbf{a}} + \cos \theta \cos \phi \cdot \widetilde{J}_{y_{TE}}^{\mathbf{a}} \quad (\text{A.2.5})$$

The integral in (9) leads to

$$k_z = \sqrt{1 - k_\rho^2} \quad (\text{A.2.6})$$

$$B_{\xi}(u, k_y) = \frac{b_{\xi}^{TE}(u, k_y)}{TE} + \frac{b_{\xi}^{TM}(u, k_y)}{TM} \quad (\text{A.2.7})$$

$$b_{\phi}^{TE}(u, k_y) = j \frac{\epsilon_r - 1}{2} \cdot \sin \psi \cos(\phi - \psi) \cdot N_{TE} \quad (\text{A.2.8})$$

$$b_{\phi}^{TM}(u, k_y) = j \frac{\epsilon_r - 1}{2} \cdot k_z \cdot k_{z1} \cdot \cos \psi \cdot \sin(\phi - \psi) \cdot N_{TM} \quad (\text{A.2.9})$$

$$b_{\theta}^{TM}(u, k_y) = j \frac{\epsilon_r - 1}{2} \cdot k_z \cdot \cos \psi \cdot [\sin \theta k_{\rho} \cdot N_{TM} - \cos \theta \cdot \cos(\phi - \psi) \cdot P_{TM}] \quad (\text{A.2.10})$$

$$b_{\theta}^{TE}(u, k_y) = j \frac{\epsilon_r - 1}{2} \cdot \cos \theta \cdot \sin \psi \cdot \sin(\phi - \psi) \cdot N_{TE} \quad (\text{A.2.11})$$

$$\sin \psi = \frac{k_y}{k_{\rho}} \quad (\text{A.2.12})$$

$$\cos \psi = \frac{k_x}{k_{\rho}} = \frac{u}{k_{\rho}} \quad (\text{A.2.13})$$

$$a = e^{-jk_0 \cos \theta d} \quad (\text{A.2.14})$$

$$N_{TE} = \frac{1}{k_{z1}^2 - \cos^2 \theta} [ja \cdot k_{z1} \cdot [k_z - \cos \theta] + \sin(k_{z1} k_0 d) \cdot (k_{z1}^2 - k_z \cos \theta) - j \cos(k_{z1} k_0 d) \cdot k_{z1} \cdot (k_z - \cos \theta)] \quad (\text{A.2.15})$$

$$N_{TM} = \frac{1}{k_{z1}^2 - k_0^2 \cos^2 \theta} \cdot j[a - \cos(k_{z1} d)] \cdot [k_{z1}^2 - \epsilon_r k_z k_0 \cos \theta] - \sin(k_{z1} d) \cdot k_{z1} \cdot [\epsilon_r k_z - k_0 \cos \theta] \quad (\text{A.2.16})$$

$$P_{TM} = \frac{1}{k_{z1}^2 - k_0^2 \cos^2 \theta} \cdot j[a - \cos(k_{z1} d)] \cdot k_{z1} \cdot [\epsilon_r k_z - k_0 \cos \theta] - \sin(k_{z1} d) \cdot [k_{z1}^2 - \epsilon_r k_z k_0 \cos \theta] \quad (\text{A.2.17})$$

초 록

본 논문에는 밀리미터파 대역에서 주로 사용되는 프린티드 다이폴 안테나에서 성능에 중요한 영향을 미치는 전자기적 현상에 대해 집중적으로 연구를 진행하였다.

크게 두 가지 형태의 프린티드 다이폴에 대해 다루었는데, 그 중 첫번째는 T-형태를 가지는 프린티드 다이폴에서 발생할 수 있는 스캔블라인드니스 현상과 원인에 대해 기술하였다. 두 번째는 고유전율을 가지는 기판에 프린티드 된 Bow-tie 안테나를 Physical Optics(PO)와 회절과 이론을 바탕으로 동작 원리를 설명하였다.

첫 번째 타입으로, Ka-대역 프린티드 다이폴이 일차원과 이차원으로 배열되어 있을 때, 스캔 블라인드니스(scan blindness)를 분석하고 제거할 수 있는 방안을 제안하였다. 먼저 일차원과 이차원 사각배열에서 능동소자패턴의 E-면 방향으로 스캔 블라인드니스가 발생함을 확인하였다. 그리고 분산 관계와 스캔 블라인드니스와의 관계를 통해 quasi-TEM 공진 모드의 존재를 확인하였다. 공진모드에서 전기장의 분포를 분석하여 T-형태를 가지는 프린티드 다이폴의 단위 셀에 대한 등가회로를 구현하였고, 이로부터 분산 관계식을 도출하였다. 또한 일차원 배열과 이차원 배열일 때 Q 값 및 프린티드 다이폴의 스캔블라인드니스를 고찰하였고, 일차원 배열인 경우 방사 손실로 인해 상호 결합의 양이 이차원 배열보다 감소함을 확인하였다. 그리고나서, 스캔블라인드니스를 없애고 안테나의 빔 조향 범위를 향상시키기 위해, 슬릿과 스테프를 추가하였다. 이러한 기생 소자들의 효과를 확인하기 위해, 선형 배열 시뮬레이션을 수행하였고 quasi-TEM 모드가 억제되는 것을 확인 하였다. 마지막으로 일차원 배열에 대해서 11×1 부배열을 제작, 자기 벽 효과를 주기 위해 이차원 배열에 대해서는 11×3 부배열을 제작하였다. 측정을 통해 스캔 블라인드 예측을

검증하고 제안된 스캔 블라인드 메커니즘과 그 개선 사항을 확인하였다.

두 번째 타입으로, 고 유전율을 가지는 기판에 프린티드 된 Bow-tie 안테나의 동작 원리를 고찰하였다. 구조를 단순화 하기 위해 잘려진 유전체 기판위에 미소 다이폴 전류를 가정하였고, Physical Optics 이론을 적용하였다. 본 연구를 통해 안테나 방사패턴의 성분은 미소 다이폴에서 직접 방사하는 직접파와 유전체에 의한 반사파가 합쳐진 Geometric Optics(GO), 그리고 공간파(Space wave), 표면파(Surface wave), 누설파(Leaky wave)에 의해 발생하는 회절파(Diffracted Ray)로 구성되어 있음을 이론적으로 밝혔다. 이론의 타당성을 검증하기 위해 전자파 해석 프로그램인 CST MWS 및 FEKO를 사용하여 이론적으로 구한 closed form과 비교 검증하였다. 연구 결과에 따르면 유전율 10 이상을 가지는 고 유전체 기판의 경우 방사패턴을 구성하는 성분 중 대부분을 차지하는 주요성분은 기판의 모서리에서 발생된 TE0 모드 표면파에 의해 생성된 회절파 때문이다. 또한 이론적으로 안테나의 지향성이 6.5 dBi 이상 고이득을 얻을 수 있어 단일 안테나 설계에 유리하다.

앞서 도출한 이론을 바탕으로 낮은 상호결합을 갖는 ku-대역 프린티드 Bow-tie 배열 안테나를 제안 하였다. 잘려진 유전체의 모서리에서 유기된 회절파는 높은 이득을 생성할 뿐만 아니라, 직접파, 반사파의 상쇄효과로 인해 상호결합을 감소시킬 수 있다. 또한 단일 소자의 측면 하단에 Ohmic sheet를 추가하여 측면으로 진행되는 표면파를 감쇠 시켜 상호결합현상을 최소화 하였다. 특히 별도의 장치를 추가하지 않아도 높은 이득과 낮은 상호 결합을 얻을 수 있는 장점이 있다. 단일 안테나를 H-면 방향으로 일차원 부배열로 설계 및 제작하여 하여, 방사패턴의 이득은 6.5 dBi 이상 고 이득을 얻었고, 상호결합현상은 12.8 GHz 이후의 대역에서 -20 dB 미만을 얻어 설계의 타당성을 검증하였다.

결론적으로, 본 논문에서는 두 가지 형태의 프린티드 다이폴의 주요 전자기적 현상을 검증하였다. T-프린티드 다이폴에 대해

스캔블라인드니스의 원인이 TEM guided mode임을 밝혔고, 고 유전율을 가지는 프린티드 bow tie 안테나의 주요 원인은 antenna에서 generated된 TEO SW의 diffracted ray 임을 이론적으로 밝혔다.

주요어: 프린티드 다이폴 안테나, 스캔블라인드니스, 고 유전율을 갖는 Bow-tie 안테나, Physical Optics, 잘려진 유전체 기관에서의 회절파, 상호결합현상

학 번: 2015-31012